A study of the ground-state properties of charmonium via radiative transitions in ψ' → γηc and J/ψ → γηc

Haddadi, Zahra

university of groningen

A study of the ground-state properties of charmonium via radiative transitions in $\psi' \to \gamma\eta_c$ and $J/\psi \to \gamma\eta_c$

PhD thesis

to obtain the degree of PhD at the
University of Groningen
on the authority of the
Rector Magnificus Prof. E. Sterken
and in accordance with
the decision by the College of Deans.

This thesis will be defended in public on

Friday 8 December 2017 at 11.00 hours

by

Zahra Haddadi

born on July 27, 1984
in Firoozabad, Iran

Supervisor
Prof. N. Kalantar-Nayestanaki

Co-supervisors
Dr. J. G. Messchendorp
Dr. M. Kavatsyuk

Assessment committee
Prof. O. Scholten
Prof. R. J. M. Snellings
Prof. J. Feldman

ISBN (printed version): 978-94-034-0357-1
ISBN (electronic version): 978-94-034-0356-4

Contents

Chapter 1

Introduction

Through a combination of theory and experiment, a mathematical model that incorporate all that was known about elementary particles has been worked out. This model is called the Standard Model (SM) and describes what matter is made of and how it is held together. Basically, the SM is a theory describing the electromagnetic, weak, and strong nuclear interactions, as well as classifying all the subatomic particles known. The current formalism was formulated in the mid-1970s upon experimental confirmation of the existence of quarks. Since then, discoveries of the top quark (1995), the τ neutrino (2000), and the Higgs boson (2012) have given further credence to the SM. Although the SM is believed to be theoretically self-consistent and has demonstrated huge and continued successes in providing experimental predictions, it does leave some phenomena unexplained. The oldest enigma in fundamental particle physics is: where do the observed masses of composite particles such as hadrons come from? The dynamical generation of mass is not well understood. To shed light on this mystery, a better understanding of the structure of subatomic matter is essential. In the first part of this chapter, an introduction to the SM is given, with an emphasis on the fundamental theory of strong interactions, Quantum Chrormodynamics (QCD). Then, the charmonium system will be introduced as a tool towards understanding the unknown features of QCD.

1.1 The Standard Model (SM)

The particles involved in the SM are characterized by their spin, mass, electric charge and parity determining their interactions. These elementary particles are grouped into two classes: bosons and fermions.

Bosons:

The bosons have a spin that is 0, 1 or 2. The SM interactions are associated with the exchange of four vector bosons. The photon mediates electromagnetic interactions, the gluon strong interactions and the Z and W bosons, weak interactions. The photon and the gluons are massless, while the Z and the W are massive, which is the reason why weak interactions are weak at low-energy (they are suppressed by powers of $E/M_{Z;W}$, where E is the energy of the process and $M_{Z;W}$ is the mass of the Z and W bosons). The existence of electromagnetic, strong and weak interactions and the dependence of each of these on single parameters, the coupling constants, α, α_s and α_W respectively, follow from imposing a gauge symmetry on the model:

$$G_{SM} = SU(3) \times SU(2) \times U(1). \tag{1.1}$$

The weak and electromagnetic interactions are described by the groups $SU(2) \times U(1)$ with the photon and W^+, W^-, Z, as generators. $SU(3)$ is the symmetry group of the strong interaction. The strong interaction is mediated by the exchange of massless particles called gluons that interact with quarks and other gluons by arranging a color-charge label. Color-charge is analogous to electromagnetic charge, but it comes in three types (red, green, blue) rather than one. Gluons therefore participate in the strong interaction in addition to mediating it, making QCD significantly harder to analyze than Quantum Electrodynamics (QED).

The Yukawa interactions are mediated by a single scalar (spin-0) particle, the Higgs boson[1]. The Higgs boson plays a unique role in the SM, by providing an explanation of why the other elementary particles, except the photon and gluon, are massive. Local symmetry requirement of the gauge theory forbids the mediators of the forces to be massive. But for the W and Z bosons, the Higgs mechanism gives rise to the mass term in the corresponding Lagrangian. In electroweak theory, the Higgs boson generates the masses of the leptons (electron, muon, tau and neutrino) and quarks in order to preserve the $SU(2)$ symmetry. The bosons described by the SM are presented in table 1.1.

Fermions:

The fermions in the SM have spin 1/2. The particles in the SM are all fermions and consist of quarks and leptons. The main difference between quarks and leptons is that quarks experience the strong force while leptons do not. This force acts such that quarks

[1]The Yukawa interaction can be used to describe the strong nuclear force between nucleons (which are fermions), mediated by pions (which are scalar mesons).

boson	force	spin	color-charge	electric charge (e)	mass [GeV]
g	strong	1	8	0	0
γ	electromagnetic	1	0	0	0
$W^{\pm}$	weak	1	0	± 1	80
Z^0	weak	1	0	0	91

Table 1.1: The SM bosons.

quark	electric charge (e)	mass [GeV]	lepton	electric charge (e)	mass [GeV]
u	$+2/3$	0.002	ν_e	0	$< 2.2 \times 10^{-9}$
d	-1/3	0.005	e	-1	0.0005
c	$+2/3$	1.3	ν_μ	0	$< 1.9 \times 10^{-4}$
s	-1/3	0.1	μ	-1	0.1056
t	$+2/3$	173	ν_τ	0	$< 1.8 \times 10^{-2}$
b	-1/3	4.2	τ	-1	1.7768

Table 1.2: The SM fermions.

cannot be found as free particles since quarks carry color-charges and therefore hadrons appear to be color neutral. The total color-charge of a system is obtained by combining the individual charges of the constituents according to group theoretical rules analogous to those for combining angular momenta in quantum mechanics. The quarks have three basic color-charge states. Three color-charge states form a basis in a 3-dimensional complex vector space. A general color-charge state of a quark is then a vector in this space. The color-charge state can be rotated by 3×3 unitary matrices. All such unitary transformations with unit determinant form a Lie group $SU(3)$. The quarks (q), like the electron, have anti-particles, called antiquarks, often denoted by $\overline{q}$. The antiquarks have the same spin and mass as the quarks, but with opposite electric charges and with an anti-color assignment. One can more generally view quark confinement as color confinement: strong interactions do not allow states other than a color singlet to appear in nature. Quarks are bound together to form particles called hadrons, in triplets to form baryons (qqq or $\bar{q}\bar{q}\bar{q}$) or quark-antiquark pairs ($q\bar{q}$) to form mesons.

There are two types of leptons: charged ones like the electrons and neutral ones like the neutrinos. Both quarks and leptons are found in three generations, namely three sets of particles that carry the same quantum numbers, and differ only in mass. In each generation there are four types of particles: an up-type quark, a down-type quark, a charged lepton, and a neutrino. The list of the SM fermions is given in table 1.2.

One of the fundamental parameters of QCD is the coupling g_s (or $\alpha_s = g_s^2/4\pi$). QCD

does not predict the actual value of α_s, however it definitely predicts the functional form of the energy dependence of α_s. The dependence of the coupling constant on the distance or momentum scale can be determined by a differential equation [2]:

$$Q\frac{d\alpha_s(Q)}{dQ} = \beta(\alpha_s), \tag{1.2}$$

where Q is a momentum scale, roughly corresponding to $1/r$, $\beta(\alpha_s) = \frac{\beta_0}{2\pi}\alpha_s^2$ where $\beta_0 = 11 - \frac{2}{3}n_f$, with n_f being the number of active quark flavors. The left term comes from the non-linear gluon contribution and the right term comes from the quark-antiquark pair effect. The left term of the equation is positive and the right term is negative, thus the gluon self-coupling has an anti-screening effect. From equation 1.2, the coupling constant of QCD can be shown to have the following scale dependence [2]:

$$\alpha_s(Q) = \frac{2\pi}{\beta_0 \ln(Q/\Lambda_{QCD})}, \tag{1.3}$$

where β_0 is a constant and the quantity Λ_{QCD} is called the QCD scale and its value is $\Lambda_{QCD} = 217^{+25}_{-23}$ MeV [3]. Two important features of QCD can be observed from this running coupling constant, namely asymptotic freedom and confinement. These important features of QCD are illustrated in Figure 1.1. One of the striking properties of QCD is asymptotic freedom which states that the interaction strength $\alpha_s(Q)$ between quarks becomes smaller as the distance between them gets shorter, i.e. $\alpha_s \to 0$ for momentum transfer $Q \to \infty$, thus allowing perturbation theory techniques to be used. This subfield of particle physics is called perturbative QCD. For this observation, Gross, Politzer and Wilczek won the Nobel prize in physics in 2004. As a consequence of the gluon self-coupling, QCD implies that the coupling strength $\alpha_s(Q)$, becomes large at large distances or equivalently at low momentum transfers. Therefore, QCD provides a qualitative description for the observation that quarks do not appear as free particles, but only exist as bound states of quarks, forming hadrons like protons, neutrons and pions. This phenomenon is called confinement and the physics attributed to this energy regime is the so-called non-perturbative QCD.

QCD predicts the existence of exotic states besides the conventional baryons (qqq, $\bar{q}\bar{q}\bar{q}$) and mesons ($q\bar{q}$). They could be bound gluons (glueball), $q\bar{q}$-pairs mixed with excited gluons (hybrid), multi-quark color singlet states such as: $q\bar{q}q\bar{q}$ (tetra-quark or molecular states), $qqqq\bar{q}$ (penta-quark), $q\bar{q}q\bar{q}q\bar{q}$ (six-quark or baryonium), etc. (see Figure 1.2). The newly found XYZ states in the charmonium spectrum are candidates for exotic states. Their nature remains, however, unresolved. Data harvest at BESIII, an e^+e^- collider, might shed light on this puzzle.

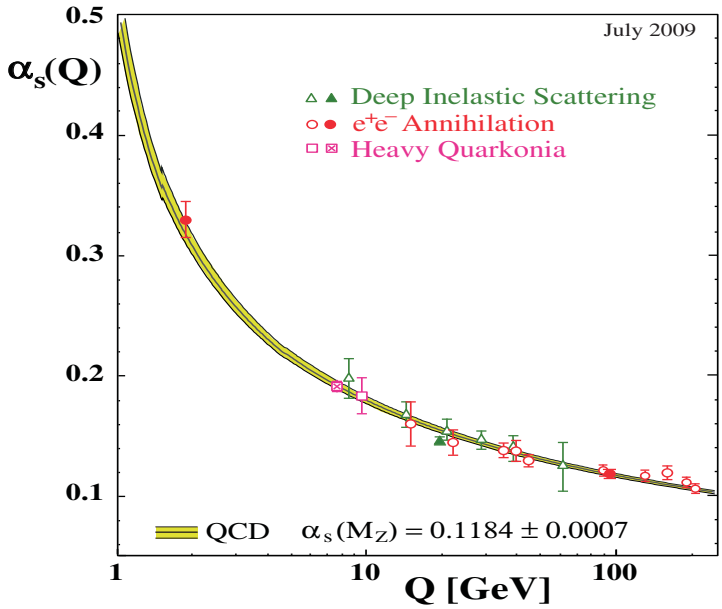

Figure 1.1: Summary of measurements of α_s as a function of energy scale Q [1]. Open symbols indicate NLO, and filled symbols NNLO QCD calculations as an input for the measurements. The curves are the QCD predictions from Lattice QCD for the combined world average value of $\alpha_s(M_Z)$ where M_Z is the mass of the Z boson.

e^+e^- collisions provide one of the cleanest environments in which to study applications of QCD in the regions between perturbative and non-perturbative QCD. The huge statistics accumulated by BESIII in the energy regime around the charmonium mass is ideally suited to study QCD in this transition regime. The advantage of e^+e^- collisions is that the initial state is well defined, in contrast to interactions involving hadrons. In addition, e^+e^- collisions involve an exchange of a virtual photon, γ^*, which is governed by QED which is well understood.

BESIII is designed to study the physics of charm, charmonium, light hadrons as well as τ physics. In this thesis, the focus is laid on charmonium physics.

1.2 Charmonium

The charmonium system was discovered in 1974, when two experimental groups at Brookhaven and SLAC announced almost simultaneously the observation of a new, narrow resonance, later to be called J/ψ [5]. This was the first observation of a charm

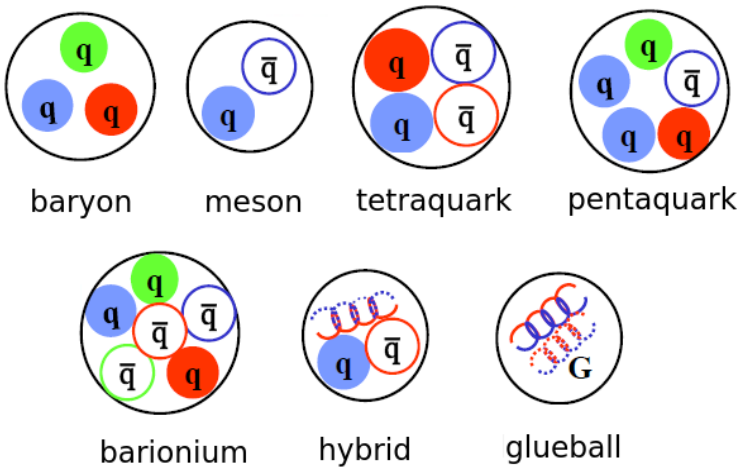

Figure 1.2: Possible bound states compatible with QCD.

and anti-charm quark pair. In the course of time, various other charmonium states were discovered which resulted in an energy spectrum as shown in Figure 1.3. Typically, the energy levels of the charmonium system were modeled by solving a non-relativistic Schrödinger equation, although there are more sophisticated calculations that take into account relativistic corrections and other effects [5]. The energy levels are characterized by the radial quantum number n_r, the relative orbital angular momentum between the quark and antiquark, L, and the spin, S. The current experimental and theoretical state-of-the-art is shown in Figure 1.3 [4]. For those levels that have been assigned, the commonly used name of its associated meson is indicated. The levels with different orbital angular momentum are labeled by S, P, D, F, corresponding to $L = 0$, 1, 2, 3. The quark and antiquark spins couple to give a total spin $S = 0$ (spin-singlet) or $S = 1$ (spin-triplet). S and L couple to give the total angular momentum of the state, J. The parity of a quark-antiquark state with orbital angular momentum L is $P = (-1)^{L+1}$ and the charge conjugation eigenvalue is given by $C = (-1)^{L+S}$. Thus L can mix between states with the same P and C parity, since the interaction potential between the quark and anti-quark is not necessarily spherical symmetric, for example due to a tensor interaction. It is common to specify the various quantum configurations of charmonium states using the spectroscopic notation $(n_r + 1)^{2S+1}L_J$, where n_r is the radial quantum excitation number with $n_r = 0$ corresponding to the lowest state in this spectrum.

The thresholds at which charmonium is allowed to decay into a pair of open-charm mesons are indicated by dashed lines in Figure 1.3. The lowest open-charm threshold

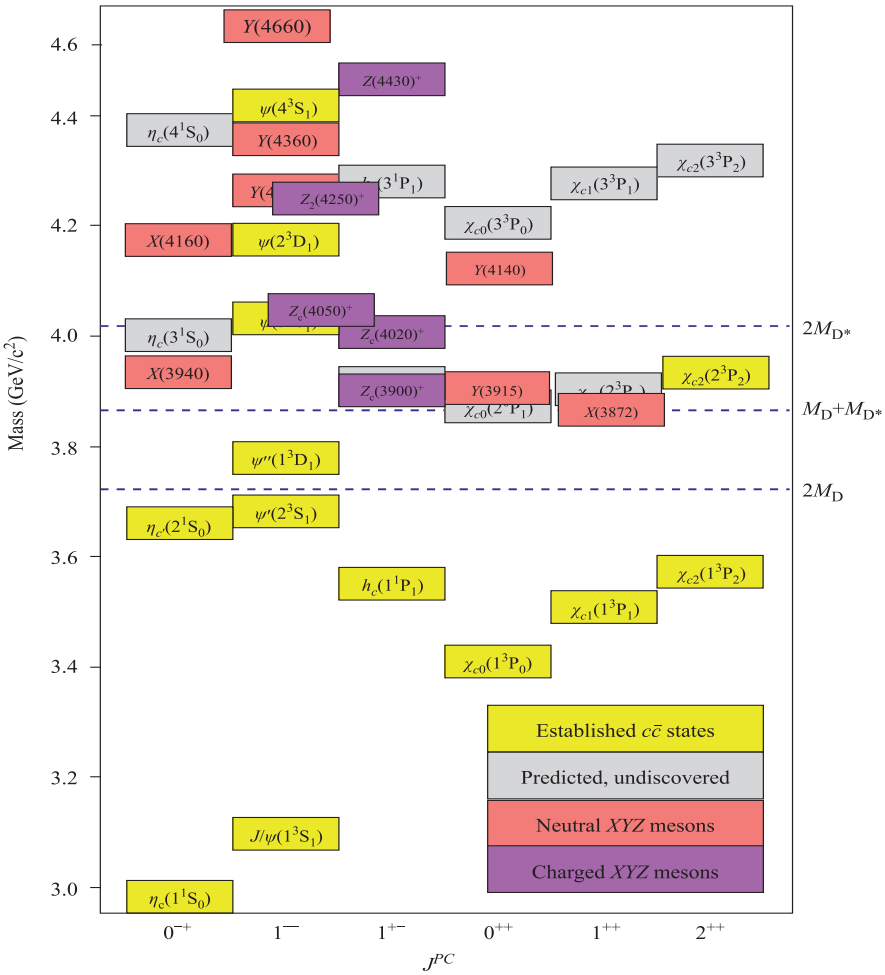

Figure 1.3: The spectrum of charmonium and charmonium-like states in the energy regime covered by BESIII [4].

corresponds to about 3.73 GeV, which is twice the mass of the D-meson, $(c\bar{u}, c\bar{d})$. The charmonium states below the open-charm threshold are in general narrow in width, corresponding to a long lifetime, much smaller than the mass differences among the states. Above the charm threshold, where the production of a pair of open-charm mesons becomes possible, charmonium states are much broader and they may overlap. Therefore, spectroscopy is more favorable below the open-charm threshold. In the following, we discuss in more detail the region above and below the $D\bar{D}$ threshold. The region below the open-charm threshold is our main focus for this thesis.

1.3 Charmonium above the open-charm threshold

In the energy region above the open-charm threshold, a number of new states have been observed. These states are not necessarily pure charmonium states, but all of them have charmonium among their decay products. They are called charmonium-like states, and they are classified in three categories, X, Y and Z. X states are neutral and produced in B decays and Y transitions. Y states are electrically neutral vector states 1^- which can be directly produced in e^+e^- colliders. $Z^\pm$ states are charged quarkonium-like particles. Figure 1.3 shows the charmonium and charmonium-like meson spectrum for masses below 4500 MeV. Here, the yellow boxes indicate established charmonium states. The gray boxes show the remaining unfilled, not discovered yet but predicted charmonium states. The red boxes show electrically neutral X and Y mesons and the purple boxes show the charged Z mesons. There are many missing charmonium states above the open-charm threshold. Charmonium-like XYZ mesons were first observed in 2003 and continue to be found at a rate of about one or two new ones every year. In March 2013, BESIII announced the discovery of a charged charmonium-like state through $e^+e^- \to \pi^\pm Z_c(3900) \to \pi^\pm\pi^\mp J/\psi$. The $Z_c(3900)$ is a good candidate for an exotic tetraquark. Many of the XYZ states have exotic properties, which may indicate that exotic states, such as multi-quark, molecule, hybrid, or hadron-quarkonium, have been observed. In order to get insight in the dynamics of these complex charmonium-like states in an energy regime with broad resonances, one necessarily has to understand states in a more clean region, namely below the open-charm threshold.

1.4 Charmonium below the open-charm threshold

The charmonium spectrum consists of eight narrow states below the open-charm threshold. The lowest state with $L = 0$, $S = 0$ and (necessarily) $J = 0$ is represented as 1^1S_0 (η_c resonance) while the first excited state with the same quantum numbers is 2^1S_0 ($\eta_c^{'}$ resonance). The orbital excited $L = 1$ states are the $^1P_1$, known as the h_c, and the $^3P_{0,1,2}$ corresponding to the triplet P-waves, $^3P_{0,1,2}$, referred to as χ_{c0}, χ_{c1} and χ_{c2}. The $^3(S,D)_1$ states correspond to resonances which are populated directly in e^+e^- annihilation since they have the same quantum numbers as the photon, $J^{PC} = 1^{--}$. In the J^{PC} notation, the quantum number of the states below the open-charm threshold are 0^{-+} ($\eta_c, \eta_c^{'}$), 1^{--} ($J/\psi, \psi^{'}$), 1^{+-} (h_c), 0^{++} (χ_{c0}), 1^{++} (χ_{c1}) and 2^{++} (χ_{c2}). Almost all states below the open-charm threshold are well established except the spin-singlet states, η_c and $\eta_c^{'}$, mainly because they are populated indirectly in e^+e^- collision via suppressed transitions. Except for J/ψ and $\psi^{'}$, the other states below the open-charm

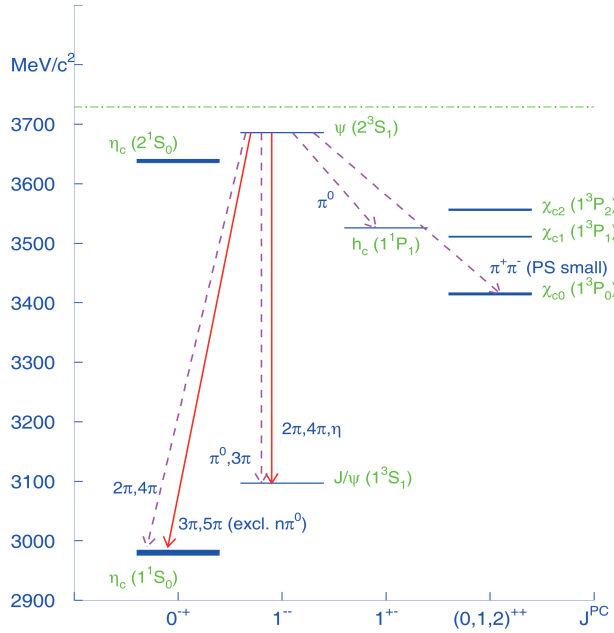

Figure 1.4: Hadronic transitions below the open-charm threshold. The allowed (suppressed) hadronic transitions are shown with solid (dashed) lines [58].

threshold are populated via radiative and hadronic transitions in e^+e^- collisions. In the following, the radiative and hadronic transitions below the open-charm threshold are discussed.

- Hadronic transitions:

There are hadronic transitions between two states if the mass difference is large enough to produce π, η or even heavier mesons. The allowed transitions are constrained by C and P parity, quantum numbers which are presented in hadronic decays due to strong interactions. The hadronic transitions of the ψ' are shown in Figure 1.4. Other hadronic transitions not shown in this figure were only studied scarcely. For more detailed information related to possible hadronic transitions, we refer to [58].

- Radiative transitions:

Radiative transitions of higher-mass charmonium states, such as the ψ', are of interest

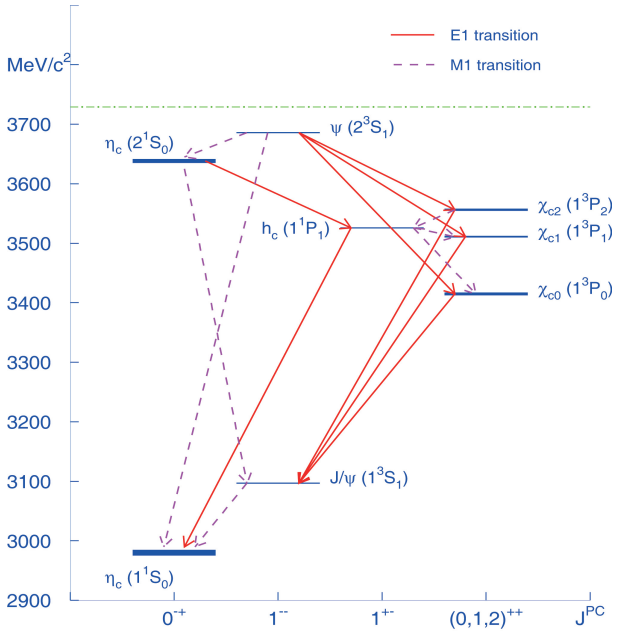

Figure 1.5: Radiative transitions of charmonium below the open-charm threshold [58].

largely because they provide access to $c\overline{c}$ states with different quantum numbers. Since the J^{PC} of the photon is 1^{--}, single photon transitions can only occur between two states of different C-parity. The transitions are either electric- or magnetic-multipole processes, depending on the spins and parities of the initial and final-states. If the product of the parities of the initial state (π_i) and final-state (π_f) is equal to $(-1)^{J_\gamma}$, the transition is an E_{J_γ} transition; otherwise, if $\pi_i \cdot \pi_f = (-1)^{J_\gamma+1}$, it is an M_{J_γ} transition, where J_γ is the total angular momentum carried by the photon. In general, when more than one multipole transition is allowed, only the lowest one is important, thus the E1 and M1 transitions are the dominant ones. The E1 transitions preserve the initial quark spin directions and they have large branching fractions up to the order of 10^{-1}. Although M1 rates are typically lower than E1 rates, since M1 transitions are accompanied by a spin flip of one of the quarks, they are nonetheless interesting because they may allow access to spin singlet states that are very difficult to produce otherwise. It is also interesting that the known M1 rates show serious disagreement between theory and experiment. Figure 1.5 shows all the possible E1 and M1 transitions below the open-charm threshold.

1.5 The line shape of η_c

The η_c was observed for the first time by the Crystal-Ball experiment in 1984 via the M1 radiative transition of $\psi^{'} \to \gamma\eta_c$. After this discovery, the next generation of experiments started to measure the basic properties of the η_c. There is a large systematic variation on the mass and width of the η_c between various experiments, much larger than observed for other charmonium states. One has realized that these variations might be due to a lack of understanding of the line shape of the η_c. To extract the mass and width, assumptions have to be made on its line shape. It is possible to get access to the η_c line shape via radiative and hadronic transitions. Radiative transitions have the advantage that the process is governed by the well-understood QED dynamics, while hadronic transitions suffer from uncertainties related to strong QCD.

Most recently, the BESIII collaboration studied the line shape of the η_c via six exclusive decay modes. Figure 1.6 shows some of the results. A significant asymmetric line shape was observed within the η_c mass range. By considering an interference effect between the η_c signal and a non-resonant background, one was able to describe the observed asymmetry [26]. The statistical significance for the interference effect is estimated to be around 15σ which is considerable.

The discrepancy between various measurements of the basic properties of η_c, the distortion of the η_c line shape and the role of interference between signal and non-resonant background on the line shape motivated us to study the η_c line shape more precisely via radiative transitions. This thesis is devoted to an analysis of two M1 radiative transitions, namely $\psi^{'} \to \gamma\eta_c$ and $J/\psi \to \gamma\eta_c$, with the aim to shed some light on the line shape behavior near the η_c mass.

1.6 Outline of the thesis

The outline of this thesis is as follows:

Chapter 2: In this chapter the various theoretical predictions and experimental measurements related to charmonium spectrum will be discussed. The motivation for studying the M1 transitions $J/\psi \to \gamma\eta_c$ and $\psi^{'} \to \gamma\eta_c$ and thereby studying the properties of the ground state of charmonium, η_c, is discussed.

Chapter 3: This chapter gives an overview of the BESIII detector. First, the subdetectors of BESIII are explained, then the BESIII offline software, BOSS, which was

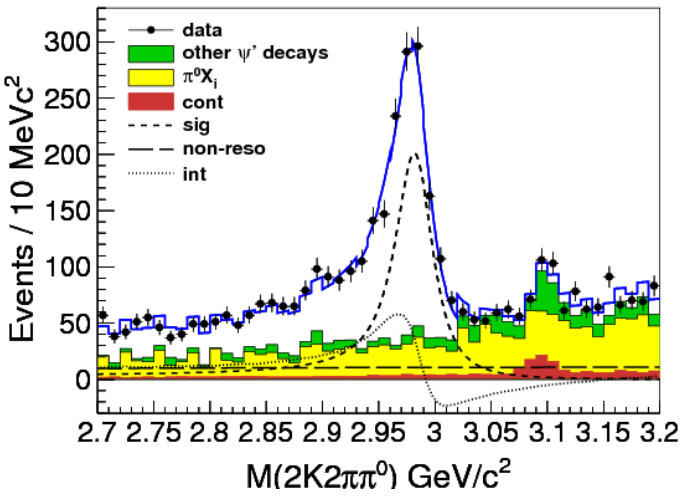

Figure 1.6: The invariant-mass distribution for $2K2\pi\pi^0$ decay. Points are data and the blue curve is the total fit result of 5 exclusive decay modes. Signals are shown as short-dashed lines, the non-resonant components as long-dashed lines, and the interference between them as dotted lines. Shaded histograms are (in red/yellow/green) for (continuum/$\pi^0 X_i$/other $\psi^{'}$ decays) backgrounds [26].

the basis of our data analysis, is described.

Chapter 4: This chapter is dedicated to analysis tools and methods which are used to perform the two reported analyses in this thesis. The tools and methods include particle identification, kinematic fitting and vertex fitting.

Chapter 5: The $J/\psi \to \gamma\eta_c$ transition is described in this chapter. This analysis is done exclusively through the decay mode of $\psi^{'} \to \pi^{\pm}\pi^{\mp}J/\psi,\ J/\psi \to \gamma\eta_c,\ \eta_c \to K^{\circ}_S K^{\pm}\pi^{\mp}$, by analysing the 2009 and 2012 $\psi^{'}$ data sample of BESIII. The main objective is to study the line shape of the η_c more precisely in order to probe the origin of the unexpected behavior of this line shape. The decay rate of $J/\psi \to \gamma\eta_c$ and the basic properties of the η_c are measured.

Chapter 6: The $\psi^{'} \to \gamma\eta_c$ transition is described in this chapter. This analysis is done inclusively by studying the 2009 $\psi^{'}$ data sample of BESIII. The aim is to measure the decay rate of this transition. The basic properties of the η_c are obtained with and without considering the interference with a non-resonant background contribution.

Chapter 7: This chapter summarizes the main aspects that were discussed in this thesis. Conclusions are drawn from the results we obtained, with an outlook towards future activities.

Chapter 2

Experimental and theoretical approaches

Radiative transitions between the charmonium states have recently been the subject of many theoretical calculations and experimental activities. Key among these studies are the magnetic dipole (M1) transitions $J/\psi \to \gamma\eta_c$ and $\psi^{'} \to \gamma\eta_c$ which are among the most poorly measured transitions in the charmonium system. Not only are precision measurements needed to determine the partial widths of these transitions but also these transitions are a source of information on the η_c mass and width. In this chapter, we review the experimental methods and theoretical models used for the study of charmonium spectroscopy and in particular the M1 transitions. We focus on models which make predictions of many of the observed properties of charmonium resonances, such as radiative decay rates and the basic properties of the η_c.

2.1 Electron-positron annihilation

The earlier studies of charmonium were done exclusively at e^+e^- colliders. These include the SLAC experiments Mark I, II and III, TPC and Crystal-Ball (CBALL); the DASP and PLUTO experiments at DESY; CLEO and CLEOc at the Cornell Storage Ring; the LEP experiments; the BES experiment at the BEPC collider in Beijing; BaBar and BELLE at the SLAC and KEK-B B factories, respectively [6]. In these experiments, the e^+e^- annihilation proceeds primarily through an intermediate virtual photon, creating a bound $c\bar{c}$ state, as shown in Figure 2.1. Other production mechanisms include photon-photon fusion (Figure 2.2), initial-state radiation (Figure 2.3) and B-meson decay (Figure 2.4). The individual charmonium production mechanisms in e^+e^- collisions will be briefly discussed in the following sub-sections.

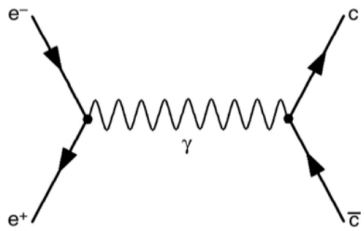

Figure 2.1: The Feynman diagram for the process $e^+e^- \to c\bar{c}$.

2.1.1 Direct formation

In e^+e^- annihilations, only states with the same quantum number as the photon, $J^{PC} = 1^{--}$, are directly formed such as J/ψ, $\psi^{'}$ and $\psi(3770)$. Figure 2.1 illustrates this formation mechanism. Precise measurements of the line shapes of these states can be obtained from the energies of the electron and positron beams, which are known with good accuracy. All the other charmonium states are populated indirectly via radiative or hadronic transitions of $J^{PC} = 1^{--}$ resonances. The basic properties such as mass, width, spin and parity of these resonances are determined from a measurement of the recoil (photon) energy and via the observation of their decay products. The precision in the measurement of the masses and widths of these states is limited by the detector resolution, which is worse than the precision with which the beam energies are known.

In this work, we make use of the radiative process, $J/\psi(\psi^{'}) \to \gamma\eta_c$, to study the properties of the η_c. Since the width of the η_c is larger than the detector resolution, it is still feasible to use such an indirect process to study its properties. Also, the huge statistics in $\psi^{'}$ decays provide an ideal data sample to perform such a study.

2.1.2 Two-photon production

Electron-positron scattering allows the production of $C = +1$ states of charmonium through the annihilation of two virtual photons via the process:

$$e^+e^- \to e^+e^- + c\bar{c}. \tag{2.1}$$

Figure 2.2 illustrates this two-photon process. The annihilation of two photons gives access to charmonium states with spin-parity other than $J^{PC} = 1^{--}$, which therefore complements the direct formation of charmonium via e^+e^- annihilation. As there are two photons involved, the production rate in this case decreases by a factor of α^2 from the rate for a single photon, where α is the fine structure constant. The cross section

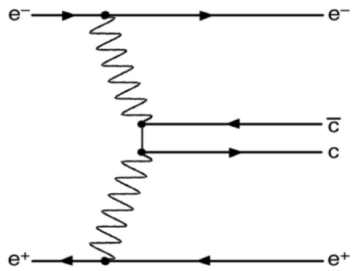

Figure 2.2: The Feynman diagram for the two-photon fusion process.

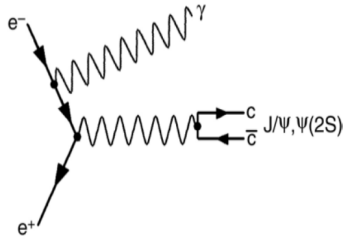

Figure 2.3: ISR production of charmonium.

for this process is proportional to the two-photon cross section, $\sigma(\gamma\gamma \to c\bar{c})$. The $c\bar{c}$ state, such as the η_c, is identified by observing its hadronic decays, thus the limitations of this method come mainly from the knowledge of the hadronic branching ratios and from the $\eta_c \to \gamma^*\gamma^*$ form-factors that are needed as input to extract the $\gamma\gamma$ width from the measured cross section. CLEO, BELLE, BaBar and KEDR are experiments that exploited the two-photon mechanism to study the basic properties of the η_c.

2.1.3 Initial-State Radiation (ISR)

Another mechanism for the production of charmonium states in e^+e^- collisions is the so-called Initial-State Radiation (ISR). In this process, illustrated in Figure 2.3, either the electron or the positron radiates a photon before the annihilation of the e^+e^- pair into a virtual photon, thereby lowering the effective center-of-mass energy. Like in the direct formation, only $J^{PC} = 1^{--}$ states can be produced directly in ISR.

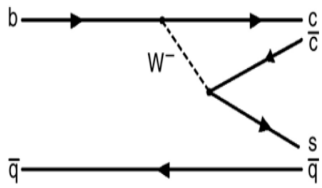

Figure 2.4: B-meson decay to charmonium.

2.1.4 B-meson decay

B mesons are mesons composed of a bottom antiquark and either an up (B^+), down (B^0), strange (B_s^0) or charm quark (B_c^+). B_c^+ is the heaviest B meson and the most difficult one to produce. Each B meson has an antiparticle that is composed of the bottom quark and up (B^-), down ($\bar{B}^0$), strange ($\bar{B}_s^0$) or charm ($\bar{B}_c^+$) antiquark. B mesons decay via weak interactions. The dominant decay mode of a b quark is $b \to cW^{*-}$, where the virtual W decays into a pair of leptons $l\bar{\nu}$ or in a semileptonic decay or into a pair of quarks as illustrated in Figure 2.4. A B factory is a particle collider dedicated to producing B mesons. Studies of b decays have been performed in e^+e^- collisions. ARGUS, CLEO, BELLE, BaBar experiments were designed to produce copious pairs of B mesons with the center-of-mass energy tuned to the $\Upsilon(4S)$ resonance peak with the quark content $b\bar{b}$, CLEO and BELLE at the $\Upsilon(5S)$ resonance peak, and SLAC and LEP at higher energies at the Z resonance. The decay of B mesons can be used to study charmonium as well. For example, the process $B^\pm \to K^\pm\eta_c$ has been used to study the charmonium ground state. The advantages of $B^\pm \to K^\pm c\bar{c}$ decays are the relatively large reconstruction efficiency, small background, and the fixed quantum numbers $J^P = 0^-$ of the initial state.

2.2 Hadron colliders

2.2.1 $p\overline{p}$ annihilation

In $p\overline{p}$ annihilation, the intrinsic limitation of e^+e^- experiments, where direct formation is possible only for $J^{PC} = 1^{--}$ states, can be overcome. In this case, the coherent annihilation of the three quarks in the proton with the three antiquarks in the antiproton via intermediate states with the appropriate number of gluons and/or virtual $q\overline{q}$ pairs, makes it possible to form directly states with all conventional quantum numbers. As an example, Figure 2.5 illustrates annihilations via two- and three-gluon intermediate

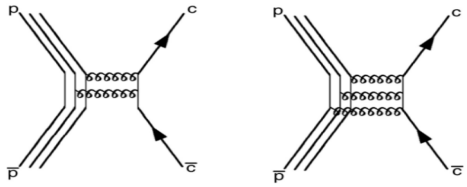

Figure 2.5: Charmonium formation in $p\bar{p}$ annihilations via an intermediate two-gluon (left) or three-gluon state (right).

states for C-even and C-odd charmonium states. This mechanism has been used at Fermilab and will be used in future experiments such as PANDA.

2.2.2 pp colliders

In an experimental setup that aims to study heavy quark systems by exploiting pp collisions, it is energetically favorable to let the protons circulate in opposite directions to populate high mass states such as B mesons that subsequently can decay to charmonium. LHCb is one of the experimental facilities that uses head-on pp collisions [7]. The LHCb experiment is situated at one of the four points around CERN's Large Hadron Collider (LHC) where beams of protons are smashed together, producing different particles. LHCb is a specialized b-physics experiment, in that it is measuring the parameters of CP violation in the interactions of b-hadrons. High center-of-mass energies available in proton-proton collisions at the LHCb ($\approx 7-8$ TeV) allow models describing charmonium production to be tested. LHCb experiments distinguish charmonia directly produced in parton interactions from those originating from b-hadron decays. Basic properties of the η_c are measured in LHCb via the decay mode of $\eta_c \to p\overline{p}$ [30].

2.3 Basic formalism of radiative transitions

In the following, we will concentrate on the theoretical formalisms that are used to describe the charmonium systems and the radiative transition processes between two charmonium states. This will be the basis of our research since we are primarily interested in the M1 transitions $\psi' \to \gamma\eta_c$ and $J/\psi \to \gamma\eta_c$ via the e^+e^- production of vector charmonium states. The M1 radiative partial widths between an initial charmonium state i of radial quantum number n_i, orbital angular momentum L_i, spin S_i, and total angular momentum J_i, and a final-state f with corresponding quantum numbers, is

given by [29]:

$$\Gamma_{M1}\left(n_i^{2S_i+1}L_i \to n_f^{2S_f+1}L_f\right) = \frac{4}{3}\left(\frac{2J_f+1}{2L_i+1}\right)e_c^2\,\frac{\alpha}{m_c^2}\delta_{L_iL_f}\delta_{S_i,S_f\pm1}\,|\langle\psi_f \mid \psi_i\rangle|^2\,E_\gamma^3\frac{E_f^{(c\bar{c})}}{M_i^{(c\bar{c})}}. \tag{2.2}$$

In the above formula, e_c is the charge of the c-quark in units of e, and $M_i^{(c\bar{c})}$ ($M_f^{(c\bar{c})}$), $E_f^{(c\bar{c})}$ represent masses of initial and final-states and the total energy of the final-state, respectively. The momentum of the transition photon equals $E_\gamma = (M_i^{(c\bar{c})2} - M_f^{(c\bar{c})2})/(2M_i^{(c\bar{c})})$.

Different theoretical methods are used to calculate the overlap between the initial and final wave functions, $|\langle\psi_f \mid \psi_i\rangle|^2$. In the following, the basic concept of some of the theoretical methods which are used to calculate the partial decay width of M1 transitions is explained.

2.4 Theoretical methods

Most theorists agree that the spectroscopy of heavy quarkonium should be described based on first principles, namely QCD. QCD alone should describe the spectroscopy of heavy quarkonium. Nevertheless, there are important difficulties to do so in practice. The theoretical approaches attempt to model what are believed to be the features of QCD relevant to heavy quarkonium with the aim to produce concrete results which can be directly confirmed or refuted by experiment and may guide experimental searches. The theoretical approaches try to describe heavy quarkonium via QCD-inspired calculations and/or approximations. In this section, we give an introduction to QCD, then the basic theoretical methods such as lattice QCD, potential model and effective field theory are discussed in connection to the topic of this thesis.

2.4.1 QCD

The Standard Model (SM) is first of all a quantum field theory (QFT). In QFT, particles are associated to fields $\phi_i(x)$, $i = 1, ..., n$, depending on the space-time coordinates, $x = (x^0, x^1, x^2, x^3)$. In the SM, only the fields with spin = 0, 1/2, 1 are considered (no gravity), since these are the only ones for which one knows how to write a theoretically consistent QFT. Their dynamics is determined by an action S written in terms of a

Lagrangian density $\mathcal{L}(x)$ with dimension 4 in energy:

$$S = \int d^4x \mathcal{L}. \tag{2.3}$$

QCD is formulated in terms of elementary fields (quarks and gluons), whose interactions obey the principles of a relativistic QFT, with a non-abelian gauge invariance $SU(3)$. If we introduce 8 gluon potentials, U_a^μ, as well as the associated covariant derivative, $D^\mu \equiv \partial^\mu + igU_a^\mu \lambda^a/2$, the quark Lagrangian can be written as:

$$\mathcal{L}_q = \overline{\psi}(iD^\mu - m_q)\psi, \tag{2.4}$$

where $\lambda^a/2$ ($a = 1, ..., 8$) are 3×3 hermitian matrices and are the so-called generators of $SU(3)$ rotations, ψ ($\overline{\psi}$) is the Dirac spinor of the quark field. $g = \sqrt{4\pi\alpha_s}$ represents the color charge (strong coupling constant). Quarks interact with gluons in a way similar to electrons interacting with photons. A new feature here is that the quark can change its color by emitting or absorbing a gluon of color a. Gluons are physical degrees of freedom and therefore must carry energy and momentum themselves. Thus one must add additional terms in the Lagrangian to describe these physical features. Following the successful theory of Maxwell on electromagnetism, the kinetic energy term for the gluons can be introduced by using the antisymmetric field strength tensor $F_{\mu\nu}^a$:

$$\mathcal{L}_g = -\frac{1}{4} F_a^{\mu\nu} F_{\mu\nu}^a. \tag{2.5}$$

The full QCD lagrangian density is the sum of the quark and gluon terms:

$$\mathcal{L}_{QCD} = \mathcal{L}_q + \mathcal{L}_g. \tag{2.6}$$

The dynamics of QCD is significantly different from that of QED. This is due to the fact that gluons carry color charges, which give rise to a self-interaction among gluons. In fact, these interactions are responsible for many of the unique and salient features of QCD. For example, QCD has two distinct features at low-energy, where the momentum transfer $p \ll \Lambda_{QCD} \approx 200$ MeV, namely confinement and the spontaneous breaking of the chiral symmetry. The former confines quarks and gluons in hadrons, and the latter is the origin of mass of the hadrons. Since analytic or perturbative solutions in low-energy QCD are hard or impossible to obtain due to the highly nonlinear nature of the strong force and the large coupling constant at low energies, alternative approaches are called for which are non-perturbative theoretical approaches.

2.4.2 Lattice QCD (LQCD)

LQCD was first proposed by K. Wilson in 1974 [11] and provides a method to calculate, based on first principles, the preparation of hadronic systems in the non-perturbative regime. In LQCD, the space-time is discretized, usually on a hypercubic lattice with lattice spacing a, with quark fields placed on sites and gauge fields on the links between the sites (sources). The continuum theory is obtained by taking the limit of vanishing lattice spacing, which can be reached by tuning the bare coupling constant to zero according to the renormalization group. In practice LQCD calculations are limited by the availability of computational resources and the efficiency of algorithms. Because of this, LQCD results come with both statistical and systematic errors, the former arising from the use of Monte Carlo integration, the latter, for example, from the use of non-zero values of a.

2.4.2.1 Method

It is straightforward to define the quantum theory using the path integral formalism, once the lattice action is known. The Euclidean-space partition function is given by [20]:

$$Z \;=\; \int \mathcal{D}A_\mu \; \mathcal{D}\psi \; \mathcal{D}\bar{\psi} \; e^{-S}, \tag{2.7}$$

where $\mathcal{D}\psi$ represents all possible paths of the field ψ, A_μ is a continuum field and S is called the Wilson gauge action which provides the simplest form of a gauge action on the lattice. The continuum form of the Wilson gauge is given by:

$$S \;=\; \int d^4x \; \frac{1}{4g_{tot}^2} F_a^{\mu\nu} F^a_{\mu\nu}, \tag{2.8}$$

where g_{tot} is the bare coupling constant in the lattice scheme. The lattice gauge theory is defined on $4D$ Euclidean lattices. The gauge field is defined on links connecting the nearest neighboring sites. Gluons live on links (Wilson Lines) as $SU(3)$ matrices and quarks live on sites as 3-vectors. By replacing space-time with the lattice, the Wilson gauge action is given by the product of gauge links around sites [14]:

$$S = \beta \sum_{x,\mu,\nu} \left[1 - \frac{1}{3} \mathrm{Re} \left(\mathrm{Tr} \big[U_\mu(x) U_\nu(x - a\widehat{\mu}) U^\dagger_\mu(x + a\widehat{\mu}) U^\dagger_\nu(x) \big] \right) \right], \tag{2.9}$$

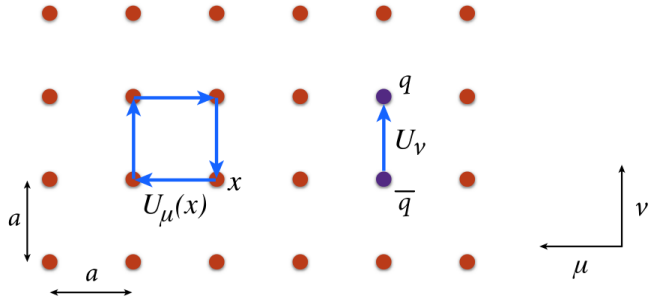

Figure 2.6: Sketch of a two-dimensional slice of the $\mu - \nu$ plane of the lattice. The lattice spacing is indicated by a. Gluon fields lying on links ($U_\mu(x)$, U_ν), appearing either the gauge action or a component of the covariant derivative connecting quark and antiquark fields [14].

where $U_\mu(x)$ and $U_\nu(x)$ are gluon fields, x is the Euclidean space-time position, $\widehat{\mu}$ the unit vector in the μ'th direction and $\beta = \frac{6}{g_{tot}}$, where g_{tot} is the bare coupling constant in the lattice scheme. This is illustrated in Figure 2.6.

Assuming the fields are varying slowly and the a value is small, one can expand the action in powers of a using $U_\mu(x) = e^{iaA_\mu(x)}$. Results for physical observables are obtained by calculating expectation values:

$$\mathcal{O} \;=\; \frac{1}{Z}\int \mathcal{D}A_\mu \; \mathcal{O}\; e^{-S}\;, \tag{2.10}$$

where $\mathcal{O}$ is called the correlation function, which is any given combination of operators expressed in terms of time-ordered products of gauge and quark fields.

2.4.2.2 Charmonium states below the open-charm threshold

In lattice calculations, charmonium masses are extracted from two-point correlation functions [13]:

$$C_{ij}(t) = \langle\Omega|\mathcal{O}_i(t)\mathcal{O}_j^\dagger(0)|\Omega\rangle = \sum_n Z_i^n Z_j^{n*}\; e^{-E_n t}\;, \qquad Z_i^n \equiv \langle\Omega|\mathcal{O}_i|n\rangle\;. \tag{2.11}$$

The physical system for given quantum numbers J^{PC}, is created from the vacuum $|\Omega\rangle$ using an interpolator $\mathcal{O}_j^\dagger$ at time t=0 and the system propagates for time t before being annihilated by $\mathcal{O}_i$. E_n is the eigenstate of $|n\rangle$ and Z_j^n is the vacuum-state matrix

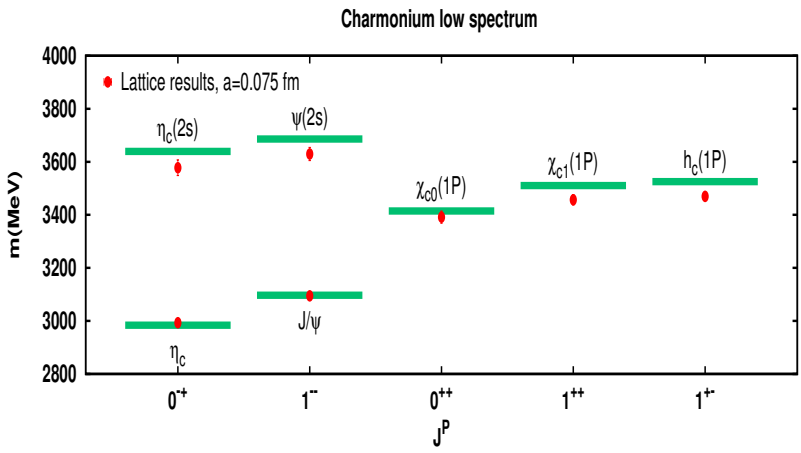

Figure 2.7: Charmonium spectrum for the states below the open-charm threshold. Experimentally determined masses (green lines) are compared to predictions from LQCD (red dots). This figure is taken from reference [12].

element, which are referred to as overlaps. The correlators are evaluated on the lattice and their time dependence allows to extract E_n and Z_n^i [9, 10]. For the states below the open-charm threshold, the masses are extracted from the energies obtained with $c\bar{c}$ extrapolating fields, which are extrapolated to $a \to 0.075$ fm, $V \to \infty$ and $m_q \to m_q^{phys}$. The latest results of the charmonium spectrum from LQCD are shown in Figure 2.7. At first inspection, there is good agreement between LQCD calculations and the measurements.

2.4.3 Potential models (NR, MNR)

Since the mass of the charmonium bound state is larger than the mass of each of the quarks, the velocity of the charm quarks in charmonium is around $v^2 \approx 0.3$, so that the charmonium system can be treated using a non-relativistic basis with some sophisticated relativistic corrections. The computation can then be approximated by an expansion in powers of v/c and v^2/c^2. This technique is called non-relativistic QCD (NRQCD). The mesonic dynamics in a non-relativistic approximation is governed by a Hamiltonian which is composed of two parts: a kinetic energy term T and a potential energy term V which takes into account the phenomenological interaction between the quark and the antiquark:

$$H = T + V. \tag{2.12}$$

The mesonic wave functions are obtained from the eigenfunctions of the Schrödinger equation:

$$\widehat{H}\psi = E\psi \ . \tag{2.13}$$

The non-relativistic expression for the energy is given by [28]:

$$T = m_1 + m_2 + p^2/2\mu, \tag{2.14}$$

where m_1 and m_2 are the constituent masses of the quark and the antiquark respectively, μ is the reduced mass for the system, and p is the relative momentum. Although many different potentials exist, the one most often referred to and the simplest one is the Cornell potential [33], which addresses the two main concepts in QCD, namely asymptotic freedom and quark confinement. It consists of a Coulomb-like term representing one-gluon exchange at small distances and a linear term, representing multi-gluon exchanges that will force quarks to be confined in hadrons and mesons:

$$V_{NR}^{(0)} = -\frac{4}{3}\frac{\alpha_s(r)}{r} + kr, \tag{2.15}$$

where r is the radius of charmonium and α_s is the QCD coupling constant. Besides the Coulomb and confinement term, the potential should also include the hyperfine interaction giving rise to an additional $\vec{S}_c \cdot \vec{S}_{\bar{c}}$ term [32]:

$$V_{NR}^{(1)}(r) = -\frac{4}{3}\frac{\alpha_s(r)}{r} + kr + \frac{32\pi\alpha_s}{9m_c^2}\tilde{\delta}_\sigma(r)\vec{S}_c \cdot \vec{S}_{\bar{c}}, \tag{2.16}$$

where $\widetilde{\delta}_\sigma(r) = \frac{\sigma}{\sqrt{\pi^3}}\ e^{-\sigma^2 r^2}$ and the four parameters $(\alpha_s, m_c, k, \sigma)$ can be determined by fitting the charmonium mass spectrum. The hyperfine interaction term is also predicted by One-Gluon Exchange (OGE) forces [31]. The potential given in equation 2.16 can be further extended with two more terms, namely spin-orbit and tensor components. The spin-orbit term $(\vec{L} \cdot \vec{S})$ and the tensor $(\vec{T})$ term can be directly derived from the standard Breit-Fermi expression to order v^2/c^2. Taking all components into account, the interaction potential becomes [29]:

$$V_{NR}^{(2)}(r) = -\frac{4}{3}\frac{\alpha_s}{r} + k\,r + \frac{32\pi\alpha_s}{9m_c^2}\tilde{\delta}_\sigma(r)\vec{S}_c \cdot \vec{S}_{\bar{c}} + \left[\frac{2\alpha_s}{m_c^2 r^3} - \frac{b}{2m_c^2 r}\right]\vec{L} \cdot \vec{S} + \frac{4\alpha_s}{m_c^2 r^3}\vec{T}, \tag{2.17}$$

where L is the orbital momentum and S is the spin of the charmonium states with:

$$\langle \vec{S}_c \cdot \vec{S}_{\bar{c}} \rangle = \frac{1}{2}S(S+1) - \frac{3}{4}, \tag{2.18}$$

$$\langle \vec{L} \cdot \vec{S} \rangle = \frac{1}{2}\left[J(J+1) - L(L+1) - S(S+1)\right], \tag{2.19}$$

$$\left\langle \vec{T} \right\rangle = -\frac{6\left(\langle \vec{L}\cdot\vec{S}\rangle\right)^2 + 3\langle \vec{L}\cdot\vec{S}\rangle - 2S(S+1)L(L+1)}{6(2L-1)(2L+3)}. \tag{2.20}$$

The confinement of quarks is assumed to be purely scalar linear type in the NR model and scalar-vector mixing linear in a modified non-relativistic (MNR) model. The mass spectrum and electromagnetic processes of the charmonium system are studied taking in to account the spin-dependent potentials in the solution of the Schrödinger equation and the results for the pure scalar and scalar-vector mixing linear confining potentials [29]. It is argued that the inclusion of relativistic corrections for a pure scalar or vector confining potential is not enough to bring theoretical predictions into agreement with experiment. The MNR results obtained by considering the specific mixture of these potentials with the mixing coefficient, ϵ which stands for the vector exchange scale. The ϵ value is fixed from the analysis of heavy quarkonium masses and radiative decays [21]. The confining and interaction potentials in MNR model are given by $V^{(0)}_{MNR}$ and $V^{(2)}_{MNR}$, respectively:

$$V^{(0)}_{MNR} = b(1-\epsilon)r - \frac{4}{3}\frac{\alpha_s}{r} + \epsilon br, \tag{2.21}$$

$$V^{(2)}_{MNR} = -\frac{4}{3}\frac{\alpha_s}{r} + b\,r + \frac{32\pi\alpha_s}{9m_c^2}\tilde{\delta}_\sigma(r)\vec{S}_c\cdot\vec{S}_{\bar{c}} + \left[\frac{2\alpha_s}{m_c^2 r^3} + \frac{(4\varepsilon-1)b}{2m_c^2 r}\right]\vec{L}\cdot\vec{S} + \left[\frac{\alpha_s}{3m_c^2 r^3} + \frac{\varepsilon b}{12m_c^2 r}\right]\vec{T}, \tag{2.22}$$

All the masses of the states below the open-charm threshold which are calculated with the two potential models are summarized in table 2.1 and were taken from [29].

2.4.4 Effective Field Theories (EFT)

An Effective Field Theory (EFT) is a very powerful tool in quantum field theory [36]. It provides a systematic formalism for the analysis of multi-scale problems. This is particularly important in QCD, where the value of the running coupling $\alpha_s(\mu)$ can change significantly between different energy scales. An EFT can approximate the full QCD when applied to a bound state containing more than one heavy quark. One of the main advantages of an EFT is that this is a theory of the dynamics of the system at energies small compared to a given cutoff. For some systems, low-energy states with respect to this cutoff are effectively independent of states at high energies. Hence, one may study the low-energy sector of the theory without the need for a detailed description of the high-energy sector.

State	Expt. [48]	Potential model [29]	
		NR	MNR
$\eta_c(1^1S_0)$	2983.4 ± 0.5	2990.4	2978.4
$J/\Psi(1^3S_1)$	3096.916 ± 0.006	3085.1	3087.7
$\eta_c'(2^1S_0)$	3639.2 ± 1.2	3646.5	3646.9
$\psi'(2^3S_1)$	3686.097 ± 0.025	3682.1	3684.7
$\chi_2(1^3P_2)$	3556.20 ± 0.09	3551.4	3559.3
$\chi_1(1^3P_1)$	3510.66 ± 0.07	3500.4	3517.7
$\chi_0(1^3P_0)$	3414.75 ± 0.31	3351.9	3366.3
$h_c(1^1P_1)$	3525.38 ± 0.11	3514.6	3526.9

Table 2.1: An overview of the results from theoretical calculations based on NR and MNR potential models for the mass of states below the open-charm threshold. The results are compared with experimental measurements.

The main idea of an EFT is simple. Consider a quantum field theory with a large, fundamental scale M. This could be the mass of a heavy particle or some large momentum transfer. Choose a cutoff $\Lambda < M$ and divide the fields of the theory into low-frequency and high-frequency modes:

$$\phi = \phi_L + \phi_H, \tag{2.23}$$

where ϕ_L contains the Fourier modes with a frequency $\omega < \Lambda$, while ϕ_H contains the remaining modes with a frequency $\omega > \Lambda$. One can consider the cutoff as a threshold of ignorance in the sense that we may pretend to know nothing about the theory for scales above Λ. Low-energy physics is described in terms of the ϕ_L fields. Everything one ever wishes to know about the theory (Feynman diagrams, scattering amplitudes, cross sections, decay rates, etc.) can be derived from vacuum correlation functions of these fields.

As non-relativistic systems, quarkonia are characterized by three energy scales, hierarchically ordered by the heavy quark velocity in the center-of-mass frame $\frac{v}{c} = \beta \ll 1$: the mass m (hard scale), the momentum transfer mv (soft scale), which is proportional to the inverse of the typical size of the system r, and the binding energy $m\beta^2$ (ultrasoft scale), which is proportional to the inverse of the typical time of the system. In the quarkonium rest frame, the heavy quarks move slowly ($\beta \ll 1$), with a typical momentum $m_Q\beta \ll m_Q$ and a binding energy $\sim m_Q\beta^2$. Hence, any study of heavy quarkonium faces a multi-scale problem with the hierarchies $m_Q \gg m_Q\beta \gg m_Q\beta^2$ and $m_Q \gg \Lambda_{QCD}$. The use of effective field theories is extremely convenient in order to

exploit these hierarchies.

2.4.4.1 EFT for conventional charmonium

The following hierarchy of scales is satisfied because of the non-relativistic nature of quarkonium [38]:

$$m \gg p \sim 1/r \sim m\beta \gg E \sim m\beta^2. \tag{2.24}$$

This allows for a description in terms of EFTs of physical processes taking place at one of the lower scales.

- Non-Relativistic QCD (NRQCD):

  Heavy quarkonium annihilation and production, which can occur at a scale m, can be described by NRQCD [39]. The effective Lagrangian is given by [38]:

  $$\mathcal{L}_{\text{NRQCD}} = \sum_n \frac{c_n(\alpha_s(m), \mu)}{m^n} \times \mathcal{O}_n(\mu, m\beta, m\beta^2, \ldots)\,, \tag{2.25}$$

  where c_n are the Wilson coefficients that encode the contributions from the scale m, μ is the NRQCD factorization scale, and $\mathcal{O}_n$ are the low-energy operators constructed out of two or four heavy-quark/antiquark fields plus gluons. The matrix elements of $\mathcal{O}_n$ depend on the scales μ, $m\beta$, $m\beta^2$ and Λ_{QCD}. Thus, the operators are counted in powers of β.

- potential Non-Relativistic QCD (pNRQCD):

  Heavy quarkonium formation, which can occur at scale mv, can be described by pNRQCD [40]. The pNRQCD Lagrangian inherited from NRQCD, but in addition as a multipole expansion in r is given by [38]:

  $$\mathcal{L}_{\text{pNRQCD}} = \int d^3r \sum_n \sum_k \frac{c_n(\alpha_s(m), \mu)}{m^n} V_{n,k}(r, \mu', \mu)\, r^k \times \mathcal{O}_k(\mu', m\beta^2, \ldots)\,, \tag{2.26}$$

  where $\mathcal{O}_k$ are the operators of pNRQCD that depend on the scales μ', mv^2 and Λ_{QCD}; the pNRQCD factorization scale is μ', and $V_{n,k}$ are the Wilson coefficients that encode the contributions from the scale r.

2.4.5 Quark model

The constituent quark was introduced over 50 years ago as a purely phenomenological entity to allow for a description of color singlet hadrons as bound states of smaller size objects, baryons as $3q$ or $3\bar{q}$ and mesons as $q\overline{q}$ states with q as constituent quarks.

At scales larger than the confinement scale $\Lambda_{QCD} \approx 200$ MeV, it is realized that the constituent mass is a consequence of the chiral-symmetry breaking in the light quark sector. Due to this breaking, the quark propagator gets modified and quarks acquire a dynamical momentum-dependent mass. The Lagrangian describing this scenario contains chiral fields to compensate the mass term. The simplest Lagrangian which contains chiral fields to compensate the mass term can be expressed as [34]:

$$\mathcal{L} = \overline{\psi}(i\,\partial\!\!\!/ - M(q^2)U^{\gamma_5})\,\psi, \tag{2.27}$$

where $U^{\gamma_5} = \exp(i\pi^a\lambda^a\gamma_5/f_\pi)$ is a Goldstone boson field matrix, λ^a are $SU(3)$ color matrices, π^a denotes nine pseudoscalar fields $(\eta_0, \vec{\pi}, K_i, \eta_8)$ with i =1,...,4 and $M(q^2)$ is the constituent mass. This constituent quark mass, which vanishes at large momenta and is frozen at low momenta at a value around 300 MeV, can be explicitly obtained from the theory, but its theoretical behavior can be simulated by parametrizing $M(q^2) = m_q F(q^2)$ where $m_q \simeq 300$ MeV, and

$$F(q^2) = \left[\frac{\Lambda^2}{\Lambda^2 + q^2}\right]^{\frac{1}{2}}. \tag{2.28}$$

The cutoff Λ fixes the chiral-symmetry-breaking scale.

2.5 Basic properties of the η_c

The width of the lowest lying charmonium state η_c, shows large systematic uncertainties when comparing data from various experimental methods. The comparison between the results from different experimental groups for the width of the η_c is shown in Figure 2.8. The data sets are not internally consistent considering the large spread and their uncertainties. Part of the discrepancy could be due to the interpretation of the line shape of the reconstructed η_c which was in many cases based on a simple Breit-Wigner distribution due to limited statistics in the experiment.

Among all these measurements, only BESIII and KEDR considered the interference of the η_c with a non-resonant background. These results are shown with the green

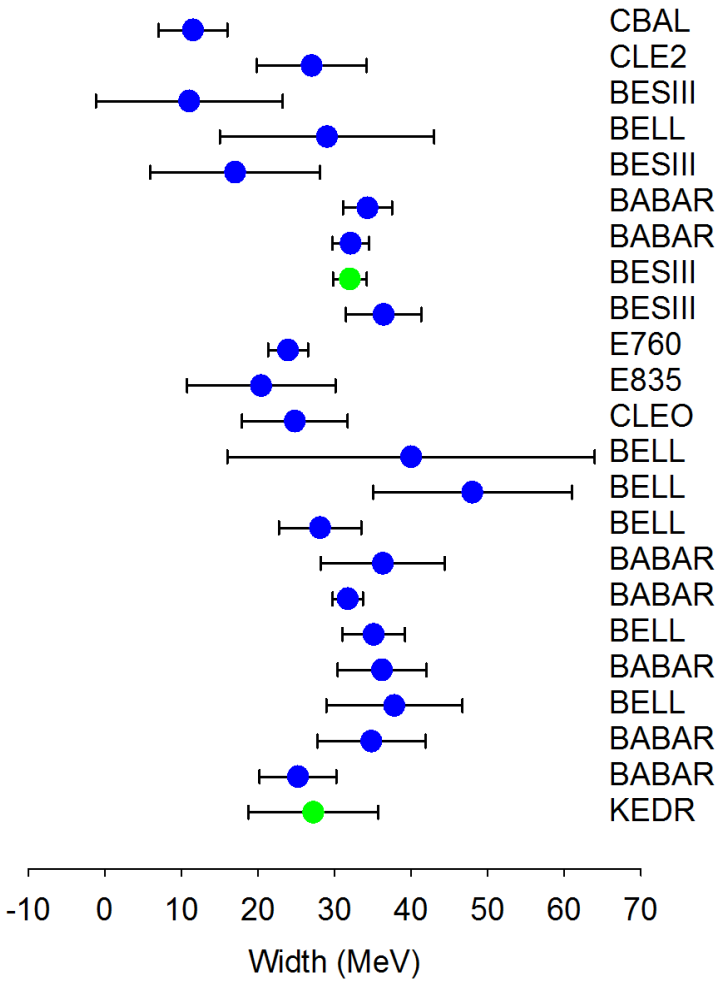

Figure 2.8: All existing measurements related to the width of the η_c [48]. The results with (without) considering the effect of interference between signal and non-resonant background are shown with green (blue) circles.

circles. The interference may clarify the discrepancy between older experiments, since interference affects the observed mass and the width of η_c. It motivated us to look at the line shape of η_c more systematically through two decay modes, $J/\psi \to \gamma\eta_c$ and $\psi^{'} \to \gamma\eta_c$ which are explained in more detail in chapters 5 and 6, respectively.

2.6 Overview of different experimental methods

To make a comparison between the theoretical calculations and experimental measurements, a summary of some of the experiments that measured the partial width of $J/\psi(\psi^{'}) \to \gamma\eta_c$ and the mass of the η_c are given here.

• CBALL:

The branching fraction of $J/\psi \to \gamma\eta_c$ was measured for the first time by CBALL in 1980 via the inclusive photon spectrum which was based on 2.2×10^6 events. The factor E_γ^3 is included in the convolution of the detector response function with the η_c Breit-Wigner resonance shape. Three sources of backgrounds were considered for this analysis which are photon background, charged particle contribution and the contribution of $\psi^{'} \to \eta J/\psi \to \gamma\gamma J/\psi$ decay. An interference with a non-resonant background was not considered in this analysis, and mass and width were taken as free parameters. This analysis resulted in $\Gamma(J/\psi \to \gamma\eta_c) = 1.17 \pm 0.32$ keV [44]. For more than twenty years, the Particle Data Group (PDG) value was based only on this single CBALL result.

The same fitting method as $J/\psi \to \gamma\eta_c$ was used for $\psi^{'} \to \gamma\eta_c$ except the E_γ^3 was replaced with E_γ^7 since $\psi^{'} \to \gamma\eta_c$ is a hindered M1 transition. The result was $\Gamma(\psi^{'} \to \gamma\eta_c) = 0.83 \pm 0.22$ keV.

Through this analysis the mass of the η_c was obtained to be 2984.3 $\pm$ 2.3 $\pm$ 4.0 MeV/c^2.

• CLEOc (2009):

In 2009, the CLEOc collaboration published the result of a new measurement in which 12 exclusive decay modes of the η_c were analyzed. A series of exclusive decay modes of the η_c were used to constrain the line shape for the inclusive spectrum. To measure $\mathcal{B}r(J/\psi \to \gamma\eta_c)/\mathcal{B}r(\psi^{'} \to \gamma\eta_c)$, the ratio of events in the following chains were taken:

$$\psi^{'} \to \pi^+\pi^- J/\psi;\ J/\psi \to \gamma\eta_c;\ \eta_c \to X_i, \tag{2.29}$$

$$\psi^{'} \to \gamma\eta_c;\ \eta_c \to X_i, \tag{2.30}$$

where the X_i are exclusive decay modes of the η_c. To minimize the systematic error, $\mathcal{B}r(J/\psi \to \gamma\eta_c)$ is taken to be the product of $\mathcal{B}r(\psi^{'} \to \gamma\eta_c)$ with $\mathcal{B}r(J/\psi \to \gamma\eta_c)/\mathcal{B}r(\psi^{'} \to \gamma\eta_c)$, rather than using the inclusive photon spectrum from J/ψ decays. Fits to the resulting photon energy spectrum for the sum of all η_c decay modes are

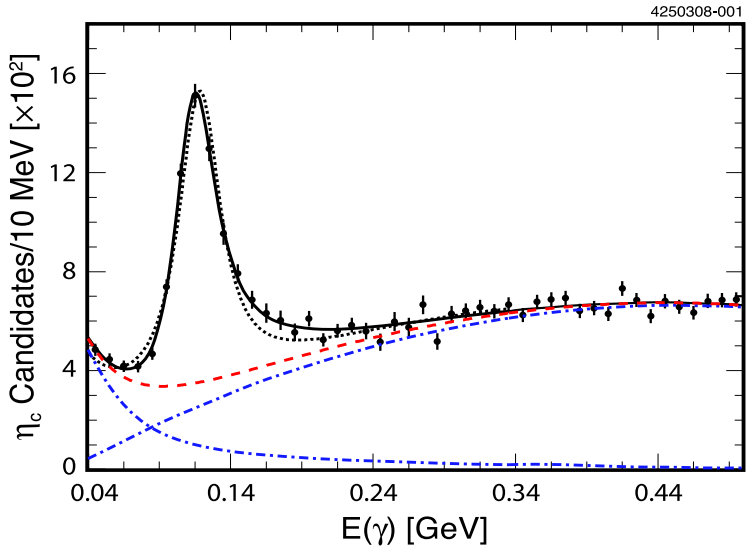

Figure 2.9: The CLEO fit to the photon spectrum in exclusive $J/\psi \to \gamma\eta_c$ decays using relativistic Breit-Wigner (dotted) and modified (solid) signal line shapes convoluted with a 4.8 MeV wide resolution function. Total background is given by the dashed line. The dot-dashed curves indicate two major background components described in the text [80]

shown in Figure 2.9. The background shape has two features. The background that falls with energy from $J/\psi \to X_i$ and a rising background from both $J/\psi \to \gamma X_i$ and $J/\psi \to \pi^0 X_i$ that is freely fit to a second-order polynomial. A fit using a relativistic Breit-Wigner distribution modified by a factor of E_γ^3 improves the fit around the peak but leads to a diverging tail at higher energies (not shown). To damp the E_γ^3, an additional factor of $\exp(-E_\gamma^2/\beta^2)$ is added [80]. A distortion in the η_c line shape was observed and it is attributed to the photon energy dependence of the magnetic dipole transition rate. The conclusion was that the η_c mass is sensitive to the line shape, suggesting an explanation for the discrepancy between measurements of the η_c mass from older experiments. The obtained value is $\Gamma(J/\psi \to \gamma\eta_c) = 1.83 \pm 0.08 \pm 0.19$ keV [80].

The same method of fitting as $J/\psi \to \gamma\eta_c$ was used for the $\psi' \to \gamma\eta_c$. Since $\psi' \to \gamma\eta_c$ is a hindered M1 transition, the E_γ^3 factor was replaced with E_γ^7. The result of this analysis was $\Gamma(\psi' \to \gamma\eta_c) = 1.28 \pm 0.06 \pm 0.17$ keV.

Through this analysis the mass of the η_c was found to be 2982.2 ± 0.6 MeV/c^2.

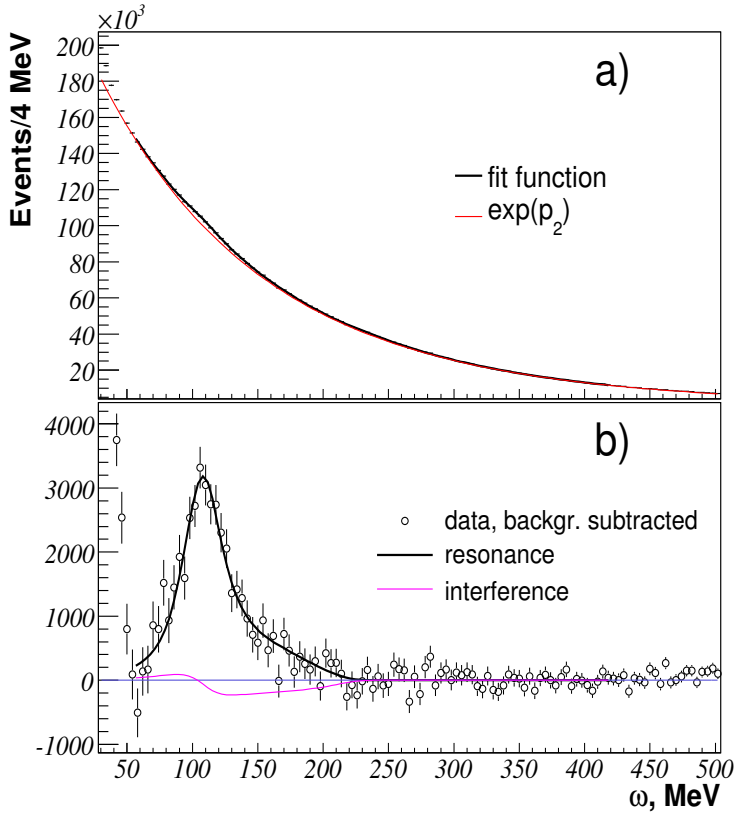

Figure 2.10: a) The KEDR fit of the inclusive photon spectrum in the energy range 55-420 MeV; b) The photon spectrum after background subtraction [45].

• KEDR:

Recently, the decay rate of $J/\psi \to \gamma\eta_c$ was measured by KEDR using the inclusive photon spectrum based on a 6 million data sample. In this analysis, the interference between the signal and a non-resonant background, $J/\psi \to \gamma gg \to \gamma X$ decays, was considered. The inclusive photon spectrum and its fit are shown in figure 2.10 and were taken from reference [45]. The spectrum was fitted with a sum of the signal, a relativistic Breit-Wigner distribution, convoluted with the calorimeter response function, and background. The background has the following shape:

$$dN/d\omega = \exp(p_2(\omega)) + c \times \mathrm{MIP}(\omega), \tag{2.31}$$

where $p_2(\omega)$ is a second-order polynomial and $\mathrm{MIP}(\omega)$ is the spectrum of charged parti-

cles. The phase ϕ, mass and width of η_c were allowed to vary freely giving the following values $\phi = (-4 \pm 54)^\circ$ and $\Gamma(J/\psi \to \gamma\eta_c) = 2.98 \pm 0.18^{+0.15}_{-0.33}$ keV [45]. The conclusion of this analysis related to interference was that the value of the obtained phase $\phi = (-4 \pm 54)^\circ$ is close to zero, therefore the interference changes the measured value only slightly.

Through this analysis the mass of the η_c was found to be $2983.5 \pm 1.4^{+1.6}_{-3.6}$ MeV/c^2.

• CLEOc (2004):

In 2004, CLEOc measured the $\Gamma(\psi^{'} \to \gamma\eta_c)$ based on 1.6 M $\psi^{'}$ decays through the decay mode of $\psi^{'} \to \gamma\eta_c$, $\eta_c \to X_i$. A Breit-Wigner convoluted with the Crystal-Ball function was used to describe the signal line shape. Since the fitted peak amplitude depends strongly on the assumed natural width of the η_c, they assumed $\Gamma_{\eta_c} = 24.8 \pm 4.9$ MeV, coming from their own determination via the formation in $\gamma\gamma$ fusion [51]. They factored out the Γ_{η_c} dependence, and the photon background under the peak was described by a 4^{th} order polynomial. The result of this analysis was $\Gamma(\psi^{'} \to \gamma\eta_c) = 0.95 \pm 0.15 \pm 0.21$ keV.

Through this analysis the mass of the η_c was found to be $2981.8 \pm 1.3 \pm 1.5$ MeV/c^2.

2.7 Comparison between theory and experiment

To give an overview of both experimental and theoretical efforts in the past decades, the various calculations for hyperfine splitting and decay width of M1 transitions will be compared with the published experimental results.

2.7.1 Hyperfine splitting

The hyperfine splitting between spin-singlet $S = 0$ and spin-triplet $S = 1$ states that arises due to magnetic interactions between the spins is important to study since it gives access to the spin-spin interaction term in confinement potential. The S-wave hyperfine splitting of charmonium is given by:

$$\Delta M_{hf}(S) = M_{J/\psi} - M_{\eta_c}. \tag{2.32}$$

Theoretical calculations related to hyperfine splitting are compared with experimental measurements in table 2.2. Since the mass of the J/ψ, $M_{J/\psi}$, is determined with high

Theoretical calculations of hyperfine splitting (MeV)	
Lattice QCD (2009) [55]	$116.0 \pm 7.4^{+2.6}_{-0.0}$
Lattice QCD (2012) [22]	$116.5 \pm 2.1 \pm 2.4$
Lattice QCD (2013) [15]	$116.2 \pm 1.4 \pm 2.8$
Lattice QCD (2015) [54]	113.8 ± 0.8
NR potential model [29]	108
GI [47]	113
Experimental measurements of hyperfine splitting (MeV)	
BELLE [25]	$111.5^{+2.5}_{-1.6}$
BESIII [26]	112.6 ± 0.9
PDG 2016 [48]	113.3 ± 0.7

Table 2.2: Theoretical calculations and experimental measurements of the hyperfine splitting in charmonium.

precision, as it can be populated directly in e^+e^- collisions, the discrepancy between theoretical and experimental values is mostly related to the precision of M_{η_c}. It confirms the consistency problem of the M_{η_c} which is explained in subsection 2.5 and it is another motivation to look at the line shape of the η_c via $\psi^{'} \to \gamma\eta_c$ and $J/\psi \to \gamma\eta_c$.

2.7.2 Partial width of $J/\psi \to \gamma\eta_c$

There are a lot of theoretical predictions for this decay rate, some of which were discussed earlier. A comparison between theoretical predictions and experimental data is given in table 2.3. This comparison shows the discrepancies between theoretical predictions and experimental measurements. The role of interference effects in this analysis is one of the key points to be checked since it can influence the line shape and the decay rate measurement as well. Among the older experiments, only KEDR considered this effect, so a more detailed study of the η_c line shape is needed to investigate the effect of an interference. As BESIII has the largest data sample of J/ψ and $\psi^{'}$ decays, it provides the opportunity to study the η_c line shape to shed light on the effect of the interference for $\Gamma(J/\psi \to \gamma\eta_c)$.

2.7.3 Partial width of $\psi^{'} \to \gamma\eta_c$

A summary of all the theoretical predictions and experimental measurements is given in table 2.4. It is to be noted that in general the systematic error dominates in most of the experimental results. To improve the results, further experimental studies are

Theoretical calculations for $\Gamma(J/\psi \to \gamma\eta_c)$ (keV)	
Lattice QCD (2013) [18]	$2.64 \pm 0.11 \pm 0.03$
Lattice QCD (2012) [22]	$2.49 \pm 0.18 \pm 0.07$
Lattice QCD (2009) [17]	2.51 ± 0.08
NR potential model [29]	1.5
MNR potential model [29]	2.2
pNREFT [41]	2.12 ± 0.40
Quark model [35]	1.25
EFT (average) [41], [42]	1.5 ± 1.0
GI [47]	2.4
Experimental measurements for $\Gamma(J/\psi \to \gamma\eta_c)$ (keV)	
CBALL [44]	1.17 ± 0.32
CLEOc [80]	$1.83 \pm 0.08 \pm 0.19$
KEDR [45]	$2.98 \pm 0.18^{+0.15}_{-0.33}$
PDG value [48]	1.28 ± 0.32

Table 2.3: Theoretical calculations and experimental measurements of partial widths (keV) of the M1 radiative transitions for $J/\psi \to \gamma\eta_c$.

Theoretical calculations for $\Gamma(\psi' \to \gamma\eta_c)$ (keV)	
Lattice QCD [22]	0.4 ± 0.8
NR potential model [29]	3.1
MNR potential model [29]	3.8
Quark model [35]	2.41
GI [47]	2.6
Experimental measurements for $\Gamma(\psi' \to \gamma\eta_c)$ (keV)	
CBALL [44]	0.83 ± 0.22
CLEOc-2004 [50]	$0.95 \pm 0.15 \pm 0.21$
CLEOc-2009 [80]	$1.28 \pm 0.06 \pm 0.17$
PDG value [48]	1.01 ± 0.17

Table 2.4: Theoretical calculations and experimental measurements of partial widths (keV) of the M1 radiative transitions for $\psi' \to \gamma\eta_c$.

needed. By using the world's largest sample of ψ' decays which is collected by BESIII, we will obtain the branching fraction of $\psi' \to \gamma\eta_c$ inclusively without any dependence on the η_c branching fraction.

The theoretical predictions in the framework of GI and NR potential models notably overestimate the experimental observations. It should be emphasized that the intermediate hadronic meson loop might provide explicit corrections to the $\psi' \to \gamma\eta_c$ process.

Such a mechanism turns out to be important for exclusive transitions, especially when the mass of the initial-state is close to the open-charm threshold [53]. More studies of the $\psi^{'}$ M1 transition, $\psi^{'} \to \gamma\eta_c$, are needed on both theoretical and experimental arenas.

Chapter 3

The BESIII experiment

The goal of this chapter is to present the main characteristics of the Beijing Electron-Positron Collider (BEPCII) and the Beijing Spectrometer (BESIII) with a detailed description of its sub-detectors in light of the physics that is being explored. These facilities are located at the Institute of High Energy Physics (IHEP) of the Chinese Academy of Science (CAS) in West Beijing and is one of the largest comprehensive fundamental research centers in China [56].

3.1 The physics program of BESIII

The aim of BESIII is to study fundamental questions of Quantum Chromodynamics (QCD), aiming to improve our understanding of the transition between the perturbative and the non-perturbative QCD regions. QCD, the fundamental theory of the strong interaction, is well tested at energies higher than $\Lambda_{QCD} \approx 200$ MeV, but below this energy, non-perturbative effects become important and these are not well understood yet. Experimentally, efforts have been targeted to study those unknown features of QCD. In principle, particle colliders at low energies can address some of those questions. The Beijing Electron Positron Collider (BEPCII) running at a center-of-mass energy from 2 GeV to 4.6 GeV is ideal, because it runs at the energy range at which physics can be probed at the overlap between long and short distance scales. In addition, many theoretical predictions have been obtained and call for confirmations or tests from the experimental side at the energy scale relevant to BEPCII.

The physics topics of BESIII and the research opportunities provided by BEPCII are:

- Charmonium decays and their transitions;
- Open-charm physics;

- τ mass;
- Light hadronic physics;
- Hybrids, glueballs and other exotics.

3.2 BEPCII facility

BESIII is located on the campus of IHEP in Beijing, China and BEPCII is used to collide electrons with positrons. These were built on the site of the previous BES detectors and the original BEPC collider. The BES detector was upgraded in 1996 to the BESII detector, and BEPC was upgraded throughout the years as well, until it was closed in 2004. At its peak, BEPC was able to deliver an instantaneous luminosity of 10^{31} cm^{-2} s^{-1}. The BESIII detector was commissioned along with BEPCII in order to take advantage of the new detector technology and the greatly increased luminosity of up to 10^{33} cm^{-2} s^{-1} provided by the upgrade to BEPCII [134] in 2007. The e^+e^- collision rate and particle detection capabilities provided by BEPCII and BESIII, respectively, allow for many important measurements and searches for rare decays in the τ-charm energy region.

3.2.1 BEPCII accelerator

BEPCII is a double-ring collider (see Figure 3.1) built within the existing BEPC tunnel. Almost all components have been replaced in order to meet the design parameters for a successful execution of the BESIII physics program. To obtain a high integrated luminosity, BEPCII provides a high instantaneous luminosity, along with efficient running. Many tightly spaced bunches of electrons and positrons enable high beam currents. BEPCII operates with 93 bunches in each ring. Each bunch is about 1.5 cm long and separated by 8 ns (2.4 m) from the next bunch, giving a single-beam current of 0.91 A when running in collision mode. The beams collide at the interaction point (IP) with a crossing angle of 11 milliradians and are focused by super-conducting quadrupole magnets near the IP using the micro-β technique to compress the vertical beam size to about 5.7 μm. The horizontal beam size is about 380 μm. The main design parameters of the BEPCII collider are summarized in Table 3.1.

The design luminosity is two orders of magnitude larger than its predecessor and it is optimized for 2×1.89 GeV center-of-mass energy, just above the open-charm threshold [134].

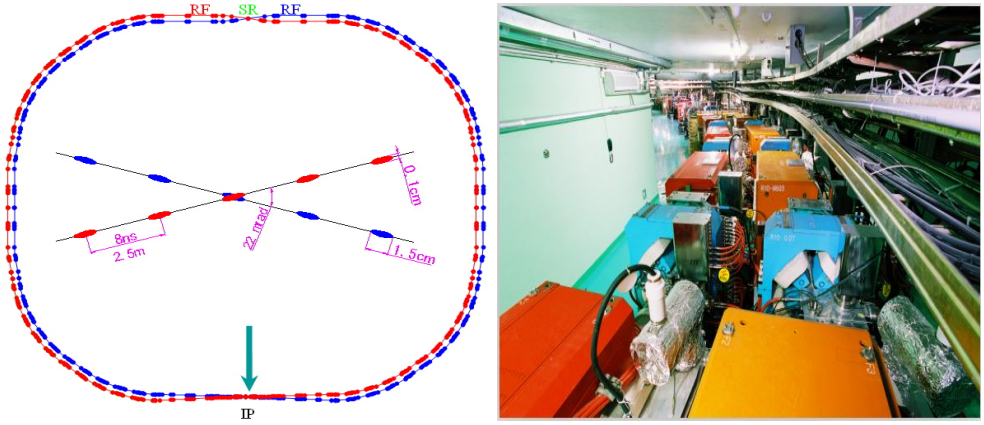

Figure 3.1: Left: The schematic view of BEPCII. Right: A picture of the double rings.

Design parameters of the BEPCII	
$\sqrt{s}$ (GeV)	2 - 4.6
Circumference (m)	237.5
RF frequency (MHz)	499.8
Number of bunches	2×93
Beam current (mA)	2×910
Bunch length σ_z (cm)	1.5
Bunch size ($\sigma_x \times \sigma_y$) (μm)	$\sim 380 \times \sim 5.7$
Crossing angle (mrad)	± 11
luminosity ($\mathrm{cm}^{-2}\ \mathrm{s}^{-1}$)	$1 \cdot 10^{33}$

Table 3.1: Design parameters of the BEPCII collider [134].

3.2.2 Storage ring

To take data with the BESIII detector, electrons and positrons must be circulating in the BEPCII storage rings. Initially, positrons are created by firing electrons at a fixed target. The positrons are created in e^+e^- pairs from photons which interact with the target material. The positrons are then separated magnetically, accelerated, and finally injected into the positron storage ring. Once the positrons in the storage ring have reached the desired beam current, the electrons are injected. Electron injection proceeds much more quickly because they do not have to be created indirectly, as the positrons do, but only accelerated and injected. The positron (electron) current in the ring increases at a rate of 50 mA/min (200 mA/min) due to injection. After injection, the e^+e^- beams collide and data are taken by BESIII [134].

3.3 BESIII detector

The BESIII detector is the second update of the original BES detector, with construction finished in Summer 2008. The BESIII detector, shown in Figure 3.2, is centered around the IP of the colliding e^+ and e^- beams. Within this thesis, a right-handed coordinate system is chosen at the interaction point (IP), (x, y, z = 0, 0, 0). The spherical coordinates are obtained by following standard conventions from Cartesian coordinates. The interactions between the e^+ and e^- beams take place within the beam-pipe, which has an inner radius of 31.5 mm and an outer radius of 57 mm [57]. Like every currently operating detector for high-energy physics measurements, BESIII has an onion-like design with several sub-detectors for measuring specific particle properties. Its main components are the following (see Figure 3.2):

- Main Drift Chamber (MDC):
  MDC measures the tracks of charged particles and provides a measurement of the specific energy loss, dE/dx.

- Time-Of-Flight (TOF):
  TOF is used for identification of charged particles.

- Electromagnetic Calorimeter (EMC):
  EMC is designed to measure the energies and angular distributions of neutral and charged particles.

- Muon identifier (MU):
  The MU information is not really applicable for kaon and proton identification. The output can separate muons from hadrons quite clearly.

- Superconducting solenoid magnet (SC magnet):
  The uniform axial magnetic field allows a measurement of the momentum of a charged particle.

BESIII officially started data taking in 2009 and has been running smoothly over the past 8 years.

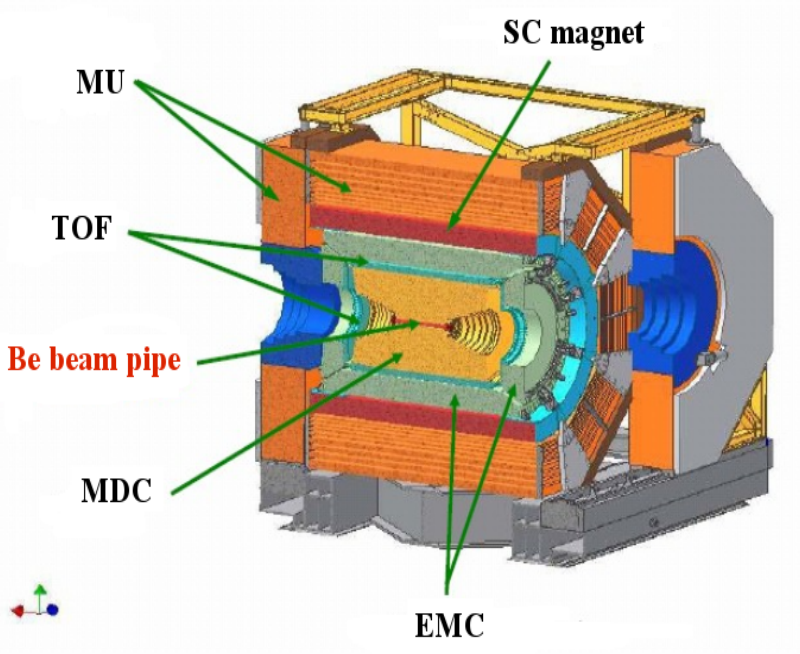

Figure 3.2: Schematic overview of the BESIII detector.

3.3.1 Superconducting solenoid magnet (SC magnet)

The SSM provides a uniform axial magnetic field with a strength of 1.0 Tesla to allow a measurement of the momentum of a charged particle. It encloses the 3 innermost sub-detectors; the inner radius is 1.38 m and limited by the EMC, the outer one is 1.7 m. The SSM is cooled with liquid He down to a temperature of 4.5 K and has a nominal current of 3369 A [97].

3.3.2 Main Drift Chamber (MDC)

By observing the detector from the inside to the outside, the first system one encounters is the MDC. This sub-detector can determine the charge and momentum of charged particles by measuring its helical trajectory and energy deposition in a well-known magnetic field of 1 T. The MDC also provides level 1 triggers, described in Section 3.4, to sort online physics events from the various backgrounds.

The MDC is a gas-filled chamber that tracks charged particles passing through its

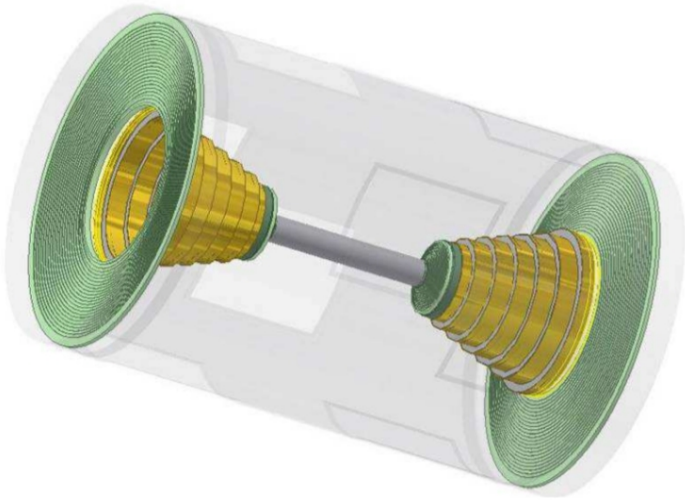

Figure 3.3: Schematic view of the MDC [58].

volume by measuring the ionization they cause. The ion-electron pairs created when a charged particle passes through are prevented from recombining by a large electric field applied to the drift chamber.

The MDC has a gas mixture of He:C_3H_8 in a ratio of 60:40; this mixture assures efficiency, while minimizing multiple scatterings which would degrade momentum resolution. The helium is chosen because it is the noble gas with the lowest atomic number. The C_3H_8 acts as a quenching gas which diffuses the energy of ionization through rotational, vibrational, and other means inaccessible to helium.

The MDC is used to take measurements of charged tracks in 43 layers using sense wires set at small stereo angles to allow 3-D track reconstruction of the particle's trajectory. The MDC has an inner radius of 59 mm and an outer radius of 810 mm while covering 93% of the 4π solid angle. The MDC has a multi-layer, small cell design, whereby the single cells give a position resolution better than 130 μm in the r-ϕ plane, and a position resolution of 2 mm in the beam direction at the IP. A sketch of the MDC is shown in Figure 3.3.

The MDC is also used to measure the energy loss per distance, dE/dx. The dE/dx information is used to identify the various long-lived particles because deposited energy depends on their velocity, β, and hence their mass according to the Bethe-Bloch

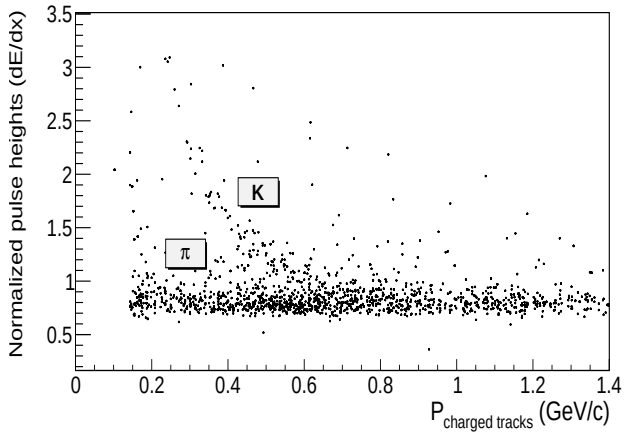

Figure 3.4: The normalized pulse heights (dE/dx) versus momentum of charged particles for the data.

formula [98]:

$$-\frac{dE}{dx} = \frac{4\pi}{m_e c^2} \times \frac{nz^2}{\beta^2} \times \left(\frac{e^2}{4\pi\epsilon_0}\right)^2 \times \left[\ln\left(\frac{2m_e c^2\beta^2}{I\cdot(1-\beta^2)}\right) - (\beta)^2\right], \tag{3.1}$$

where ϵ_0 is the vacuum permittivity, n is the electron number density of the MDC, I is the mean excitation potential for the electrons in an atom of the medium, m_e is the mass of electron and z is the atomic number. A scatter plot of a normalized dE/dx pulse heights versus momentum for various particles obtained from the Monte Carlo (MC) study is shown in Figure 3.4. The normalized pulse height is proportional to the energy loss of incident particles in the drift chamber, which is a function of momentum and mass of charged particles. Charged particles of different masses will have different velocities at the same momentum, so together with the momentum measurement, the dE/dx can give the mass information of the particle. From Figure 3.4, it can be seen that the dE/dx pulse heights can discriminate kaons and pions up to a momentum p in the order of 0.7 MeV/c.

$dE/dx_{measured}$ is compared with $dE/dx_{expected}$ and associated uncertainty for a particular particle hypothesis (σ_i) to calculate the deviation from that particle hypothesis for a single measurement and thereby providing the total MDC χ^2, where:

$$(\chi_c)^2 = \sum_i \frac{(dE_i/dx_{measured} - dE_i/dx_{expected})^2}{(\sigma_i)^2}, \tag{3.2}$$

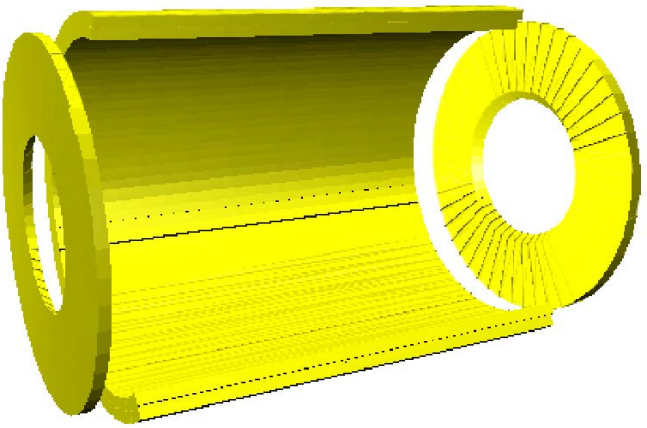

Figure 3.5: The BESIII TOF system with dual-layer barrel region and two single-layer end-cap regions [58].

and index i represents the event numbers. This information is used along with measurements from the Time-Of-Flight (TOF) system described in Section 1.3.3 to calculate the probabilities of various particle hypotheses. The dE/dx resolution is about 6% allowing a 3σ K/π separation for particles with momenta of up to 0.7 MeV/c.

3.3.3 Time-Of-Flight system (TOF)

The TOF system, shown in Figure 3.5, is composed of a dual-layer barrel region covering $|\cos\theta| < 0.83$, and two single-layer end-cap regions covering $0.85 < |\cos\theta| < 0.95$. The barrel part consists of two layers of 88 plastic scintillators, which are arranged in a cylinder around the MDC with a mean radius $\sim$ 870 mm. Each bar has a length of 2380 mm and a thickness of 50 mm. The barrel counters are read out at both ends, providing a total time resolution of 110 ps. The end-cap TOF with an inner radius of 410 mm and an outer radius of 890 mm is located behind the MDC end plate and consists of a single layer of 48 fan-shaped elements, each read out from one end by a single fine-mesh photomultiplier tube (PMT). The designed time resolution for the end-cap is 90 ps.

The TOF determines the travel time of charged particles from the IP to the TOF wall to identify the particle type. Charged particles will interact with a bunch of plastic scintillation detectors mounted on the outer surface of the MDC. The corresponding signals provide input to the level 1 trigger. Measurements are made from two different

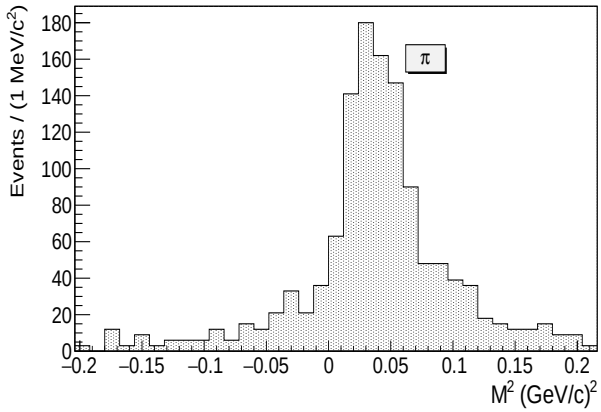

Figure 3.6: Mass-squared distribution obtained from MC using reconstructed tracks from TOF measurements for charged pions.

bands of staggered scintillation detectors attached to fine mesh PMTs; one bank is located 0.81 m from the beam-line, and the other is located 0.86 m from the beam-line.

The timing information enables a measurement of the velocity of a charged particle, which allows for separation of particles with similar momenta, but different masses. The flight time is measured by $t = \frac{L}{\beta c}$, $\beta = \frac{p}{\sqrt{p^2+M^2}}$, where c is the velocity of light, M is the mass of the charged particle, β is the flight velocity of the charged particle, L and p are the flight path and the momentum of the charged particle gives by the MDC measurements, respectively. The TOF information is used to calculate the mass of the charged particle:

$$\beta = \frac{L}{c \times t_{mea}}, M^2 = p^2 \times \frac{1-\beta^2}{\beta^2}, \tag{3.3}$$

where t_{mea} is the measured time. Obtained result from MC for a typical mass-squared distribution, M^2 , calculated by Eq. (3.3) is drawn for pions in Figure Figure 3.6. The TOF detector allows 3σ K/π separation for particles with momenta of up to 0.9 GeV/c.

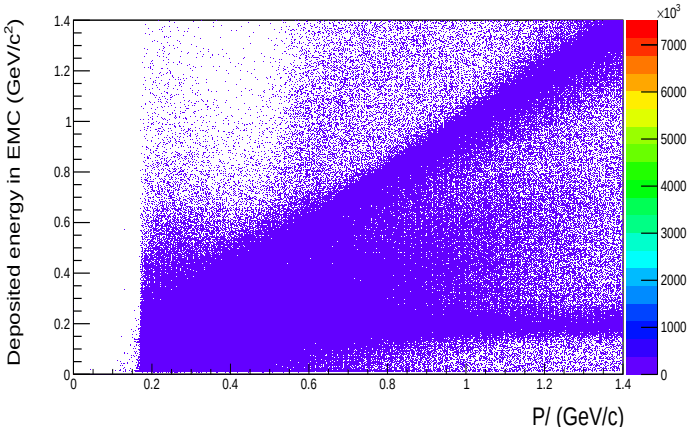

Figure 3.7: The energy deposition of a charged track, obtained from the EMC, versus its momentum reconstruction extracted from the MDC information obtained from 2009 ψ' data sample. We have selected events that contained at least one photon and one charged particle in the final-state.

3.3.4 Electromagnetic Calorimeter (EMC)

At the outside of the TOF, the BESIII EMC is used to measure the energy and scattering angles of electrons, positrons and photons, as well as to contribute to the level 1 trigger. The energy and angular measurements of photons are used in the reconstruction of π^0 and other neutral hadrons which are reconstructed from their decays into photons. The EMC provides an energy measurement for electrons and photons within the range of 20 MeV to 2 GeV. The energy and spatial resolutions in barrel (endcap) are 2.5% (5%) and 0.6 cm (0.9 cm) at 1 GeV, respectively. The angular coverage of the barrel EMC is $|\cos\theta| < 0.82$ whereas the end-cap covers the region $0.83 < |\cos\theta| < 0.93$.

The calorimeter is composed of one barrel and two end-cap sections, covering 93% of 4π. There are a total of 44 rings of crystals along the z direction in the barrel, each with 120 crystals, and 6 layers in the end-cap, with different numbers of crystals in each layer. The entire calorimeter has 6272 CsI(Tl) crystals with a total weight of about 24 tons.

The deposition of energy in the EMC is used to separate minimum-ionizing electrons and positrons from other (heavier) charged particles. Most of the heavier particles, such as muons and pions, are not subject to this form of energy loss and so they can be distinguished from electrons based on their energy loss in the EMC. The electrons

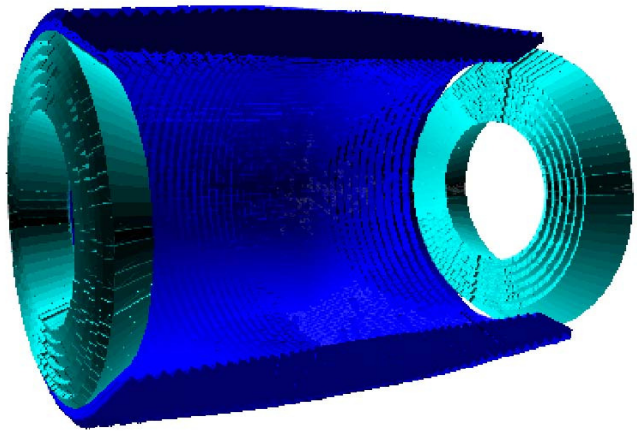

Figure 3.8: The BESIII Electromagnetic Calorimeter.

and positrons are moving at relativistic speeds and thus are minimum-ionizing particles that deposit a constant amount of energy in the EMC, independent on their momenta. Due to the small mass of the electron, bremsstrahlung radiation causes electrons to lose energy proportional to their momenta. In Figure 3.7 we show the energy deposition of a charged track, obtained from the EMC, versus its momentum reconstruction extracted from the MDC information. The data have been obtained from the 2009 data sample in which the $\psi^{'}$ decays were studied. We have selected events that were with at least one photon and one charged particle in the final-state. The horizontal band corresponds to the pions and muons and the diagonal band corresponds to electrons. This plot confirms that the EMC information provides good e/π separation for particles with momenta greater than 650 MeV/c.

The EMC is designed to have an energy resolution of about $2.3\%/\sqrt{\mathrm{E(GeV)}} \oplus 1\%$. The energy resolution versus photon energy simulated for the single photon energies ranging from 100 MeV to 1 GeV for all photons that were generated in the simulated process $\psi^{'} \to \gamma\eta_c$, $\eta_c \to$ anything is shown in Figure 3.8. For each photon candidate, we take the difference between the true photon energy and the reconstructed one. The distributions we obtain, after taking many events and binning in several energy intervals, have been used to estimate the resolution. Each distribution is then fitted with an asymmetric gaussian function and the resolution is defined as σ/E_γ, where σ is obtained from the asymmetric gaussian. The best energy resolution is 3.5% according to Figure 3.9. The resolution varies from 1.8-3.5% for the photon energies between 0.1-0.8 GeV.

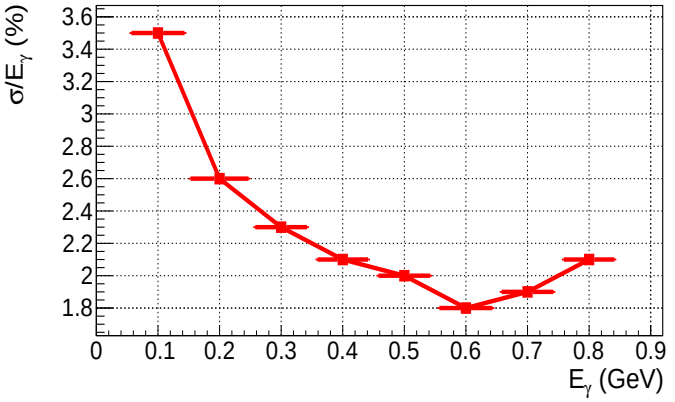

Figure 3.9: Resolution of photons as a function of photon energy for the process, $\psi\prime \to \gamma\eta_c, \eta_c \to$ anything. The result is obtained from a MC simulation. For more details see text.

3.3.5 Muon identifier (MU)

The final component of the detector is the MUon identifier (MU) which is composed of nine layers of Resistive Plate Chambers (RPC) in the barrel and eight layers in the end-cap to form a muon identifier. The spatial resolution is about 16.6 mm. The purpose of the MU is to distinguish muons from pions and other hadrons. Since muons only interact weakly, they can penetrate deeper into the MU than charged hadrons which are subject to strong interactions. Electrons and positrons will not reach the muon counter since these particles have already lost their energy in the EMC. On the other hand, most of the hadrons pass through the material of the calorimeter and magnet coil, and are absorbed somewhere in the iron yoke. Because of the bending of the muon path due to the magnetic field, muon identification in the muon chamber only becomes useful for muons with momenta greater than 0.4 GeV/c. Figure 3.10 shows the performance of the current muon identifier from simulated single muon and pion events in the momentum range between 0.5 and 1.9 GeV/c. In general, the MU detector is able to reject pions to a level of $\sim 4\%$ while keeping 90% of the muons. The MU information has not been used for particle identification for the work presented in this thesis.

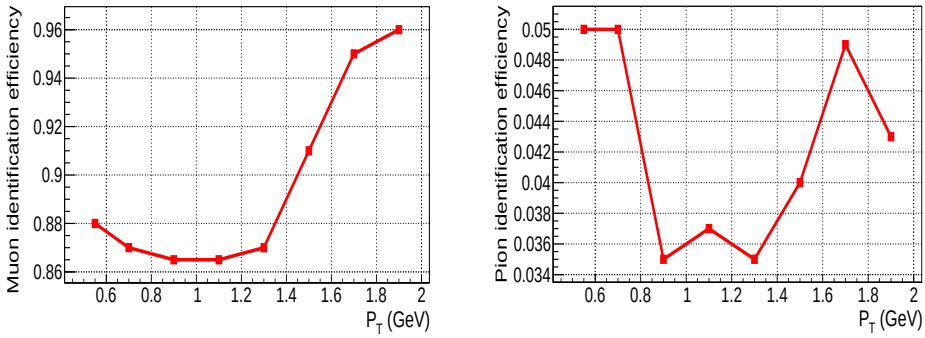

Figure 3.10: Left (right): Muon (pion) identification efficiency as a function of the transverse momentum [58].

3.3.6 Luminosity determination

The luminosity will be an input to many precision measurements, including the τ mass measurement, R-values, $J/\psi, \psi^{'}, \psi^{''}$ total widths, cross sections etc.. For these quantities, the luminosity error will directly translate into errors on their measured values. Thus, a precision measurement of the luminosity is a very important aspect of the BESIII physics program.

The cross section σ determines the probability of a physical process at each energy point, whereas the production rate for a process of interest is given by $dN/dt = \mathcal{L} \cdot \sigma$ with $\mathcal{L}$ is the luminosity of the accelerator which depends on properties of the beam. It is given by:

$$\mathcal{L} = \frac{N_1 N_2 f}{4\pi\sigma_x\sigma_y}, \tag{3.4}$$

where N_1 , N_2 are the numbers of particles (electrons and positrons) per bunch, σ_x, σ_y are the spatial dimensions of a bunch which is basically the cross section area of the overlap of both bunches and f is the frequency of bunch collisions of the accelerator. The luminosity is determined by measuring the yield of the three main QED processes $e^+e^- \to (\gamma)e^+e^-$, $(\gamma)\mu^+\mu^-$ and $(\gamma)\gamma\gamma$ using information from all subdetectors of BESIII. The cross sections of these processes are very large and accurately known. For the luminosity determination, the Bhabha scattering process $e^+e^- \to e^+e^-$ is adopted since it has the largest production cross section. With this process, we can get a higher precision for the luminosity measurement. By measuring the rates of QED processes and correcting for spectrometer acceptances and efficiencies, the luminosity can be accurately determined. The integrated luminosity is given by $\mathcal{L}_{int} = \int \mathcal{L}dt$ and

quantities the amount of data taken during a specific time during the experiments.

3.3.7 Number of $\psi^{'}$ events

The decay of $\psi^{'} \rightarrow$ inclusive hadrons was used to extract the number of $\psi^{'}$ events which is the crucial parameter for measuring the branching fraction of subsequent decays. The branching fraction of $\psi^{'} \rightarrow$ inclusive hadrons is very well-known, $(97.85 \pm 0.13)\%$ [48]. To estimate the continuum background, four τ-scan energy points above the τ pair mass region ranging from 3.540 to 3.560 GeV are used due to the small energy difference between the $\psi^{'}$ peak and the τ pair mass threshold. The number of $\psi^{'}$ events is determined by [116]:

$$N_{\psi'} = \frac{N^{obs.}_{peak} - f \cdot N^{obs.}_{off-resonance}}{\epsilon}, \tag{3.5}$$

where $N^{obs.}_{peak}$ is the observed number of hadronic events at the $\psi^{'}$ peak, $N^{obs.}_{off-resonance}$ is the observed number of hadronic events at τ scan with the average of $E_{cm} = 3.572$ GeV, with the same selection criteria as $\psi^{'}$ peak events, ϵ is the selection efficiency obtained from inclusive $\psi^{'}$ MC sample and f is the scaling factor to account for the energy dependence of the cross section:

$$f = \frac{\mathcal{L}_{\psi'}}{\mathcal{L}_{3.65}} \cdot \frac{3.65^2}{3.686^2} = 3.677, \tag{3.6}$$

where $\mathcal{L}_{\psi'}$ is the luminosity for $\psi^{'}$ data and $\mathcal{L}_{3.65}$ is the luminosity for τ scan data. The total number of the $\psi^{'}$ events from 2009 is $(106.8 \pm 0.70) \times 10^6$ and the total number of $\psi^{'}$ from 2012 is $(341.1 \pm 0.63) \times 10^6$ corresponding to an integrated luminosity of 156.4 pb^{-1} [116].

3.4 Trigger

The trigger is the fast real-time event selection and hardware control system for BESIII. The purpose of a trigger system is to select events of interest from enormous backgrounds and to suppress backgrounds to a level that the DAQ system can handle. The BESIII DAQ is designed for a maximum throughput of 3000 events per second. The trigger system reduces the rate of various backgrounds and Bhabha events down to 1500 Hz while keeping a high efficiency for J/ψ and $\psi^{'}$ decays.

3.4.1 Backgrounds and rates

The BESIII detector deploys a two-tier trigger system to filter out background while maintaining a high efficiency for physics events, illustrated in the block diagram in Figure 3.11. The main background is from beam-related sources like beam-gas and beam-wall interactions. Such backgrounds occur at a rate about 13 MHz. Collimators and masks are used to keep lost electrons from interacting with the detector, but the trigger must help to filter these events further. The other source of background that the triggers suppresses come from cosmic rays which pass through the detector. The rate coming cosmic ray is about 1.5 kHz. The trigger system must suppress these backgrounds to a level that does not overwhelm the expected rate of physics events, which is about 2 kHz at the J/ψ peak and 600 Hz at the ψ' peak when running at the peak luminosity of 10^{33} cm^{-2} s^{-1}. The Bhabha process ($e^+e^- \rightarrow e^+e^-$) occurs at a rate of 800 Hz within the detector acceptance, and pre-scaled events from this process are recorded for calibration and luminosity measurements.

3.4.2 Trigger system

The Level 1 (L1) trigger decision is made with inputs from the MDC, TOF, and EMC sub-detectors. This trigger is read out every clock cycle (24 ns) at a rate of 41.65 MHz. There is a 6.4 μs latency between the trigger signal and the event occurrence, mainly due to the slow signal from the EMC, which has a 1 μs peaking and 3 μs decay time.

The MDC defines short and long tracks. A minimum transverse-momentum cut is applied to these tracks to ensure that tracks with sufficient momentum have originated from the IP and reach the appropriate outermost superlayer while traveling in a magnetic field of 1 Tesla. This cut is 90 MeV/c for short tracks and 120 MeV/c for long tracks. The number of short and long tracks, along with information on back-to-back tracks, is passed to the L1 trigger to be used in conjunction with the TOF and EMC information.

The TOF passes on the number of hits in the barrel and end-cap regions, as well as information on back-to-back hits in the barrel and end-cap TOF. The TOF must have hits within a range of 9 counters on the opposite sides of the detector to be considered back-to-back.

Clustering is the first step in determining the L1 trigger information from the EMC. Clustering refers to combining the energy of adjacent crystals around a local maximum-energy deposit in a crystal. The number of isolated clusters is sent on to the L1 trigger along with back-to-back information for the barrel and end-cap EMC. Combining the information from these three sub-detectors enables the trigger to reduce the rate of

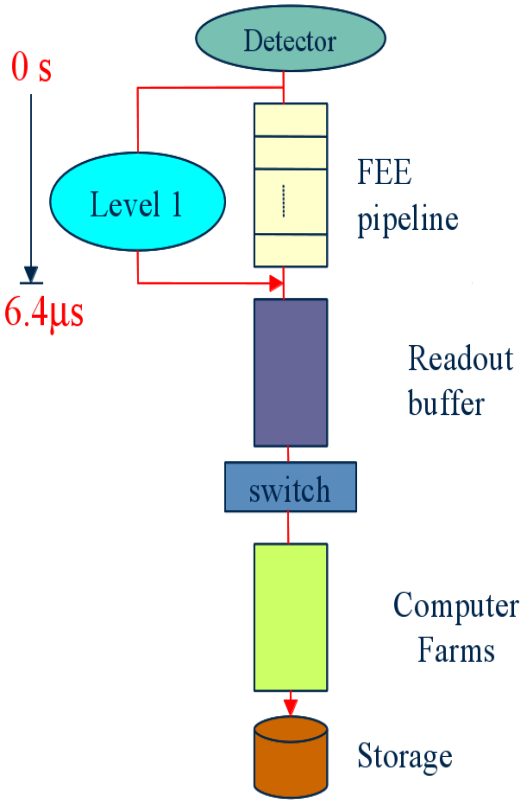

Figure 3.11: Schematic overview of the BESIII trigger system.

Process	Level 1 Trigger Efficiency (%)
$J/\psi \rightarrow$ anything	97.7
$\psi^{'} \rightarrow$ anything	99.5
$e^+e^- \rightarrow e^+e^-$	100
$e^+e^- \rightarrow e^+e^- \gamma$	100
Beam-related backgrounds	4.6×10^{-3}
Cosmic-ray backgrounds	9.4

Table 3.2: The percent of events passing the level L1 trigger.

cosmic-ray background to about 200 Hz and the beam-related background to 1.84 kHz. The maximum L1 trigger rate is 4 kHz. The L1 trigger efficiencies are summarized in table 3.2 for various processes which confirms that the efficiency to keep the good events relevant to our interested channel, $\psi^{'} \rightarrow$ anything, is around 99%.

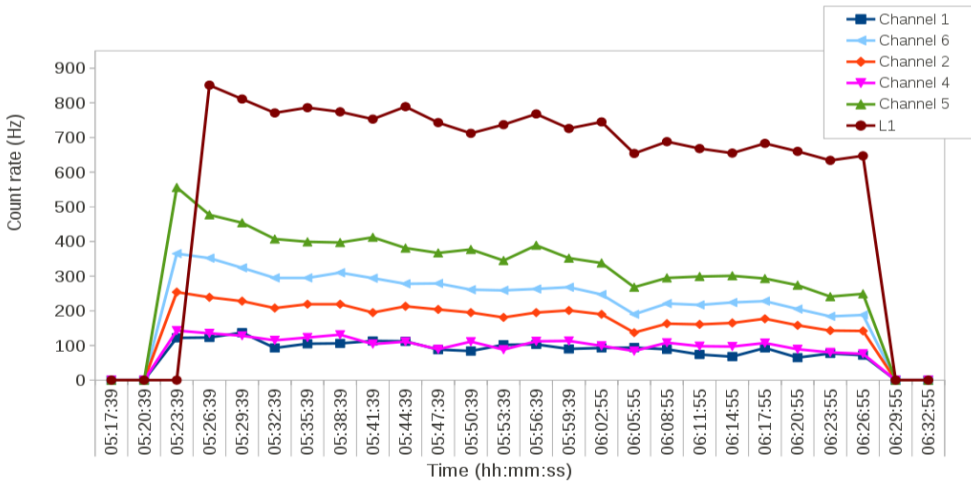

Figure 3.12: Count rate in different trigger channels for run number 26642 [100].

Once a level 1 trigger is received, the electronics from all of the sub-detectors are read out and the event is assembled in an online computer farm. This farm is responsible for the somewhat confusingly-named level 3 (L3) software trigger. The background reduction for the L3 trigger is fairly modest, taking a background rate of about 2 kHz and reducing it by half. Combined with a 2 kHz signal rate at the J/ψ peak, the level 3 trigger writes out events at a rate of about 3 kHz. This corresponds to data being written to mass storage at a speed of 40 MB/s.

3.4.3 ψ' data from 2009/2012

The trigger settings for ψ' data taking are summarized in table 3.2. Channel 0 is designated for end-cap Bhabha events, channels 1 to 5 for events with charged particles in the barrel region and channel 11 for all-neutral events. An MDC super-layer consists of four neighboring wires. If any of the trigger channels listed in the table were active, the event would be read out. Trigger efficiencies for various channels are studied in detail in [99]. The count rates as a function of time for different trigger channels for the ψ' data sample for one beam spill corresponding to run number 26642 are shown in Figure 3.12 [100]. From the figure one can see that the typical lifetime of the beam is about 250 minutes, the typical data-taking time per run is about 1 hour and the typical count rate for the L1 trigger is about 750 Hz. The condition for the 2009 and 2012 data sets are similar, except for channel 3 which is not used in the 2012 data set.

$\psi^{'}$ data from 2009	
Trigger channel	Trigger conditions
channel 0	Number of short tracks back-to-back of MDC ≥ 1, Number of end-cap TOF hits ≥ 1, Number of end-cap clusters ≥ 1
channel 1	Number of long tracks in MDC ≥ 2, Number of barrel TOF hits ≥ 2, Number of barrel clusters ≥ 1
channel 2	Number of long tracks in MDC ≥ 2, Number of barrel TOF hits ≥ 2
channel 3	Long tracks back-to-back, Number of barrel TOF hits ≥ 1
channel 4	Number of long tracks back-to-back in MDC ≥ 1, Number of barrel ToF hits ≥ 1
channel 5	Number of long tracks in MDC ≥ 1, Number of barrel ToF hits ≥ 1, Total energy deposited in EMC above a lower threshold
channel 6	Number of barrel clusters in EMC ≥ 2, total energy deposited in EMC is above a medium threshold
channel 9	Random trigger at 60 Hz
channel 11	Number of clusters in EMC ≥ 2, Total energy deposited in EMC above a medium threshold

Table 3.3: Trigger settings for the $\psi^{'}$ data from 2009. Channel 0 is designated for end-cap Bhabha events, channels 1 through 5 for events with charged particles in the barrel region, channel 6 for events with neutral particles, channel 9 for random trigger and channel 11 for all-neutral events.

3.4.4 DAQ system and event filter

The BESIII DAQ is designed to read out data from the front-end electronics system (FEE) and record valid data on storage devices, using a VME architecture and an online computer farm. After L1 triggers are received, the DAQ system transfers all sub-detector data to the online computer farm. The computer farm carries out the event reconstruction, event filtering and background suppression, and controls and monitors the DAQ operation.

Chapter 4

Analysis tools

The BESIII analysis software is used for data analysis of this work. For the data analysis we made use of the common software framework developed and maintained by the BESIII collaboration. This framework provides a rich library of software tools that can be used to process the data, including high-level algorithms dedicated for physics studies, such as track and (secondary) vertex fitting, particle identification (PID) and kinematic fitting tools. These tools are used to reconstruct the vertex and four momentum of particle candidates of the channel of interest, optimize the corresponding resolutions, and suppress background events.

This chapter provides information about the tools and methods which are used to reconstruct the final-state particles containing charged tracks and photons related to the two analysis channels which are reported in this thesis:

- $\psi^{'} \to \gamma\eta_c, \quad \eta_c \to$ anything
- $\psi^{'} \to \pi^{\pm}\pi^{\mp}J/\psi, \quad J/\psi \to \gamma\eta_c, \quad \eta_c \to K^{\circ}_{S}K^{\pm}\pi^{\mp}$

4.1 BESIII offline software

The detector description, calibration, data reconstruction, Monte Carlo simulation and reconstruction, and analysis tools are implemented within the BESIII Offline Software System (BOSS) [101]. BOSS is developed using the C++ language and object-oriented techniques on the operation system of Scientific Linux CERN (SLC).

The BOSS framework has been developed based on Gaudi [101], which provides standard interfaces for the common software components necessary for data processing and physics analysis. The framework employs Gaudi event data service as the data

manager. Three types of persistent event data have been defined in the BOSS system: raw data, reconstructed data and Data-Summary-Tape (DST) data. Raw data are data collected from the detector without any processing. It contains the QED processes, hadronic processes (including continuum and resonance states) and beam-associated backgrounds. The raw data after calibration is called reconstructed data. Then, after reconstruction, the results are stored as DST data. Both reconstructed data and DST data are in ROOT format for easy management and usage. ROOT is an object-oriented framework for performing physics analysis [117]. The BOSS software is managed with the Configuration Management Tool (CMT) [102], which handles the dependencies between software packages, as well as creating the executables and the libraries from the source code and header files.

4.1.1 Simulation

The BESIII detector simulation, based on the GEANT4 package [103], consists of four parts:

- Event generators:
  KKMC is used to generate charmonium states with the inclusion of ISR effects and the beam energy spread and the BesEvtGen [104] (based on EvtGen [105]) is used for τ-charm physics;
- Detector description:
  A unique description of the detector geometry and materials, used by both simulation and reconstruction packages, has been developed on the basis of XML [106];
- Particle tracking:
  Particle tracking and the interactions with the detector materials are all handled by GEANT4;
- Detector response:
  Detector responses are modeled by the so-called "digitization code", which takes into account various hardware aspects, including readout electronics, as well as the realistic situations such as noise, dead channels, etc..

4.1.2 Reconstruction

Data reconstruction is the central task for the offline data processing. The BOSS software takes as input the information obtained from the readout of each sub-detector.

These data are combined with the interaction on detector material and geometry descriptions saved in Geometry Design Markup Language (GDML) files [107].

4.1.2.1 MDC reconstruction

A track-finding algorithm and a Kalman-filter-based track-fitting algorithm are used to determine the momentum of charged particles based on the information from the MDC (see Section 3.3). The reconstruction begins with finding track segments from the raw hits according to pre-calculated patterns. A least-squares method is used to fit axial segments to circles. Once a circle has been identified from axial segments, stereo hits are added and the axial and stereo hits are fitted iteratively to the helix shape that represents the path of a charged particle through a uniform magnetic field. Finally, after collecting additional hits that might possibly belong to the track, a track refitting procedure based on the Kalman-filter technique is performed [58]. For charged particles with transverse momentum larger than 150 MeV, the reconstruction efficiency is about 98%, even in high background environments [58]. The reconstructed tracks in the MDC are used to determine the charge, momentum, and position of the particles. The *dE/dx* information from the hits along the track is used in conjunction with the TOF information to provide PID.

4.1.2.2 TOF reconstruction

For the TOF (see Section 3.3.3) reconstruction, first of all, MDC tracks are extrapolated to the TOF and matched with a particular TOF module. The TOF reconstruction algorithm calculates precisely the time that a charged particle needs to travel from the IP to the TOF itself. Using the information provided from the MDC about the particle's momentum and flight path, the TOF time measurements are used to discriminate between the charged particle hypotheses. Energy deposited in the TOF is also added back into the energy from the EMC for showers that started in the TOF.

4.1.2.3 EMC reconstruction

The data reconstruction in the EMC (see Section 3.3.4) consists of five concatenated steps:

- Hit position:

When a photon or an electron (positron) hits the EMC, it interacts with CsI(Tl) crystals. The photon transforms to a e^+e^- pair through gamma conversion, and the e^+ or e^- emits photons through bremsstrahlung. These interactions continue alternatively and form an electromagnetic shower. The shower develops laterally and longitudinally, depositing energy in several connected crystals. The reconstruction algorithm searches for these adjacent crystals, adds their registered energy together, and calculates the hit position.

- Clustering:

  At BESIII, the definition of a cluster is a contiguous group of crystals with a deposited energy above a certain threshold. In essence, the crystal algorithm searches recursively for firing adjacent crystals and adds these into a list. This process is continued until no more neighboring firing crystals are found. All the crystals in the list form a cluster. The same procedure is implemented for firing crystals not in the list, until no more clusters are found.

- Cluster splitting:

  A cluster can be the result of energies deposited by one or more particles, corresponding to one or more showers. Each shower is recognized by a seed, which is the local maximum of energy deposition among its cluster members. If a cluster contains only one seed, only one shower, i.e., one particle is identified. If more seeds are found, for example, in a cluster caused by two photons from the decay of high-momentum π° meson, the cluster can be split into several showers.

- Shower energy:

  The energy of the photon is one of the most important quantities for further physics analysis. The success of our physics study depends strongly on the energy resolution that can be obtained for registered photons. Although one might expect that the best energy resolution is obtained by summing up all the deposited energies of all crystals in a shower, the electronics noise and backgrounds may be included in the sum, hence deteriorating the resolution. A common practice to optimize the resolution is to sum up the deposited energies of a cluster of 3×3 or 5×5 crystals around the seed. The corresponding sum energies are referred to

as E3 × 3 or E5 × 5, which contain 9 and 25 crystals, respectively. In the current setup, E5 × 5 is used to define the shower energy for the BESIII EMC [127].

The energy loss in the TOF counters can be reconstructed, matched and added to the deposited energy in the EMC shower. This procedure improves the energy resolution significantly as described in reference [128]. For the energy calibration, π° or radiative photon samples are selected from data [129].

- Shower position:

There are many different methods to obtain the shower position. The simplest and fastest one is by calculating the energy-weighted mean, as written in the following:

$$\overrightarrow{x_c} = \frac{\Sigma_i W_i(E_i)\overrightarrow{x_i}}{\Sigma_i W_i(E_i)}. \tag{4.1}$$

A center-of-gravity (CG) method is used to calculate the impact coordinate, $\overrightarrow{x_c}$, of the showering particles on the front face of the EMC [131]. The weight, $W_i(E_i)$, is a function of the deposited energy in the cluster, and $\overrightarrow{x_i}$ the center of i^{th} crystal in the cluster. The sum includes the information of all crystals in a cluster. In reference [130] several weighting functions are evaluated. The simplified version of this method is a linear weighting function, which is defined as:

$$W_i^{linear}(E_i) = E_i, \tag{4.2}$$

and the second method is a logarithmic weighting function, which is defined as

$$W_i^{log}(E_i) = \max\{0, a_0 + \ln(E_i) - \ln(E_{total})\}, \tag{4.3}$$

where E_{total} is the sum of the total energy deposited in the crystals and $a_0 = 0.4$ is the cutoff parameter which guarantees that the logarithm gets a positive argument and removes crystals with a very low-energy. Since the photon energy, related to the analysis reported in this thesis, is between 100 and 700 MeV, the second method is used, which can reduce the weight of the most energetic crystals and enhance the low-energy ones.

Both methods need corrections because of the complexity of the EMC geometry. Bhabha events are used for this purpose. The hit position determined from a track

extrapolation from the MDC information is compared to the weighted shower position and thereby used to obtain a correction factor.

4.1.2.4 MU reconstruction

The reconstruction in the MU is fairly straightforward and algorithm-wise easy, and is mainly used to see how far a particle penetrates from the IP in order to separate muons from other charged particles. The MU information is not used in the analysis presented in this thesis, and it will, therefore, not be discussed any further.

4.1.3 Calibration

The calibration software, which is based on GLAST's scheme, consists of a calibration framework and calibration algorithms [108]. The calibration constants for each sub-detector are produced by the associated calibration algorithm, and then stored in a ROOT file and a database along with other information such as the run information, trigger condition, software and hardware version number, etc..
The calibration algorithm contains time correction, effective velocity and attenuation calibration [58]. The calibration is data-driven and can be done using well-understood control channels with high statistics.

- MDC calibration:
  The MDC has been calibrated using $J/\psi \to \mu^+\mu^-$ events for both position and dE/dx measurements. Since the production cross section at the J/ψ peak is huge, sufficient statistics can be obtained in a short run period.

- TOF calibration:
  The TOF calibration has been performed using J/ψ decays to leptons, both for timing and energy.

- EMC calibration:
  The EMC high-energy response has been calibrated with Bhabha electrons at energies of 1.55 GeV or more and the low-energy response with $\pi^\circ \to \gamma\gamma$ decays. Each crystal has been recalibrated periodically, and monitored frequently by an LED light pulser. Corrections due to temperature variations are applied.

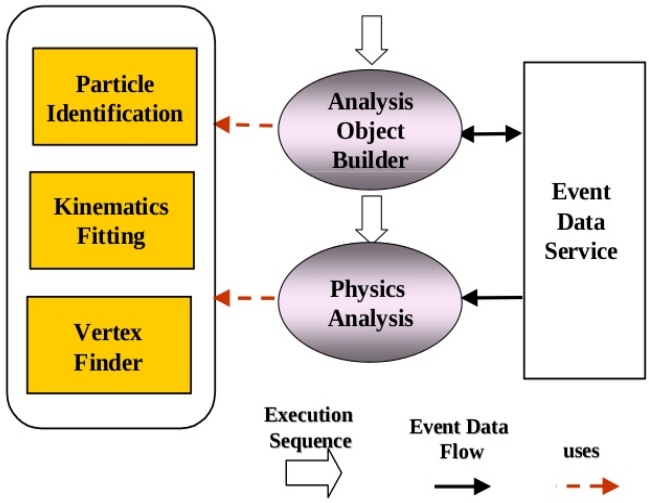

Figure 4.1: The structure of the analysis software [108].

4.1.4 Analysis tools

The block diagram of the analysis software is shown in Figure 4.1. The Analysis Object Builder (AOB) will fetch the reconstruction results from the Transient Data Store (TDS) through the event data service, then build data objects that are more suitable for physics analysis and put them back into TDS. In this process, the BESIII physics tools are used, including vertex finder and PID. In BESIII, PID will combine TOF, dE/dx measurements, energy deposits in EMC and MU information to provide data for physics studies.

4.2 Monte Carlo generators

High quality Monte Carlo (MC) simulations will be essential for minimizing experimental systematic uncertainties. They are used to determine detection efficiencies, to model backgrounds and to determine analysis strategies. Thus, the MC generators must simulate the underlying processes being studied as precisely as possible. In this section, we give an overview of the BESIII generator framework and we give a brief introduction to the BESIII event generators, such as KKMC, BesEvtGen, various QED generators and some inclusive generators which are used for further analysis.

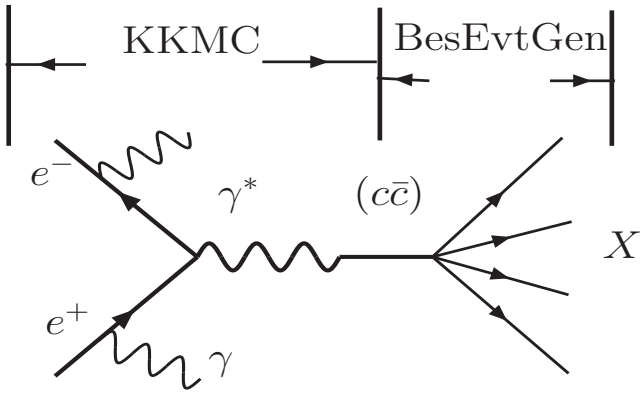

Figure 4.2: BESIII generator framework [58].

4.2.1 Generator framework

To generate charmonium decays, KKMC and BesEvtGen [118] are used as the default generator framework. In e^+e^- annihilation, the incoming positrons and electrons can radiate real photons via ISR before they annihilate into a virtual photon. Taking into account these radiative processes is crucial in e^+e^- annihilation experiments, especially for measurements performed near a resonance or near a production threshold. To obtain meaningful results, generators for e^+e^- collision must take ISR into account. The KKMC generator is used to simulate $c\bar{c}$ production via e^+e^- annihilation. Subsequently, charmonium meson decays ($c\bar{c} \to X$) are generated with BesEvtGen (see Figure 4.2).

KKMC: The KKMC generator, originally developed for the LEP and SLC colliders, is used to model SM electroweak interactions and it generates processes of the form $e^+e^- \to f\overline{f} + n\gamma$, where $f = \mu, \tau, u, d, s, c, b$ at center-of-mass energies from the $\tau^+\tau^-$ threshold up to 1 TeV. KKMC takes into account second-order sub-leading corrections. ISR and interferences between initial-state and final-state radiation are modelled by KKMC. In our case, KKMC is used to generate J/ψ and $\psi^{'}$ with the inclusion of ISR effects and the beam-energy spread.

BesEvtGen: The BesEvtGen generator is based on EvtGen, which was originally developed for the CLEO and BaBar experiment. Over 30 models for exclusive decays are available in BesEvtGen, in addition to the ability to easily incorporate user-created

decay models. The amplitudes for these models are constructed using the helicity amplitude method, and constrained by imposing parity conservation. FSR effects can be included at the BesEvtGen level by the PHOTOS model [108]. The Lundcharm and PYTHIA models are used to generate unknown decays of charmonium resonances [119].

4.2.1.1 QED generator

Babayaga [110] is a QED generator to generate $e^+e^- \to e^+e^-$, $\mu^+\mu^-$ and $\gamma\gamma$. It has a high-precision QED calculation of the Bahbha process. The theoretical accuracy of Babayaga is quoted as 0.1% [111] and is used to determine efficiencies and acceptances for measuring the integrated luminosity of BESIII data samples.

4.2.1.2 Inclusive MC generator

The Lundcharm model was especially adjusted by BESII for simulating J/ψ and $\psi^{'}$ inclusive decays. C- and G-parity constraints were imposed and comparisons with experimental data were performed [112]. As a result, BESIII officially decided to use this modified Lundcharm model to generate J/ψ and $\psi^{'}$ inclusive decays in the BesEvtGen framework. An advantage of generating inclusive MC events with Lundcharm running in the EvtGen framework is that the decay widths in the Lundcharm model can be controlled by the user. Thus, branching fractions and models for known decays can be specified in the EvtGen decay dictionary, while unknown decays are generated with the Lundcharm model.

4.2.1.3 Exclusive MC generators

For exclusive MC simulations, the generator is based on the amplitude information developed in the EvtGen framework. The models cover hadronic decays, radiative decays and decays for investigating some physical quantities in charmonium physics.

The models that are used for the analyses presented in this thesis are as follows [113]:

- PHSP:
  This refers to a pure phase-space model that is used to generate channels such as $\eta_c \to K^{\circ}_S K\pi$, $\pi^{\circ} \to \gamma\gamma$, $K^{\circ}_S \to \pi^+\pi^-$.

- JPE:
  This model is constructed for vector decays into a photon plus a pseudoscalar meson. In our case, it is used for the decay $J/\psi \to \gamma\eta_c$ and $\psi^{'} \to \gamma\eta_c$ to give the corresponding angular distribution.

- JPIPI:
  This model is constructed for the decay $\psi^{'} \to J/\psi\pi\pi$. In this model, the amplitude is constructed by the chiral effective Lagrangian:

$$A_\Lambda \propto [g(m^2_{\pi\pi} - 2m^2_\pi) + 2g_1 E_{\pi^+} E_{\pi^-}]\epsilon^*_{\psi'}(M) \cdot \epsilon_{\psi'}(\lambda), \tag{4.4}$$

  and the parameters (g, g_1, and $\epsilon^*_{\psi'}$) are taken from a fit to the experimental mass spectrum of two pions [114].

- P2GC0,1,2:
  This model is constructed for the decay $\psi^{'} \to \gamma\chi_{cJ=0,1,2}$. The amplitude is constructed in the helicity amplitude given by:

$$M \propto D_{m,\lambda}(\theta, \phi)A_\lambda, \tag{4.5}$$

  where the m and the λ are the helicity value of $\psi^{'}$ and γ, respectively, A_λ is the decay amplitude and $D_{m,\lambda}$ is the D function [133]. For consideration of CP invariance, the helicity amplitudes satisfy the relation $A_{-\lambda} = A_\lambda$. The angular distribution of the outgoing photon takes the following form:

$$\frac{dM^2}{dcos\theta} \propto (1 + \alpha\cos^2\theta), \tag{4.6}$$

  where α depends on the total angular momentum $J = 0, 1, 2$.

- MassH2:
  This model is constructed to generate events using a Dalitz plot as input, given in root format. The x-axis corresponds to the $m^2_{DP[i],DP[j]}$, and y-axis to $m^2_{DP[i],DP[k]}$ where DP_i, DP_j and DP_k are the daughter particles specified by users.

- S2GV:
  This model is constructed for scalar decays into a photon plus a vector meson. For example, the decay $\chi_{c0} \to \gamma J/\psi$ is modeled by S2GV.

- VLL:
  VLL is one of the available decay models in EvtGen which is suitable for charmonium decays, where V and L denote vector and lepton, respectively. In our case, this model is used for the decay $J/\psi \to e^+e^-$.

4.3 Track reconstruction

In particle physics, the tracking is the act of measuring the direction and magnitude of the momenta of charged particles. The task of track reconstruction is traditionally divided into two different subtasks: track finding and track fitting. Track finding is a pattern recognition or classification problem and aims at dividing the set of measurements in a tracking detector into subsets, each subset containing measurements believed to originate from the same particle. These subsets are called track candidates. The track fit takes the set of measurements in a track candidate as a starting point. The goal is to estimate as accurately as possible a set of parameters describing the position of the particle somewhere in the tracking detector, often at a reference surface close to the particle beam. The track fit is also used to decide whether the track candidate hypothesis is valid.

The MDC tracking algorithm starts with the formation of track segments from hits using pre-calculated patterns. It then links the found axial segments to circular tracks and applies a circular fit using the least-square method. Stereo segments are subsequently added to track candidates followed by an iterative helix fit. Finally, after collecting additional hits that might possibly belong to the track, a track refitting procedure based on the Kalman-filter technique is performed [132]. This method yields more accurate track parameters and an error matrix. This method updates fitting results in each step, taking into account material effects and magnetic field distortions. The corrections due to energy loss and non-uniformity of the magnetic field for the track reconstruction are taken care of by a subsequent software package.

Particle tracking and their interactions with detector materials are handled by the GEANT4 package, while detector responses are modeled by the so-called digitization code, which takes into account detector components, including readout electronics, as well as the realistic situations such as noise, dead channels, etc.. A simulation of the trigger system is also implemented.

4.4 PID

After track reconstruction, we determine the type of charged particle by using particle identification (PID) methods. PID will play an essential role in most of the BESIII physics program to identify the neutral and charged tracks in the final-state. For example, in our case, we need to distinguish between kaon and pion tracks for the channel $\psi' \to \pi^{\pm}\pi^{\mp}J/\psi$, $J/\psi \to \gamma\eta_c$, $\eta_c \to K_S^{\circ}K\pi$, $K_S^{\circ} \to \pi^{\pm}\pi^{\mp}$. For this, we use PID.

4.4.1 Probability Density Functions (PDFs)

The response of a detector to each particle species is given by a probability density function (PDF). The PDF, written as $\mathcal{P}(x;p,H)$ describes the probability that a particle of species $H = e^{\pm}, \mu^{\pm}, \pi^{\pm}, K^{\pm}$, p, $\bar{p}$ leaves a signature x described by a vector of measurements (dE/dx, TOF, E/p, ...). $\mathcal{P}(x;p,H)dx$ is the probability for the detector to respond to a track of momentum p and type H with a measurement in the range $(x, x+dx)$ [58]. As with any PDF, the integral over all possible values is unity, $\int \mathcal{P}(x;p,H) = 1$. Note that the momentum is treated as part of the hypothesis for the PDF and, is therefore, placed to the right of the semicolon. The momentum measurements from the drift chamber are usually of sufficient precision that they can be fixed in the PDF calculation. In borderline cases when the precision is not quite sufficient, it is sometimes treated by assuming that the momentum is perfectly measured and by smearing the PDF. The vector x may describe a single measurement in one detector, several measurements in one detector, or several measurements in several detectors. The measurements may be correlated for a single hypothesis. In both reported cases in this thesis, the correlations will be reasonably small and the overall PDF is determined as a product of the PDFs for individual detectors.

4.4.2 Likelihood

In practise, we use the likelihood method to relate a track to a particle of species H. The likelihood that a track with measurement vector x is a particle of species H is denoted by $\mathcal{L}(H;p,x)$. The functional forms of PDFs and the corresponding likelihood function are the same [58]:

$$\mathcal{L}(H;p,x) \equiv \mathcal{P}(x;p,H). \tag{4.7}$$

The difference between $\mathcal{L}(H;p,x)$ and $\mathcal{P}(x;p,H)$ is subtle. The probability ($\mathcal{P}$) is a function of the measurable quantities x for a fixed hypothesis (p,H) whereas the likelihood ($\mathcal{L}$) is a function of particle type H for a fixed momentum p and the measured value x. Therefore, an observed track for which x has been measured has a likelihood for each particle type. Particle type hypotheses have been compared using the ratio of their likelihoods. For example, to distinguish between the K^+ and π^+ hypotheses for a track with measurements x_{obs} related to the channel of $\psi' \to \pi^{\pm}\pi^{\mp}J/\psi$, $J/\psi \to \gamma\eta_c$, $\eta_c \to K^{\circ}_S K^{\pm}\pi^{\mp}$, $K^{\circ}_S \to \pi^{\pm}\pi^{\mp}$, this quantity has been used:

$$\frac{\mathcal{L}(K^+; p_{obs}, x_{obs})}{\mathcal{L}(K^+; p_{obs}, x_{obs}) + \mathcal{L}(\pi^+; p_{obs}, x_{obs})}. \tag{4.8}$$

4.4.3 PID using TOF and *dE/dx*

The $K^{\pm}$ and $\pi^{\mp}$ candidates are identified with the information from both the energy loss in the main drift chamber (*dE/dx*) and the travel time of charged particles from the IP.
The TOF and *dE/dx* measurements for each charged track are combined to calculate $\chi^2_{PID}(i)$ values and the corresponding confidence levels $\mathcal{P}_{PID}(i)$ for the hypothesis that a track is of type i, e.g. a pion or kaon:

$$\chi^2_{PID}(i) = \left(\frac{(dE/dx)_{measured} - (dE/dx)_{expected}}{\sigma_{dE/dx}}\right)^2 + \left(\frac{(TOF)_{measured} - (TOF)_{expected}}{\sigma_{TOF}}\right)^2. \tag{4.9}$$

The expected values are calculated based on their reconstructed momenta and mass assumption. The $\chi^2_{PID}(i)$ is further used to obtain the probability of a track having a particle i assignment which we denote as $\mathcal{P}_i$. The values $\chi^2_{PID}(i)$ and $\mathcal{P}_i$ are calculated for each charged track for each particle hypothesis i. We label a track as $i = \pi(K)$ in the case $\mathcal{P}_\pi > \mathcal{P}_K$ ($\mathcal{P}_K > \mathcal{P}_\pi$) with the additional requirement $\mathcal{P}_i > 0.001$. This requirement is to guarantee there is no situation in which both of the $\mathcal{P}_{PID}(i)$ values are very close to zero which would make the relative-probability comparison meaningless. The PID using TOF and *dE/dx* measurements further improves by combining the $\chi^2_{TOF+dE/dx}(i)$ with the goodness-of-fit parameter, χ^2, of the kinematic fit as discussed in Section 4.5. This method was used in the analysis of $\psi' \to \gamma K^\circ_S K^{\pm}\pi^{\mp}\pi^{\pm}\pi^{\mp}$.

4.4.4 The E/p method

Most of the BESIII physics studies require high quality π/K, e/μ, e/π and e/K separation. *dE/dx* and TOF work very well for the identification of kaons and pions. $e/(\mu, K, \pi)$ identification can be done by the so-called E/p method with the ratio between the energy measured by the EMC and the momentum of the charged track reconstructed by the MDC. When an electron or positron passes through the calorimeter, one expects that these particles deposit their full energy in the calorimeter. Since the electron mass is negligible in the energy range of interest, we expect to find a ratio of

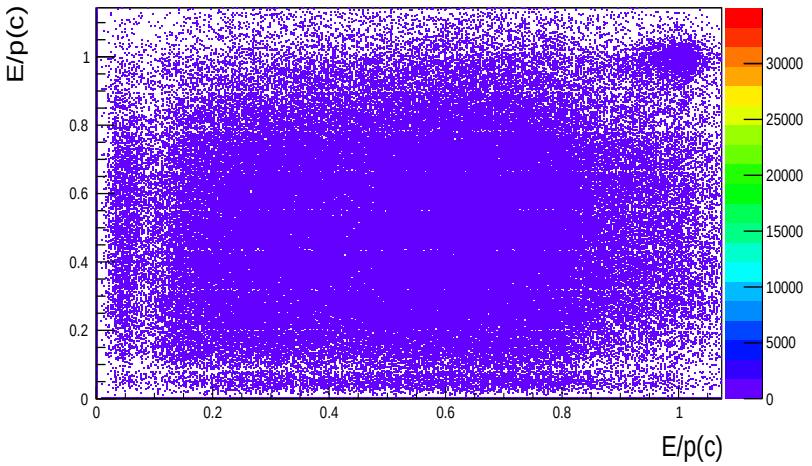

Figure 4.3: $E/p(c)$ distribution versus $E/p(c)$ for an analysis of the 2009 $\psi^{'}$ dataset. In this analysis, at least two charged tracks and at least one photon are required.

E/p close to unity. For muons, pions and kaons, this ratio will be significantly smaller than one since they will deposit only a fraction of their energy in the EMC. For a large part this is due to their heavier masses compared to that of the electrons or positrons. Figure 4.3 shows E/p versus E/p for charged tracks in an analysis of the $\psi^{'}$ dataset. In this analysis, at least two charged tracks and at least one photon are required as signal selection criteria. The blob around $E/p = 1$ corresponds to a coincidence between an electron and positron and the smaller values of E/p corresponds to μ, K, π which demonstrate that the E/p method works very well for separating the electrons or positrons from other charged tracks.

4.5 Kinematic fitting

The energy E and the angles θ and ϕ of the final-state particles are measured in the detector with finite resolution. In general, these quantities will not satisfy energy-momentum conservation exactly due to experimental resolutions. Kinematic fitting is a mathematical procedure in which one uses the physical laws governing a particle interaction or decay to improve the measurements describing the process. For example, consider the decay chains, $\psi^{'} \to \gamma\eta_c$, where η_c decays to $K^{\circ}_S K\pi\pi\pi$ and K°_S decays to $\pi^+\pi^-$. There are several constraints that can be applied:

• Energy and momentum are conserved (4 constraints, also known as 4C fit);
• The $\pi^+\pi^-$ pair from K°_S decay must come from a common space point;
• The momentum vector of the $\pi^+\pi^-$ pair must be aligned with the position vector of the decay vertex relative to the interaction point;
• Mass constraints of $M_{\pi^\pm\pi^\mp}$ related to K°_S are applied.

When the tracks are refit with these constraints using the general algorithm discussed in the next section, their parameters are forced to satisfy the constraints, thereby improving the mass and momentum resolution of all final-states and, thereby, intermediate particles, such as η_c. These resolution improvements will translate to a larger signal-to-background ratio and frequently elevate marginal signals to statistical significant results. Figure 4.4 depicts the invariant-mass of $K^\circ_S K\pi\pi\pi$ attributed to the channel $\psi^{'} \to \gamma K^\circ_S K\pi\pi\pi$. Three peaks can be observed that correspond to the decay of the three L=1 charmonium states, namely the $\chi_{c0}, \chi_{c1}, \chi_{c2}$. The data points depict the invariant-mass distribution obtained from the measured variables before a 4C fit and the filled histogram corresponds to the result after a 4C fit. The filled histogram is obtained after a 4C kinematic fit for which we keep only the events for which, $\chi^2<55$, and we modified the momenta of the final-state products according to the constraints of the fit. This figure illustrates the power of kinematic fitting. It demonstrates that it helps to reduce the number of background events and to improve the momentum resolution of the detected charged tracks. The resolution of the χ_{c0} signal hardly improves compared to that of χ_{c1} and χ_{c2} signals. This is due to the fact that the natural width of χ_{c0} ($\Gamma_{\chi_{c0}} = 10.5$ MeV) is much larger than those of the χ_{c1} and χ_{c2} ($\Gamma_{\chi_{c2}} = 1.93$ MeV). For more details about kinematic fitting, see Appendix A.

4.5.1 Track representation

For kinematic fitting, it is important to choose the track representation which uses physically meaningful quantities and which is complete. Here, 7-parameter W format, defined as $\alpha_W = (p_x, p_y, p_z, E, x^{'}, y^{'}, z^{'})$, with a 4-momentum and a point where the 4-momentum is evaluated, is adopted in the kinematic fitting software package. $x^{'}, y^{'}, z^{'}$, might differ from the vertex where the beam interaction takes place. It is easy to transfer the parameters and their covariance to the W representation for neutral and charged tracks. By using the W format, it is much simpler to transport particles in a magnetic field, and it will be helpful for vertex fitting. It is noted that the W formats also have enough information to represent the general decays of particles.

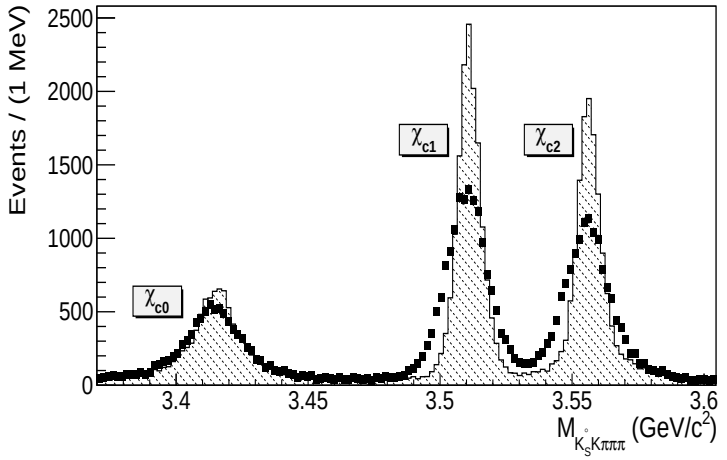

Figure 4.4: The invariant-mass of $K_S^\circ K\pi\pi\pi$. Dots represent the invariant-mass before kinematic fitting and the filled histogram is the result after a 4C fit obtained from our dataset.

4.5.2 Vertex fitting

Consider a set of n tracks forced to pass through a common vertex $X = (x, y, z)$. If the covariance matrix of the vertex is known in advance, the overall χ^2 can then be written as a general form:

$$\chi^2 = (\alpha - \alpha_0)^T V_{\alpha_0}^{-1}(\alpha - \alpha_0) + (x - x_0)^T V_{x_0}^{-1}(x - x_0) + 2\lambda^T(\mathbf{D}\delta\alpha + \mathbf{E}\delta c\tau + \mathbf{d}), \quad (4.10)$$

where the terms represent, respectively, the contribution from tracks, vertex and the constraints, x_0 and V_{x_0} represent the initial vertex position and its covariance matrix, $\delta\alpha = \alpha - \alpha_A$ and $\delta x = x - x_A$, $E_{ij} = \frac{\partial H_i}{\partial x_j}$. $\mathbf{D}$ and $\mathbf{d}$ matrices are defined as:

$$\mathbf{D} = \begin{pmatrix} -2p_x & -2p_y & -2p_z & 2E & 0 & 0 & 0 \end{pmatrix}; \quad (4.11)$$

$$\boldsymbol{d} = E^2 - p_x^2 - p_y^2 - p_z^2 - m_c^2 = 0. \quad (4.12)$$

After the vertex fitting, track parameters and their covariance matrix should be updated to the vertex position. The track parameters can be written in matrix form [58],

$$\alpha_V = \begin{pmatrix} p_V \\ x_V \end{pmatrix}. \quad (4.13)$$

4.5.3 The decay vertex reconstruction

In the present work, we study the decay sequence $\psi^{'} \to \pi^{\pm}\pi^{\mp}J/\psi,\ J/\psi \to \gamma\eta_c,\ \eta_c \to K^{\circ}_S K^{\pm}\pi^{\mp}$. The K°_S particle is reconstructed first, since it does not decay at the IP. Figure 4.5 illustrates a K°_S that decays into a pair of pions at the secondary vertex. Having been produced in the IP region and after traveling a certain distance, s, it decays to a pair of pions. To reconstruct the K°_S, we assume all the charged tracks are pions, and then the common vertex fit is performed for π^+, π^- by looping over all charged tracks. The IP is determined event-by-event, where event vertices are obtained from the vertex fit. The decay point of the K°_S is determined by the common vertex fit. It could be obtained by the K°_S flight direction from the IP by considering the tracking error of the daughter particles. This constraint between the IP and the decay point is called the second-vertex fit.

To reconstruct the K°_S, the IP, (x_p, y_p, z_p), and the decay vertex fit, (x_d, y_d, z_d), should be in a straight line along the K°_S trajectory. The set of equations are defined as following:

$$x_p - x_d - \frac{p_x}{m}c\tau = 0, \tag{4.14}$$

$$y_p - y_d - \frac{p_y}{m}c\tau = 0, \tag{4.15}$$

$$z_p - z_d - \frac{p_z}{m}c\tau = 0. \tag{4.16}$$

where (p_x, p_y, p_z) is the momentum of K°_S, m is the mass of K°_S, c is the speed of light and τ is the life-time of K°_S. The goodness-of-fit parameter, χ^2, is defined as:

$$\chi^2 = (\alpha_{fit} - \alpha_0)^T V^{-1}_{\alpha_0}(\alpha_{fit} - \alpha_0); \tag{4.17}$$

where

$$\alpha = (p_x, p_y, p_z, E, x_d, y_d, z_d, x_p, y_p, z_p)^T. \tag{4.18}$$

α_{fit} is the value of α after the decay length fit, α_0 is the initial value of α and V_{α_0} is the error matrix of α_0. The v_α value is determined via control channels by using MC information. The decay vertex reconstruction is used to study the decay channel, $\psi^{'} \to \pi^{\pm}\pi^{\pm}J/\psi,\ J/\psi \to \gamma\eta_c,\ \eta_c \to K^{\circ}_S K^{\pm}\pi^{\mp}$, $K^{\circ}_S \to \pi^+\pi^-$.

4.6 General selection criteria

The general selection criteria include all the requirements which are applied by the collaboration to improve the signal-to-noise ratio. These criteria were determined by the working groups at BESIII.

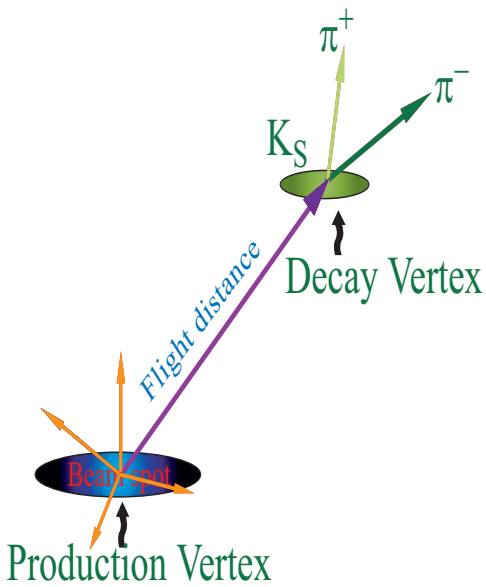

Figure 4.5: A K_S° travels a certain distance before decaying into its daughters. These daughters are subsequently measured by the tracking system.

- Photons:

  Photon candidates are selected based on information from the EMC detector covering barrel and end-cap. The barrel is defined as the area $|\cos\theta| < 0.83$ and the end-cap is defined as $0.85 < |\cos\theta| < 0.95$. The following conditions have been applied:

  – Angle cut
  To eliminate showers from charged tracks, the angle between the photon and the closest charged track should be larger than 20°;

  – Energy threshold
  To effectively reject background hits, the energy deposition in the barrel region is required to be greater than $E_{barrel} > 25$ MeV and in the EMC end-cap is required to be $E_{end-cap} > 50$ MeV;

  – EMC time
  Timing requirements are used to suppress electronic noise and energy deposits in the EMC unrelated to the event: $0 \leq t \leq 700$ ns;

- Charged tracks:

  Charged track candidates are selected based on the MDC information, i.e., the polar angle and vertex coordinate.

  - Polar angle in MDC
    Since the inner radius of MDC is 60 mm and outer radius is 800 mm, tracks must be within the MDC volume of $|\cos\theta| < 0.93$.
  - Vertex cuts
    The tracks must originate from a cylindrical volume, centered around the i^{th} interaction point, which is defined by a radius of 1 cm perpendicular to the beam axis and a length of ± 10 cm along the beam axis.

Chapter 5

Data Analysis of $J/\psi \to \gamma\eta_c$

An exclusive study of the spin-singlet S-wave state of charmonium, η_c, has been performed by observing the decay chain, $\psi^{'} \to \pi^{\pm}\pi^{\mp}J/\psi,\ J/\psi \to \gamma\eta_c,\ \eta_c \to K^{\circ}_{S}K^{\pm}\pi^{\mp}$. The main aim of this analysis is a measurement of the basic properties of the η_c such as the mass (M), width (Γ) and a measurement of the branching fraction of the M1 transition, $\mathcal{B}(J/\psi \to \gamma\eta_c)$. Earlier studies of the M1 transition $\psi^{'} \to \gamma\eta_c$ by BESIII [26] demonstrated that the extraction of these parameters was sensitive to an interference of the signal with a non-resonant background that appeared strongly in the measurements. Our aim is to study these effects in the complementary M1 transition $J/\psi \to \gamma\eta_c$ with the hope to provide further insights into the underlying mechanism that induced such an interference and to provide an alternative measurement of the mass and width of the ground state of charmonium, η_c. Moreover, a measurement of the M1 transition rate can be used to confront state-of-the art calculations to learn more about the dynamics of this electromagnetic process.

A $K^{\circ}_{S}K^{\pm}\pi^{\mp}$ invariant-mass reconstruction of the $J/\psi \to \gamma K^{\circ}_{S}K^{\pm}\pi^{\mp}$ final-state gives access to a measurement of the η_c parameters. Background contributions from $\psi^{'} \to \gamma\chi_{cJ=0,1,2}$ and $\psi^{'} \to \pi^{\circ}K^{\circ}_{S}K^{\pm}\pi^{\mp}$ have been studied and accounted for by using (partially) a data-driven approach in combination with Monte Carlo (MC) studies.

We perform a fit of the data by using a probability density function (PDF) which contains the signal, different sources of background, the interference between signal decays and non-resonant background and detector response and detection efficiency, to extract the number of signal events. The MC studies are performed to obtain the reconstruction efficiency and detection resolution. As a result of the fit M and Γ of the η_c and $\mathcal{B}(J/\psi \to \gamma\eta_c)$ are obtained. In this chapter, a detailed description of the exclusive analysis of $J/\psi \to \gamma\eta_c$ is presented.

5.1 Data sample and MC simulation

To experimentally determine the η_c line shape in the $J/\psi \to \gamma\eta_c$ transition, the following data set and MC samples are used.

5.1.1 Data set

In this analysis, data taken in 2009 and 2012 at a center-of-mass energy corresponding to the $\psi^{'}$ resonance are used. We refer to these data as the 2009 and 2012 $\psi^{'}$ data sets. The 2009 $\psi^{'}$ data set was accumulated by BESIII from March 7 to April 4, 2009 and the 2012 $\psi^{'}$ data set was accumulated by BESIII from April 10 to May 22, 2012. The total number of $\psi^{'}$ decays from the 2009 data set is determined to be $(106.41 \pm 0.86) \times 10^6$ and the total number of $\psi^{'}$ decays from the 2012 data set is determined to be $(341.1 \pm 0.63) \times 10^6$. Thus, the total number of $\psi^{'}$ decays used in this analysis is $(447.51 \pm 2.9) \times 10^6$ [116], where the uncertainty is dominated by systematics, and the statistical uncertainty is negligible. The BESIII Offline Software System (BOSS), version BOSS 6.6.4, is used for the data reconstruction.

5.1.2 MC samples

For the study of potential background sources, 447×10^6 inclusive MC events were used. The events are generated with the generator EVTGEN [125], which simulates the decay of resonances with the known branching fractions from the PDG [48]. Decay channels with unknown branching fractions are simulated with the Lund-Charm model [126]. The BOSS version for the analysis of the inclusive MC data is BOSS 6.6.4 p01.

In addition to the inclusive MC sample, exclusive MC samples were used for the determination of the detector response and detection efficiency. The JPE decay model is used for the transition $J/\psi \to \gamma\eta_c$ to generate signal events. The channels $\psi^{'} \to \gamma\chi_{cJ=0,1,2}$ are generated with P2GC0, P2GC1 and P2GC2 decay models, respectively, as one of the sources of the background in this analysis. The decay $\psi^{'} \to \pi^{\pm}\pi^{\mp}J/\psi$ is modeled with JPIPI, the decay chain $\psi^{'} \to \gamma\eta_c$, $\eta_c \to K^{\circ}_S K^{\pm}\pi^{\mp}\pi^{\pm}\pi^{\mp}$, $K^{\circ}_S \to \pi^{\mp}\pi^{\mp}$ is modeled with a phase-space distribution and the $\eta_c \to K^{\circ}_S K^{\pm}\pi^{\mp}$ is generated with MassH2. For more details of the various decay models, we refer to section 4.2.1.

5.2 $\mathcal{B}(J/\psi \to \gamma\eta_c)$, M and Γ of η_c

The analysis presented here aims to measure the branching fraction, $\mathcal{B}(J/\psi \to \gamma\eta_c)$, and the mass, M, and the width, Γ of the η_c. The branching fraction, $\mathcal{B}$, is obtained using the following equation:

$$\mathcal{B}_{(J/\psi\to\gamma\eta_c)} = \frac{N_{J/\psi\to\gamma\eta_c}}{\epsilon_{J/\psi\to\gamma\eta_c} \times N_{\psi'} \times \mathcal{B}(\psi' \to \pi\pi J/\psi) \times \mathcal{B}(\eta_c \to K^\circ_S K\pi) \times \mathcal{B}(K^\circ_S \to \pi\pi)}, \tag{5.1}$$

where $N_{\psi'\to\gamma\eta_c}$ is the number of signal events obtained from the fit in the mass region, 2.7 GeV/c^2 $< RM_\gamma <$ 3.072 GeV/c^2, $\epsilon_{\psi'\to\gamma\eta_c}$ is the efficiency which will be determined from MC simulations, $N_{\psi'}$ is the total number of ψ' events, $\mathcal{B}(\psi' \to \pi\pi J/\psi)$ and $\mathcal{B}(K^\circ_S \to \pi\pi)$ are taken from the PDG [48] and $\mathcal{B}(\eta_c \to K^\circ_S K\pi)$ from a published BESIII analysis [26]. The fit strategy to extract the number of signal events and the procedure to obtain the efficiency via a MC study are explained in Sections 5.3 and 5.8, respectively. M and Γ of the η_c are kept as free parameters in the fit. The number of signal events are obtained from the fit as well to determine $\mathcal{B}(J/\psi \to \gamma\eta_c)$.

5.3 General fitting strategy

In order to obtain $\mathcal{B}$, M and Γ for the resonance of interest, we reconstruct the invariant-mass, m, spectrum from the information of the decay particles. This spectrum is fitted by a function $F(m)$ that contains a model of the signal, background and possible interference contributions. The probability density function, $F(m)$, contains the following components:

$$F(m) = \Big(\epsilon(m)\big|BW(m) \times e^{i\phi} + \alpha N(m)\big|^2 \times E^3_\gamma \times f_d(E_\gamma)\Big) \otimes DR + B(m), \tag{5.2}$$

where $\epsilon(m)$ is the mass-dependent efficiency, $BW(m)$ refers to the Breit-Wigner function describing the signal, α is the strength of the interfering non-resonant component with the same final-states as the signal, $N(m)$ is the corresponding non-resonant amplitude, E^3_γ is the phase-space factor with E_γ representing the energy of the transition photon, f_d is the damping factor, $\otimes$ is the convolution symbol, DR is the detector response and ϕ reflects the interference phase between the signal and the non-resonant background. $B(m)$ contains backgrounds from the final-state radiation (FSR), $J/\psi \to \gamma_{FSR} K^\circ_S K^\pm\pi^\mp$, and $J/\psi \to \pi^\circ K^\circ_S K^\pm\pi^\mp$ process. The various components of the fit function are described below.

5.3.1 Description of the signal

The signal is described by a BW modified by a factor E_γ^3. This factor is needed to get proper matrix elements but leads to a diverging tail at lower masses. To damp the E_γ^3 term, an additional factor is added, which is called the damping factor. The damping factor in our fit is taken from KEDR for a similar process [45] and is given by:

$$f_d(E_\gamma) = \frac{E_0^2}{E_\gamma E_0 + (E_\gamma - E_0)^2}, \tag{5.3}$$

where E_γ is the energy of the radiative photon and E_0 is the photon energy at the η_c nominal mass, $m_{\eta_c}^2$:

$$E_\gamma = \frac{m_{\psi'}^2 - m^2}{2m_{\psi'}}, \tag{5.4}$$

$$E_0 = \frac{m_{\psi'}^2 - m_{\eta_c}^2}{2m_{\psi'}}, \tag{5.5}$$

where $m_{\psi'}$ is the nominal $\psi^{'}$ mass, 3.686 GeV/c^2. The signal is convoluted with the Detector Response (DR) which is explained in more details in Section 5.8. The BW distribution as a function of mass, m_{η_c}, is given by:

$$BW(m) = \frac{1}{(m^2 - m_{\eta_c}^2) + i m_{\eta_c}\Gamma}, \tag{5.6}$$

where m_{η_c} and Γ are the mass and width of the η_c, respectively. The values of the mass and width are kept as free parameters in the final fit.

5.3.2 Background

In the fitting procedure, we studied in detail three different sources of background, namely $J/\psi \to \gamma_{FSR} K_S^\circ K^\pm \pi^\mp$, $J/\psi \to \pi^\circ K_S^\circ K^\pm \pi^\mp$ and the contribution of a possible non-resonant background with the same final-state as the signal. In equation 5.2, the $B(m)$ term contains the background channels, $J/\psi \to \gamma_{FSR} K_S^\circ K^\pm \pi^\mp$ and $J/\psi \to \pi^\circ K_S^\circ K^\pm \pi^\mp$ and the $N(m)$ term includes the non-resonant background. The procedure that was used to determine the line shape of the backgrounds is explained in more detail in Section 5.7.

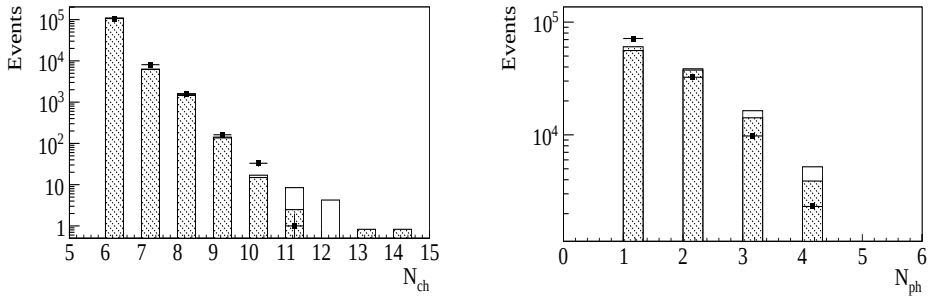

Figure 5.1: Left: The distribution of charged track multiplicity per event, Right: The distribution of photon multiplicity per event. Dots represent data, filled histograms represent the result of inclusive MC and open histograms represent the result of exclusive MC. The MC histograms are scaled to match the integral of the number of events in the data sample.

5.4 Event selection for $\psi' \to \gamma K_S^\circ K^\pm \pi^\mp \pi^\pm \pi^\mp$

The following criteria are used to select the $\psi' \to \pi^\pm \pi^\mp J/\psi$, $J/\psi \to \gamma \eta_c$, $\eta_c \to K_S^\circ K^\pm \pi^\mp$ final-states:

- Assume all charged tracks are π traces;
- The total number of neutral tracks, N_{ph}, is required to be more than 0 and less than 5 and the number of charged tracks, N_{ch}, is required to be at least 6 with the sum of charges equal to zero. The comparison between data, inclusive and exclusive MC is shown in Figure 5.1. Dots represent the data, filled histograms represent the results of the inclusive MC simulation and histograms represent the results of the exclusive MC. The histograms corresponding to MC studies are scaled to the number of events in the data sample. The maximum deviation between data and inclusive MC simulation for any bin is about 9% and between data and exclusive MC is about 10%.
- K_S° is reconstructed from the decay of $K_S^\circ \to \pi^+ \pi^-$. A kinematic constraint between the production and decay vertices, and a second-vertex fitting algorithm based on the least squares method are employed [121][1]. To suppress the combinatorial background, it is required that the ratio of the reconstructed decay length over its error ($L_{K_S^\circ}/\sigma_L$) is greater than three. The $L_{K_S^\circ}/\sigma_L$ distribution is shown

[1] For more details see subsection 4.5.3

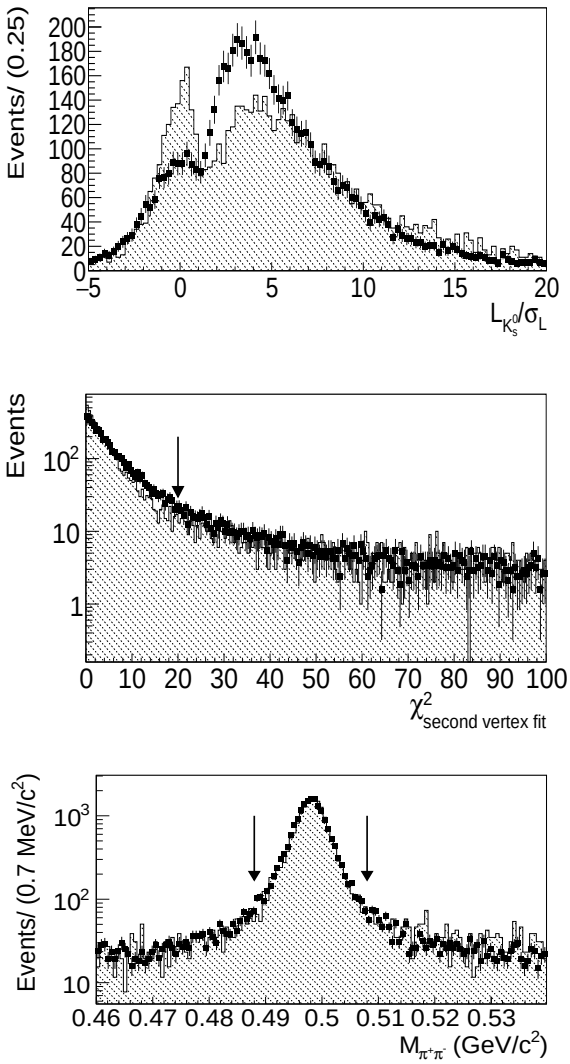

Figure 5.2: Top: The decay length over its error ($L_{K_S^\circ}/\sigma_L$), Middle: the $\chi^2_{\text{second vertex fit}}$ distribution, Bottom: the invariant-mass distribution of selected K_S° candidates. The results of data are compared with results of an exclusive MC study of the signal process. Dots represent data and histograms represent the exclusive MC.

in the top panel of Figure 5.2. The middle panel in Figure 5.2 shows the χ^2 distribution related to the secondary vertex fit. A cut of $\chi^2 < 20$ is applied as a

further selection criteria which is shown with arrow in Figure 5.2. If more than one $\pi^+\pi^-$ combination is found that matches a K°_{S} signature, the combination with the closest mass value to the K°_{S} nominal mass is selected as a good candidate. Finally, it is required that the mass of the reconstructed K°_{S} candidate after a vertex fit falls in the region, $|M_{K^{\circ}_{S}} - 0.498| < 10$ MeV which is shown with arrows in bottom panel of Figure 5.2. The invariant-mass of good K°_{S} candidates is shown in the bottom panel of Figure 5.2.

- General selection criteria have been applied for the remaining charged tracks and neutral tracks. Details are described in Section 4.6.

- After the selection of charged tracks from the K°_{S} decay, the total number of remaining charged tracks is required to be equal to four, corresponding to two positively and two negatively charged tracks in the final-state.

- The remaining charged tracks in each event can be $K^+\pi^-\pi^+\pi^-$ or $K^-\pi^+\pi^-\pi^+$. The information from TOF and *dE/dx* is combined to form a likelihood $\mathcal{L}(K)$ (or $\mathcal{L}(\pi)$) with the assumption that the track is assigned to a kaon (or pion). We loop over all possible combinations and it is assumed that one of the charged tracks is a kaon and the other three charged tracks are pions. To improve the efficiency of the reconstruction, the χ^2 of particle identification for the kaon, χ^2_K, and three pions, χ^2_π, are added together to form the total χ^2 of PID, χ^2_{PID}. A kinematic fit of all identical candidates to the initial ψ' four-momentum is performed to improve the mass resolution. For more details of this 4C kinematic fit, we refer to section 4.5. Throughout the chapter, all the distributions are obtained from parameters after performing a 4C kinematic fit unless stated otherwise. A 4C kinematic fit is performed for all the remaining candidates of photon and K°_{S} candidates with the selected $K3\pi$ tracks. Then, the χ^2 of the 4C kinematic fit (χ^2_{4C}) is added to the total χ^2_{PID}. We define a combined 4C and PID χ^2:

$$\chi^2_{PID+4C} = \chi^2_{4C} + \chi^2_{PID}. \tag{5.7}$$

The combination with the smallest χ^2_{PID+4C} is selected. The left panel of Figure 5.3 shows χ^2_{4C} and the right panel compares the χ^2_{PID+4C} distribution of the results of data, inclusive and exclusive MC samples. By analyzing the significance distributions of the inclusive MC sample, an optimum of χ^2_{PID+4C} of 55 was found and used to reject background. This cut corresponds to the maximum value of the significance, $\frac{N_{Signal}}{N_{Signal}+N_{Background}}$, where N_{Signal} is the number of signal events and $N_{Background}$ is the number of background events.

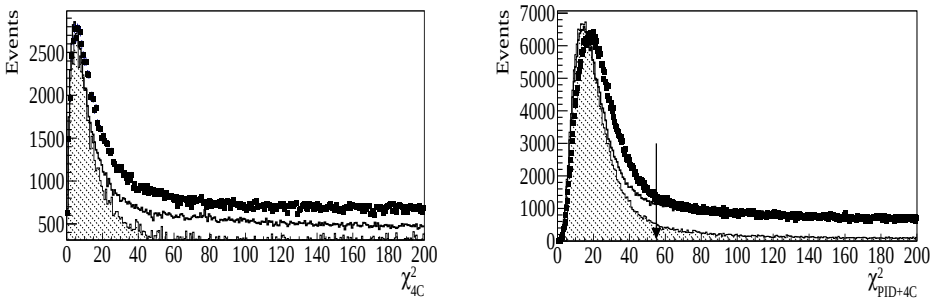

Figure 5.3: Left: The χ^2_{4C} distribution and Right: χ^2_{PID+4C} distribution for the transition $\psi' \to \gamma K^\circ_S K^\pm \pi^\mp \pi^\pm \pi^\mp$. Dots represent the data, open and filled histograms represent the inclusive and exclusive MC results, respectively.

5.5 J/ψ event selection

The identification of the J/ψ is done by using the recoil mass of $\pi^+\pi^-$ pair, $RM_{\pi\pi}$, coming from the ψ' to J/ψ transition. $RM_{\pi\pi}$ is obtained from taking the invariant-mass of the four-momentum difference between the ψ' momentum and that of the four-momentum sum of the transition $\pi^+\pi^-$ pair. Figure 5.4 shows the $RM_{\pi\pi}$ distribution and there is a clear peak around the J/ψ mass, 3.096 GeV/c^2, with a resolution of about 1 MeV. There are several positive aspects by using a J/ψ identification based on the $RM_{\pi\pi}$ analysis. With this method, we will be able to perform a side-band analysis which will allow us to obtain a data-driven background estimate. The side-band analysis is explained in more detail in section 5.6. We also note that the branching fraction of $\psi' \to \pi^\pm\pi^\mp J/\psi$ is $(31.7 \pm 1.1)\%$ and, therefore, we obtain high statistics from the available large ψ' data sample. The signal region is chosen to be 3.08 GeV/c^2 $< RM_{\pi\pi} <$ 3.11 GeV/c^2. After boosting the J/ψ momenta to its rest frame, we calculate the recoil mass of the transition photon. The results are shown in Figure 5.5. There are two clear peaks which are attributed to the η_c which is around 2.894 GeV/c^2 and the contribution from the final-state radiation, γ_{FSR}, which peaks at the maximum kinematically allowed recoil mass of 3.096 GeV/c^2.

5.6 Side-band analysis

One of the main motivations of the present analysis is related to the production and decay of the $\chi_{cj=0,1,2}$ states. Figure 5.6 shows the contribution of the $\chi_{cJ=0,1,2}$ back-

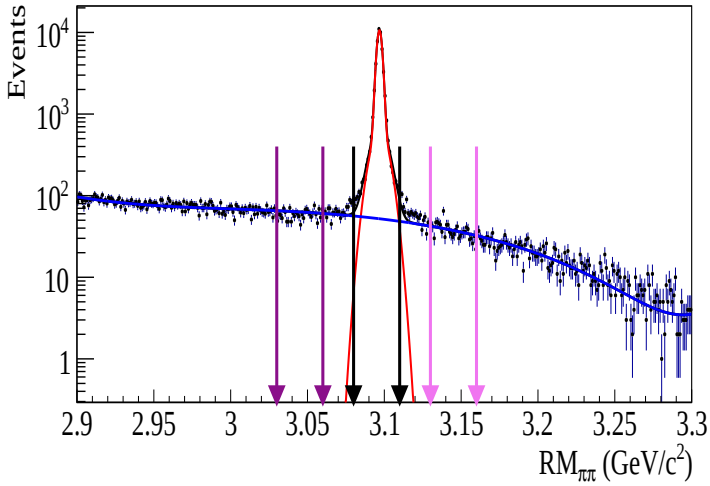

Figure 5.4: The $RM_{\pi\pi}$ distribution for events from $J/\psi \to \gamma\eta_c,\ \eta_c \to K^{\circ}_{S}K^{\pm}\pi^{\mp}$. Signal is shown with red curve and background is shown with blue curve. Three regions that were used to select the signal and background events are indicated as well. The signal region ($3.08 < RM_{\pi\pi} < 3.11$) is shown with black arrows, the left side-band ($3.03 < RM_{\pi\pi} < 3.06$) with purple arrows and the right side-band ($3.13 < RM_{\pi\pi} < 3.16$) with pink arrows.

ground within the RM_{γ} distribution. In this plot, events from the channel of interest, $J/\psi \to \gamma\eta_c,\ \eta_c \to K^{\circ}_{S}K^{\pm}\pi^{\mp}$ appear in a blob around $RM_{\gamma} = 2.983$ GeV/c^2 and $E_{\gamma} = 0.110$ GeV. Three horizontal lines around $E_{\gamma} = 0.120$ GeV, $E_{\gamma} = 0.170$ GeV and $E_{\gamma} = 0.260$ GeV correspond to the photon energies related to populating the χ_{c0}, χ_{c1}, and χ_{c2}, respectively. These three lines are events from $\psi^{'} \to \gamma\chi_{cj=0,1,2},\ \chi_{cj=0,1,2} \to K^{\circ}_{S}K^{\pm}\pi^{\mp}\pi^{\pm}\pi^{\mp}$. The horizontal line around $E_{\gamma} = 0.636$ GeV corresponds to the η_c from $\psi^{'} \to \gamma\eta_c,\ \eta_c \to K^{\circ}_{S}K^{\pm}\pi^{\mp}\pi^{\pm}\pi^{\mp}$.

A side-band analysis of the $RM_{\pi\pi}$ is performed to estimate and subtract the contributions from the $\chi_{cj=0,1,2}$ backgrounds in the RM_{γ} distribution. For doing the side-band analysis, three different regions of signal and side-bands are selected as shown in Figure 5.4. The signal region is shown with black arrows (3.08 GeV/$c^2 < RM_{\pi\pi} < 3.11$ GeV/c^2), left side-band region with purple arrows (3.03 GeV/$c^2 < RM_{\pi\pi} < 3.06$ GeV/c^2) and right side-band region with pink arrows (3.13 GeV/$c^2 < RM_{\pi\pi} < 3.16$ GeV/c^2). Figure 5.7 shows the effect of the two side-bands in our region of interest, 2.6 GeV/$c^2 < RM_{\gamma} < 3.11$ GeV/c^2. The purple distribution is attributed to the left side-band and the pink distribution to the right side-band. The first peak corresponds

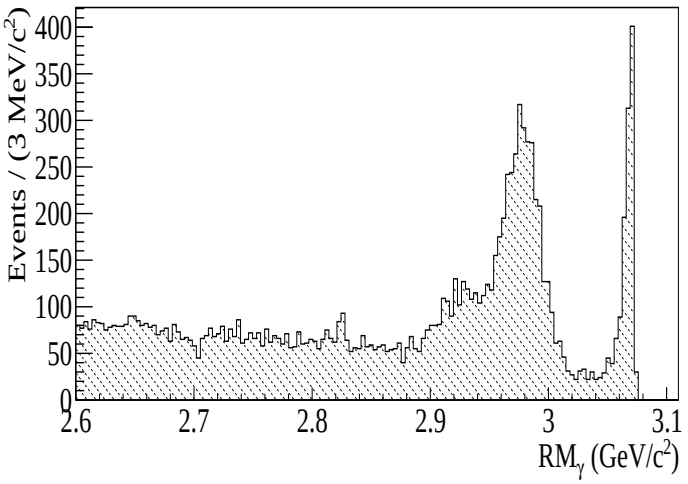

Figure 5.5: RM_γ distribution for events in the signal region of Figure 5.4 after a momentum boost obtained from the data set for the transition $J/\psi \to \gamma\eta_c$, $\eta_c \to K^\circ_S K^\pm\pi^\mp$, $K^\circ_S \to \pi^+\pi^-$.

to χ_{c0}, the second peak to χ_{c1} and the third peak to χ_{c2}. The line shape of the $\chi_{cj=0,1,2}$ states is obtained from data. Left and right side-bands are added together and then the normalized result is subtracted from the signal. The final result after subtraction the $\chi_{cj=0,1,2}$ background is shown in Figure 5.8 and is compared with the result of the inclusive MC data. This comparison shows that the inclusive data does not contain all sources of backgrounds such as $\pi^\circ K^\circ_S K^\pm\pi^\mp$, $\gamma K^\circ_S K^\pm\pi^\mp$ and that the signal is not well described. We continue with a more data-driven method to understand the other sources of background in this analysis.

5.7 Sources of backgrounds

To study the background from the $J/\psi \to \pi^\circ K^\circ_S K^\pm\pi^\mp$, a data-driven method is used. To obtain the shape of $J/\psi \to \gamma_{FSR} K^\circ_S K^\pm\pi^\mp$ background, the inclusive MC sample is used. The remaining background is, in the first instance, modeled as a flat distribution in the considered interval following a similar procedure as described in reference [26]. All the components are explained in detail in the following.

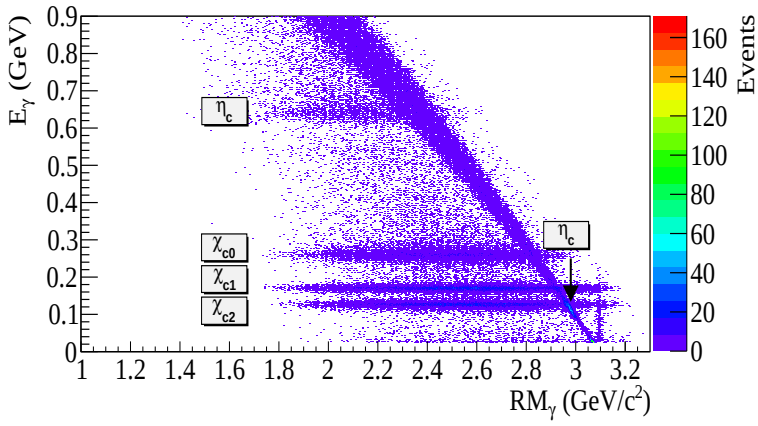

Figure 5.6: The energy of photon, E_γ, varsus the RM_γ. Events from the channel of interest appear as a blob around $RM_\gamma = 2.983$ GeV$/c^2$ and $E_\gamma = 0.111$ GeV. Three horizontal lines around $E_\gamma = 0.128$ GeV, $E_\gamma = 0.171$ GeV and $E_\gamma = 0.261$ GeV correspond to χ_{c0}, χ_{c1} and χ_{c2}, respectively. These three lines are events from $\psi^{'} \to \gamma\chi_{cj=0,1,2}$, $\chi_{cj=0,1,2} \to K^\circ_S K^\pm\pi^\mp\pi^\pm\pi^\mp$. The data around $E_\gamma = 0.636$ GeV correspond to $\psi^{'} \to \gamma\eta_c$, $\eta_c \to K^\circ_S K^\pm\pi^\mp\pi^\pm\pi^\mp$.

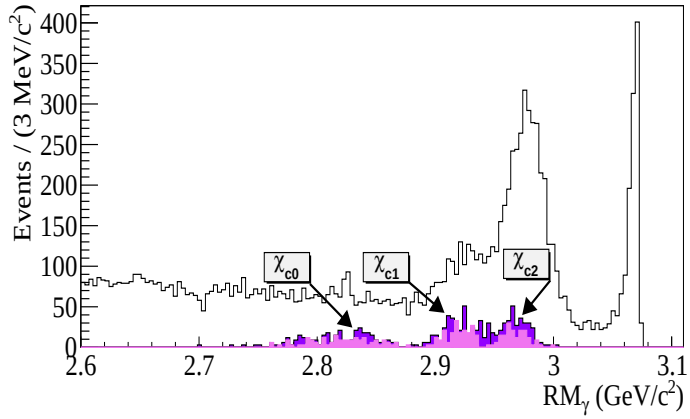

Figure 5.7: The RM_γ distribution for three selected regions in $RM_{\pi\pi}$. The black histogram corresponds to the signal region whereas the pink and purple distributions are attributed to the left and right side-bands, respectively.

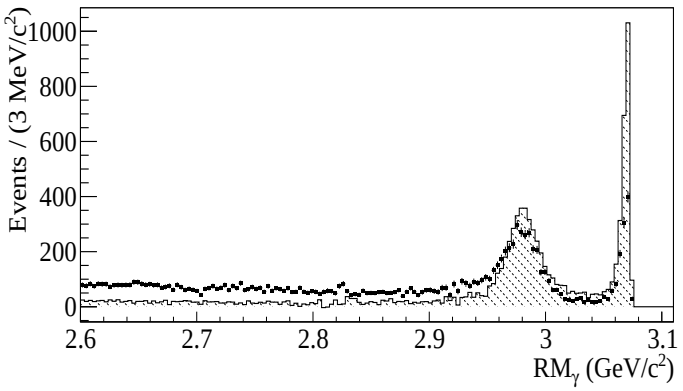

Figure 5.8: RM_γ distribution after subtracting the side-band data. The result of the data is compared with the result of the inclusive MC sample. Dots represent the data and the filled histogram represents the inclusive MC data.

5.7.1 π° background

The background contribution from the channel $\psi' \to \pi^\circ K^\circ_S K^\pm \pi^\mp$ is estimated by selecting data with at least one additional photon in the final-state in order to identify unambiguously π° events. The top panel of Figure 5.9 shows the $\pi^\circ K^\circ_S K^\pm \pi^\mp$ mass, $M_{\pi^\circ K^\circ_S K^\pm \pi^\mp}$, versus the two-photon mass, $M_{\gamma\gamma}$. Note that the kinematic variables are taken before the 4C kinematic fit. The $M_{\gamma\gamma}$ distribution is obtained by making a loop over all the photons. A blob around the π° mass and J/ψ mass can be observed showing a strong contribution from $J/\psi \to \pi^\circ K^\circ_S K^\pm \pi^\mp$ decays. Events falling in the region, $0.125\ \text{GeV}/c^2 < M_{\gamma\gamma} < 0.142\ \text{GeV}/c^2$, are selected for further analysis.

The bottom panel of Figure 5.9 shows the expected contribution of the $\pi^\circ K^\circ_S K^\pm \pi^\mp$ background in the RM_γ spectrum. The shape of this background is obtained from data for which the difference between single and double photon detection efficiency is compensated for by a MC study. The correction is related to the inconsistency in the number of photons in the final-state since in the $\pi^\circ K^\circ_S K^\pm \pi^\mp$ event selection there are at least two photons in the final-state and in our region of interest there can be only one photon. This correction is applied by modifying the recoil mass distribution from $\pi^\circ K^\circ_S K^\pm \pi^\mp$ data by multiplying with a RM_γ dependent correction:

$$\frac{\gamma K^\circ_S K^\pm \pi^\mp \text{ distribution obtained from MC}}{\pi^\circ K^\circ_S K^\pm \pi^\mp \text{ distribution obtained from MC}}. \tag{5.8}$$

In this manner, the obtained shape and absolute scale is fixed in the final fit.

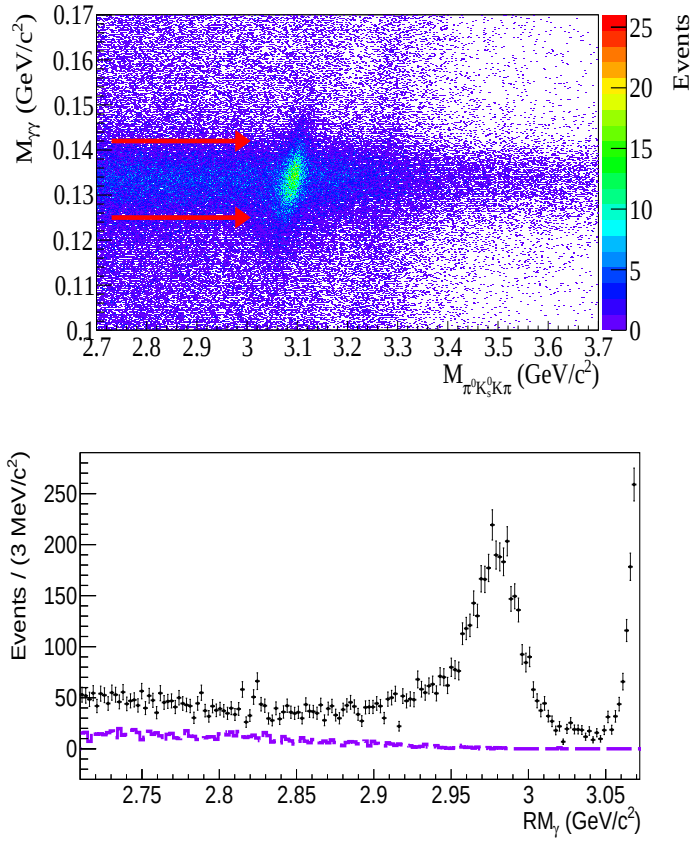

Figure 5.9: Top: $M_{\pi^\circ K_S^\circ K\pi}$ versus $M_{\gamma\gamma}$ for the events from the $J/\psi \to \gamma\eta_c$, $\eta_c \to K_S^\circ K^\pm\pi^\mp$ transition. The kinematic variables are before the 4C kinematic fit. Bottom: Contribution of $\pi^\circ K_S^\circ K^\pm\pi^\mp$ background in the RM_γ distribution. Dots represent all the data events for $J/\psi \to \gamma\eta_c$, $\eta_c \to K_S^\circ K^\pm\pi^\mp$ transition and the purple line represents the $J/\psi \to \pi^\circ K_S^\circ K^\pm\pi^\mp$ distribution.

5.7.2 γ_{FSR} background

The shape of the Final-State Radiation, γ_{FSR} background, might depend on the dynamics of the decay into $K_S^\circ K^\pm\pi^\mp$. We have studied this aspect by selecting the

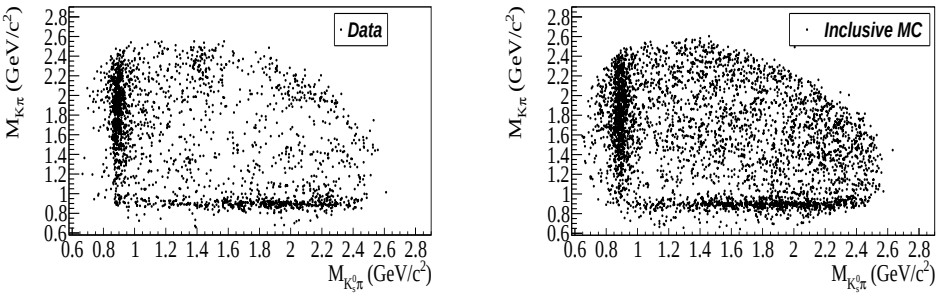

Figure 5.10: Dalitz plots of $K^\circ_S K^\pm\pi^\mp$ candidates for the reaction $J/\psi \to \gamma\eta_c$, $\eta_c \to K^\circ_S K\pi$, obtained from data (left) and inclusive MC (right).

$J/\psi \to \gamma_{FSR} K^\circ_S K^\pm\pi^\mp$ events from the inclusive MC sample. The decay dynamics is shown for the MC in the right-hand panel in Figure 5.10 using a Dalitz representation. The left-hand panel in Figure 5.10 shows a similar spectrum for data. The events for this spectrum has been obtained by applying a cut of $RM_\gamma > 3.05$ GeV$/c^2$ to have a strong bias on FSR events. Both in data and in MC, one observes a dominant contribution from the $K^*(892)$ resonance. The distribution outside this resonance region is not well simulated by MC although it only contributes to about 5% of the total spectrum. We therefore conclude that the inclusive MC generally gives a reasonable representation of the data. Thus, the inclusive MC is used to get the shape of the γ_{FSR} and the green line in Figure 5.11 shows the normalized contribution of the γ_{FSR} background for the RM_γ distribution.

5.7.3 Non-resonant background

Throughout this thesis, we refer to the non-resonant background as a source of background for which the final-state is identical to that of the signal of interest. In our case, this refers to the final-state $\psi' \to \gamma K^\circ_S K^\pm\pi^\mp$ without an intermediate η_c resonance. This type of background might interfere with our signal, hence we consider such an effect in our fit of the RM_γ spectrum. The shape of the non-resonant background within the signal region is initially assumed to have a shape that corresponds to a flat distribution. However, interference between the signal events and the non-resonant background should be considered. The strength of the non-resonant amplitude is kept as a free parameter in the final fit of RM_γ.

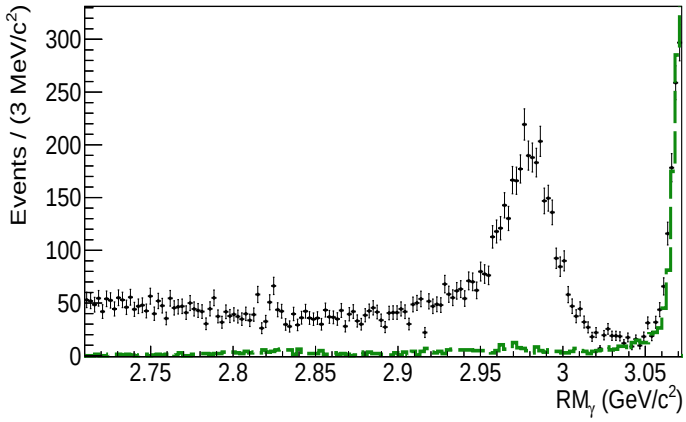

Figure 5.11: Contribution of $J/\psi \to \gamma_{FSR} K_S^\circ K^\pm \pi^\mp$ in the RM_γ distribution which is determined from an inclusive MC study. Dots represent data of the channel $J/\psi \to \gamma K_S^\circ K^\pm \pi^\mp$ and the green line represents the $J/\psi \to \gamma_{FSR} K_S^\circ K^\pm \pi^\mp$ distribution.

5.8 MC studies

To get the line shape for the signal events, $J/\psi \to \gamma\eta_c,\ \eta_c \to K_S^\circ K\pi$, two important effects should be properly accounted for, namely the detector response and the mass-dependent efficiency. The proper model is required to generate the MC signal events to obtain the detector response and efficiency for this analysis. $J/\psi \to \gamma\eta_c$ events are generated by the JPE model which is very reliable. Since the decay $\eta_c \to K_S^\circ K\pi$ might have a complex topology due to contributions from various resonances and their interferences, we studied the Dalitz plot of $K_S^\circ K\pi$ candidates from data and we required our MC simulation to reproduce this spectrum. The top panel of Figure 5.12 shows the Dalitz plot of $K_S^\circ K\pi$ candidates from data. The structure of the Dalitz plot reveals that the phase-space model is not a correct model to generate the exclusive MC sample of $\eta_c \to K_S^\circ K\pi$ events. The obvious structure around 2 GeV/c^2 is related to $K^*(892)$ decays since its dominant decay mode is $K^*(892) \to K\pi$ according to PDG 2016 [48]. The bottom panel of Figure 5.12 shows the Dalitz plot of exclusive MC events which are generated by massH2 model. More details of this model can be found in Section 4.2. This model is obtained by taking experimental data from the process $\psi' \to \pi^\circ h_c,\ h_c \to \gamma\eta_c,\ \eta_c \to K_S^\circ K\pi$ and by applying a correction to the detection efficiency. This channel is selected because it is a clean transition, for which the interference between signal and non-resonant background turns out to be negligible [27] and it is also an independent

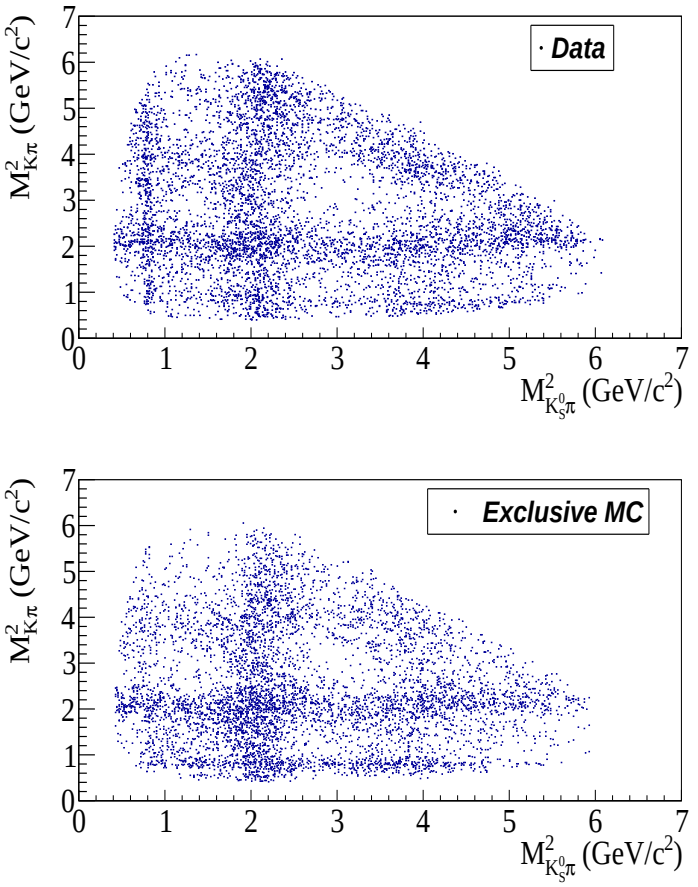

Figure 5.12: The Dalitz plot for the $\eta_c \to K^\circ_S K\pi$ transition obtained from data (top) and exclusive MC (bottom). For more details, we refer to the text.

study. There is a reasonable agreement between the Dalitz plots obtained from exclusive MC and data in Figure 5.12. This enables us to use the exclusive MC result for the determination of the detector response and the detection efficiency.

5.8.1 Detector Response (DR)

Since the η_c is a resonance with a width of about $\Gamma = 30$ MeV, whereas the mass resolution is only about a factor of two smaller than Γ, a good understanding of the detector response is required to study the width. The detector response for signal events

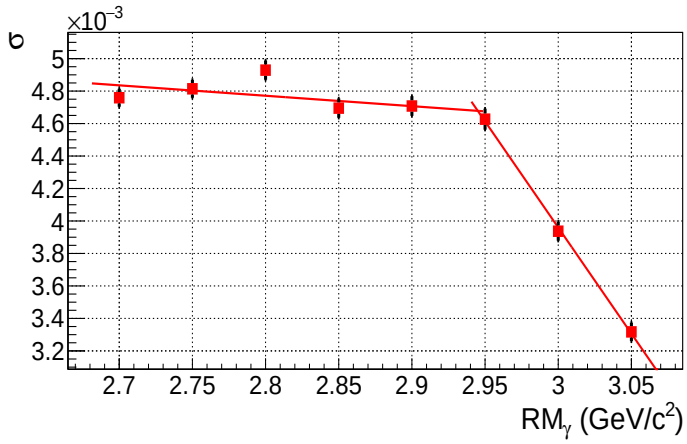

Figure 5.13: The reconstructed mass resolution versus RM_γ. The detector response for each data point is obtained by fitting the RM_γ to the exclusive MC with zero natural width. For more details see text.

is obtained by fitting the RM_γ distribution to an exclusive MC study with zero natural width for the η_c as input. Moreover, we studied the response for eight different η_c-mass input values covering the signal range. For each mass point, the corresponding response distribution is then fitted with a Crystal-Ball function. We define the resolution as the standard deviation, σ, obtained from the Crystal-Ball function. The Crystal-Ball function is defined as follows:

$$\alpha(x) = \begin{cases} \exp(-\frac{(x-\bar{x})^2}{2\sigma^2}), & \text{for} \quad \frac{x-\bar{x}}{\sigma} > -\alpha, \\ A \cdot (B - \frac{x-\bar{x}}{\sigma})^{-n}, & \text{for} \quad \frac{x-\bar{x}}{\sigma} < -\alpha, \end{cases}$$

where $A = \left(\frac{n}{|\alpha|}\right)^n \cdot \exp\left(-\frac{\alpha^2}{2}\right)$ and $B = \frac{n}{|\alpha|} - |\alpha|$. Figure 5.13 shows the energy resolution versus RM_γ. Two first-order polynomial functions are used to describe the resolution as a function of mass. The fitted functions are used to describe the mass-dependent resolution in the final fit of RM_γ, which corresponds to the function DR as indicated in equation 5.2.

5.8.2 Efficiency

A mass-dependent reconstruction efficiency is necessary to be determined in order to minimize the uncertainty in extracting a branching fraction, mass and width. A mass-dependent reconstruction efficiency of our signal events is obtained by fitting the RM_γ

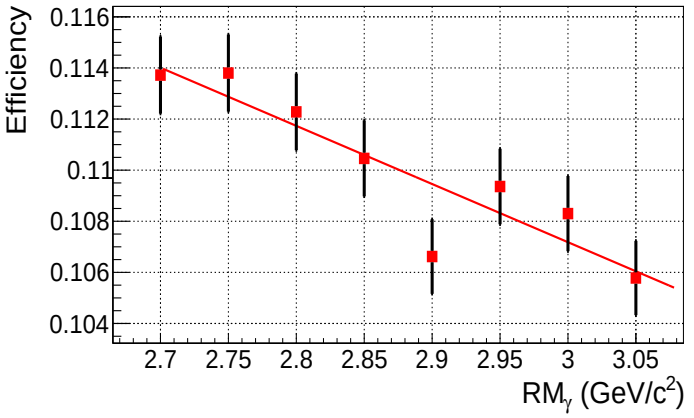

Figure 5.14: The efficiency versus RM_γ. The detector response for each data point is obtained by fitting the RM_γ to the exclusive MC with zero natural width of η_c. For more details see text.

to the exclusive MC with zero natural width at eight different fixed energy points. Each distribution is then fitted by a Crystal-Ball function as described above. The efficiency (ϵ) is calculated from the number of detected events divided by the number of generated events in the exclusive MC sample. The result of the obtained efficiency versus the RM_γ is shown in Figure 5.14. A first-order polynomial is used to describe the mass-dependent efficiency. This function is used to describe the mass-dependent efficiency, $\epsilon(m)$, in the final fit.

5.9 Extraction of mass and width of the η_c resonance

Until now all the different components of the fit function, as given in equation 5.2, have been described individually. In this section we are going to perform the fit for the RM_γ spectrum by considering all the components. We refer to this as the *complete fit*. In this way, we will be able to extract the number of signal events and the mass and width of the η_c. In the complete fit, the shape and the number of $\pi^\circ K^\circ_S K\pi$ background events, and the shape of $\gamma_{FSR} K^\circ_S K\pi$ are fixed. M and Γ of the η_c, the interference phase (ϕ), the strength of the non-resonant background (α), the magnitude of non-resonant background (p_0), the number of counts in the signal (N_{η_c}) and the interference contribution for interference between signal and non-resonant background (N_{inter}) are kept as free parameters. We find two solutions with a similar minimum χ^2 for the

Fitting parameters	constructive fit	destructive fit
$\chi^2/n.d.f$	2.12	2.13
M_{η_c} GeV/c^2	2.9849 $\pm$ 0.0006	2.9851 $\pm$ 0.0001
Γ_{η_c} GeV	0.032 $\pm$ 0.002	0.031 $\pm$ 0.002
α	0.08 $\pm$ 0.03	0.04 $\pm$ 0.01
ϕ (rad.)	2.6 $\pm$ 0.6	4.03 $\pm$ 0.09
p_0	185.0 $\pm$ 27.6	204.2 $\pm$ 9.2
N_{η_c}	3229 $\pm$ 56	4423 $\pm$ 69

Table 5.1: Summary of all the fitting parameters by considering constructive and destructive interference between the signal and the non-resonant background.

interference phase, ϕ, which we label as the constructive and destructive interferences. The complete fit by considering both constructive and destructive interference scenarios are presented in the top and bottom panels of Figure 5.15, respectively. The fit results for the free parameters of the fit are presented in Table 5.1.

5.10 Systematic error

In this section the various sources of systematic errors related to our measurement of the branching fraction, mass and width of the η_c are presented.

5.10.1 Efficiency of the K°_S reconstruction

To determine the efficiency for the reconstruction of the K°_S decays, we strongly depend on the results we obtain from MC simulations. Since the MC simulation might not be a perfect model of reality, we do consider three components that we believe could contribute to the systematic uncertainty related to the K°_S reconstruction. These components include the geometrical acceptance, the tracking efficiency, and the efficiency of the K°_S selection from $M_{\pi\pi}$. The first part is studied by using the exclusive MC simulation of the control sample, $\psi' \to \gamma\chi_{c0}$, $\chi_{c0} \to K^\circ_S K^\pm\pi^\mp\pi^\pm\pi^\mp$. The other two parts are estimated using the measured control channel $J/\psi \to K^{*\pm}K^\mp$, $K^{*\pm} \to K^\circ_S\pi^\mp$. Details of the study of the K°_S reconstruction and corresponding systematic uncertainties are explained in reference [122]. The systematic error attributed to the K°_S reconstruction is estimated to be around 1.4%.

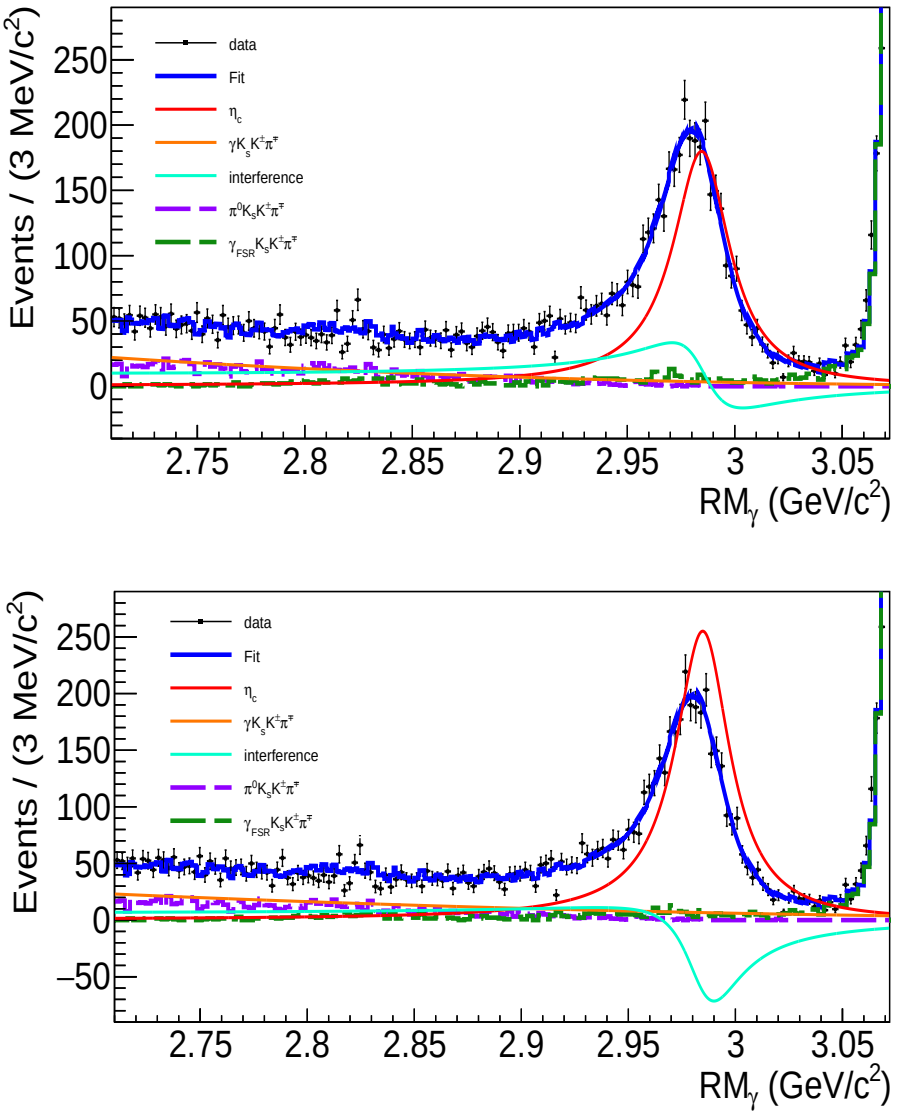

Figure 5.15: The results of a fit through the data using a fit function that incorporates all components considered. Top: by considering for both the constructive interference, Bottom: by considering the destructive interference between the signal and a non-resonant background.

5.10.2 Kinematic fitting error

Since the detector responses are not perfectly modeled in the MC simulation, one might expect deficiencies in the efficiency determination when applying a kinematic fit. Various analyses have been carried out in the past to study its corresponding systematic uncertainty. The most appropriate study related to our work can be found in reference [124]. Here we give a brief summary of these particular studies from which we used its outcomes.

The model that was used in the MC simulation to describe the detector performance is much simpler than reality which cause differences between data and MC simulation in the track parameters of photons and charged tracks. According to the study reported in reference [124] for the simulated detector response for the emitted photon, there is a good agreement between data and MC simulation.

For the charged tracks [124], a comparison between MC and purely selected data samples indicate that the MC simulates the angular resolutions and momentum significantly better than those in data, while matrix elements agree well between data and MC simulation. As a consequence, the χ^2 distribution is on average smaller in MC than in data and it can, therefore, make a bias in the efficiency estimation. To reduce the difference between data and MC simulation, the track helix parameters of MC simulation are corrected. Data from the process $J/\psi \to \phi f_0(980)$, $\phi \to K^+K^-$, $f_0 980 \to \pi^+\pi^-$ are used as control samples to study the difference in the helix parameters of charged tracks between data and MC. The reason for selecting this particular channel is that it has a large production rate, very low background, and has both pions and kaons. Details of this study are presented in reference [122].

The effect of the helix parameters correction for the charged tracks is checked in reference [122] for the $\psi^{'} \to \gamma\chi_{c0}$, $\chi_{c0} \to K^{\circ}_{S}K^{\pm}\pi^{\mp}\pi^{\pm}\pi^{\mp}$ which has the same final-states as our channel of interest. The systematic error was estimated to be 1.5%.

5.10.3 Fit range

The invariant-mass distribution is fitted using several alternatives within the range of [2.70, 3.02] GeV/c^2 and [2.75, 3.072] GeV/c^2. The largest difference in the extracted branching fractions, M and Γ of the η_c within the alternative fitting intervals is taken as a systematic error. The estimated values for the branching fraction is 6% for the constructive interference scenario and 5% for the destructive interference scenario. The systematic uncertainties for M and Γ of the η_c were estimated to be 0.02% and 0.1% for

the constructive interference scenario and 0.05% and 4% for the destructive interference scenario, respectively.

5.10.4 Background shape

In the nominal fit, the background shape is modeled by using combinations of three different sources of background (Section 5.7). Instead of combining different sources of backgrounds to describe the background shape, one exponential and one Chebyshev polynomial are used to estimate a corresponding systematic error. The exponential function describes the γ_{FSR} background and the Chebyshev function can describe the non-resonant background and $\pi^\circ K_S^\circ K^\pm \pi^\mp$ background. The $\chi^2/n.d.f$ values of the fit were 1.47 for the constructive interference scenario and 1.48 for the destructive interference scenario. The difference between the obtained results for the branching fraction, M and Γ of the η_c attributed to the two different kinds of background shapes is taken as a systematic error. The estimated systematic errors for the branching fraction are 0.5% for the constructive interference scenario and 5% for the destructive interference scenario. The systematic error related to M and Γ of the η_c was estimated to be 0.005% and 3% for the constructive scenario and 0.008% and 5% for the destructive scenario, respectively.

5.10.5 Non-resonant background

To estimate the systematic error related to the description of the non-resonant background line shape, the zero-order polynomial is replaced with a first-order and second-order polynomial and the maximum difference is taken as a systematic error. The obtained errors for the branching fraction, M and Γ of the η_c are 7%, 0.01% and 0.3% for the constructive scenario and 10%, 0.006% and 3% for the destructive scenario, respectively.

5.10.6 Efficiency for signal events

To generate the $\eta_c \to K_S^\circ K^\pm \pi^\mp$ events, the massH2 model is used. Deficiencies of the massH2 model can cause a systematic error in the calculation of the reconstruction efficiency. To account for this source of systematic error, $\eta_c \to K_S^\circ K^\pm \pi^\mp$ events are generated with a phase-space (PHSP) model. The difference between the efficiencies obtained with different generator models is taken as a systematic error. The corresponding systematic error is estimated to be 1%.

5.10.7 Damping factor

Two different damping factors have been proposed by the KEDR [46] and CLEO [80] collaborations to describe the line shape properly. In our nominal fit, the damping factor is taken from the KEDR collaboration. To account for the systematic error related to the damping factor function, the damping factor in our nominal fit is replaced with the damping factor used by the CLEO collaboration. The difference between the obtained branching fractions, M and Γ of the η_c based on these two damping factor functions is taken as a systematic error. The obtained errors for the branching fraction, M and Γ of the η_c are 8%, 0.001% and 1% for the constructive scenario and 2%, 0.003% and 2% for the destructive scenario, respectively.

5.10.8 Interference between signal and non-resonant background

We also considered a scenario in which no interference occurs between the η_c signal and the non-resonant background. For this scenario, the value of α is set to zero in equation 6.2. The fit result is presented in Figure 5.16. One observes that the fit curve undershoots and overshoots the data on the left and right side of the signal, respectively. The $\chi^2/n.d.f$ value of the fit is 3.6 which is significantly worse than the scenario including interference effects, therefore, we choose to ignore such a hypothesis. Thus, this source of systematic error is discarded.

5.10.9 Photon reconstruction

The photon detection efficiency is studied utilizing the control samples $\psi^{'} \to \pi^+\pi^- J/\psi$, $J/\psi \to \rho^\circ\pi^\circ$ and $\psi^{'} \to \pi^\circ\pi^\circ J/\psi$ with $J/\psi \to l^+l^-$ $(l = e, \mu)$ and $\rho^\circ\pi^\circ$. The corresponding systematic uncertainty is estimated by the difference of detection efficiency between data and MC samples, and an error of 1% is assigned for each photon [85].

5.10.10 Number of $\psi^{'}$ events

An uncertainty of 0.7% is estimated for the number of $\psi^{'}$ from 2009 events and 0.7% related to the number of $\psi^{'}$ events from 2012 as reported in [84]. These values are adopted in the present analysis.

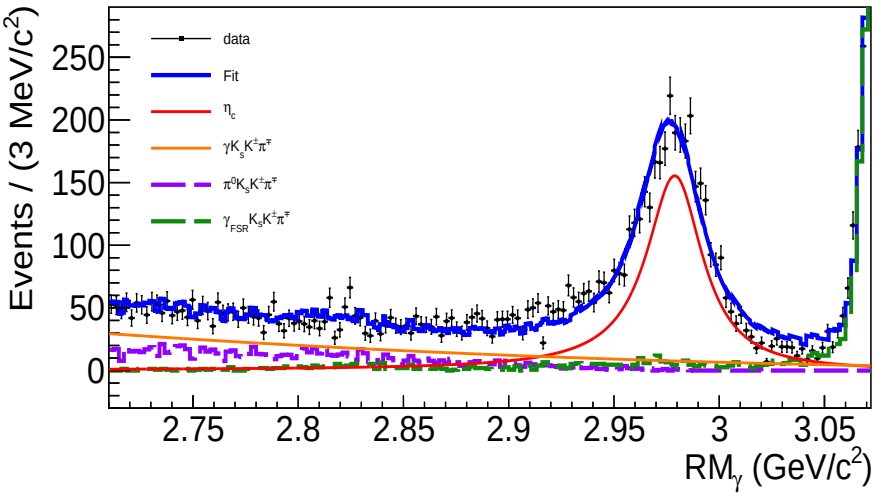

Figure 5.16: Complete fit without considering the interference between signal and non-resonant background.

5.10.11 Trigger efficiency

The uncertainty caused by the trigger efficiency for the ψ' data sample from 2009 is found to be 0.15% [120] and for ψ' data sample from 2012 is estimated to be negligible [84].

5.10.12 MDC tracking

The next uncertainty we considered is related to charged tracks not coming from the K_S°, namely three π and one K which are directly produced at the IP. The tracking efficiencies as a function of transverse momentum have been studied for K and π using the process $J/\psi \to K_S^\circ K^{\pm}\pi^{\mp}$ and $\psi' \to \pi^{\pm}\pi^{\mp}J/\psi$, $J/\psi \to l^+l^-$, respectively. The efficiency difference between data and MC has been estimated to be 2% for each K and π track by the Data Quality/Validation (DQ) group [123]. A total uncertainty of 8% is quoted for the tracking efficiency related to this analysis. The errors add linearly and not quadratically due to the fact that the errors are highly correlated. For instance, if one is off for one charged track, the other charged track will also be off by the same value, therefore, they are not independent.

Syst. error sources / Fit scenario	**Constructive (%)**	**Destructive (%)**
Efficiency of K°_{S} reconstruction	1.4	1.4
Kinematic fitting error	1.5	1.5
Fit range	6	5
Background line shape	0.5	5
Non-resonant background	7	10
Efficiency for the signal events	1	1
Damping factor	8	2
Photon reconstruction	1	1
Number of $\psi^{'}$	0.7	0.7
Trigger efficiency	0.15	0.15
MDC tracking	8	8
$\mathcal{B}(\psi^{'} \to \pi^{\pm}\pi^{\mp}J/\psi)$	0.3	0.3
$\mathcal{B}(\eta_c \to K^{\circ}_{S}K^{\pm}\pi^{\mp})$	0.7	0.7
$\mathcal{B}(K^{\circ}_{S} \to \pi^{\pm}\pi^{\mp})$	0.05	0.05
Total $\sigma_{Syst.Error}$	14	15

Table 5.2: Summary of all the systematic errors for the branching fraction. All the errors are relative to the branching fraction. The total error is obtained by adding the individual errors in quadrature.

5.10.13 Uncertainty of the branching fraction for $\psi^{'} \to \pi^{\pm}\pi^{\mp}J/\psi$, $\eta_c \to K^{\circ}_{S}K^{\pm}\pi^{\mp}$ and $K^{\circ}_{S} \to \pi^{\pm}\pi^{\mp}$

The uncertainties related to our knowledge of the branching fractions, $\mathcal{B}(\psi^{'} \to \pi^{\pm}\pi^{\mp}J/\psi)$, $\mathcal{B}(\eta_c \to K^{\circ}_{S}K^{\pm}\pi^{\mp})$ and $\mathcal{B}(K^{\circ}_{S} \to \pi^{\pm}\pi^{\mp})$ are part of the systematic error of this analysis and their values are taken from PDG 2016 [48], $\mathcal{B}(\psi^{'} \to \pi^{\pm}\pi^{\mp}J/\psi) = (34.45 \pm 0.30)\%$, $\mathcal{B}(\eta_c \to K^{\circ}_{S}K^{\pm}\pi^{\mp}) = (2.0 \pm 0.7)\%$ and $\mathcal{B}(K^{\circ}_{S} \to \pi^{\pm}\pi^{\mp}) = (69.20 \pm 0.05)\%$.

5.10.14 Summary of all the systematic errors

Table 5.2 summarises the systematic errors for the branching fraction and Table 5.3 for the mass M and the width Γ. Assuming all the sources are independent, the total systematic error, $\sigma_{Syst.Error}$, is calculated by adding the individual errors in quadrature.

Syst. error / Fit scenario	**Constructive**		**Destructive**	
	Mass (%)	Width (%)	Mass (%)	Width (%)
Fit range	0.02	0.1	0.05	4
Background line shape	0.005	3	0.008	5
Non-resonant background	0.001	0.3	0.006	3
Damping factor	0.001	1	0.003	2
Total $\sigma_{Syst.Error}$	0.02	3.2	0.05	7

Table 5.3: Summary of all the systematic errors for the mass and width. All the errors are relative to the mass and width.

Experimental groups	$\mathcal{B}(J/\psi \to \gamma\eta_c)$
This work, constructive	$(1.54 \pm 0.01 \pm 0.21) \times 10^{-2}$
This work, destructive	$(2.11 \pm 0.02 \pm 0.31) \times 10^{-2}$
CLEO [80]	$(1.98 \pm 0.09 \pm 0.30) \times 10^{-2}$
CBALL [44]	$(1.27 \pm 0.36) \times 10^{-2}$
PDG [48]	$(1.4 \pm 0.4) \times 10^{-2}$

Table 5.4: Summary of results for our branching fractions compared with other measurements.

5.11 Results and discussion

Discussing and presenting our measurements of $\mathcal{B}\ (J/\psi \to \gamma\eta_c)$, M and Γ of η_c were the main topics of this chapter. In the following, a comparison between obtained results and different experimental measurements and theoretical predictions is presented and the effect of interference between signal decays and non-resonant background on the obtained results will be discussed.

5.11.1 $\mathcal{B}\ (J/\psi \to \gamma\eta_c)$

The measured value of the branching fraction obtained from the current analysis is presented in Table 5.4 and compared to the results of other experiments. The PDG average value is based on two measurements, CLEO and CBALL, and both collaborations do not consider the effect of the interference between signal decays and non-resonant background in their analysis. Our result that is based upon the constructive interference scenario is consistent with the CLEO and CBALL results within the errors but not for the destructive interference scenario. In the case of the constructive interference scenario, we have improved the errors relative to previous experiments.

5.11.2 M and Γ of the η_c

One the main motivation for the present analysis is measuring the basic properties of η_c like M and Γ since there is a large uncertainty in the value of these two parameters, as explained in Section 2.5. The obtained values for the constructive interference scenario for the M and Γ are $2.9849 \pm 0.0006 \pm 0.0006$ GeV/c^2 and $0.032 \pm 0.002 \pm 0.001$ GeV and for the destructive interference scenario are $2.9851 \pm 0.0001 \pm 0.0015$ GeV/c^2 and $0.031 \pm 0.002 \pm 0.002$ GeV, respectively.

The measured values of M and Γ of the η_c are compared in Figure 5.17 with all existing measurements. In this comparison, only BESIII, KEDR and our measurement considered the effect of the interference. The green circle shows our result for the M and Γ without considering the interference. According to this comparison, the interference affects the value of M but hardly the Γ. This may partly explain the discrepancy between the older experiments for the mass since they did not take into account the effect of interference in their analysis.

The first three red circles in Figure 5.17 are attributed to the BESIII collaboration. The first measurement is the result of this analysis, the second measurement is the result of $\psi' \to \gamma\eta_c$ and the third one is the result of $\psi' \to \pi^\circ h_c$, $h_c \to \gamma\eta_c$. These measurements are consistent with each other and are superior in accuracy compared to the results of other experiments.

5.11.3 Hyperfine splitting

The present measurement of the η_c mass allows us to determine the S-wave hyperfine splittings, which determine the spin-dependent part of the confinement potential. For this, we take the difference of the mass of the J/ψ, obtained from the PDG [48], with our mass measurement of η_c. S-wave hyperfine splittings of 112.0 ± 0.4 MeV/c^2 and 112.3 ± 0.5 MeV/c^2 are obtained corresponding to the cases in which we assume a constructive or destructive interference in our fit, respectively. Our results are compared in Table 5.5 with different theoretical predictions and with the average of published experimental results reported by the PDG [48]. Since only BELLE and BESIII have measured the η_c mass via e^+e^- annihilation, we only make comparisons with these two measurements.

Our result from the constructive (destructive) scenario is consistent within 2σ (5σ) with the latest lattice QCD result and consistent within 2σ (5σ) with the PDG value. Both experimental and theoretical errors have been reduced in the course of time and are now very competitive. This measurement is still limited by systematics. To improve on the systematic error of this measurement, some ideas are given in Section 7.4.

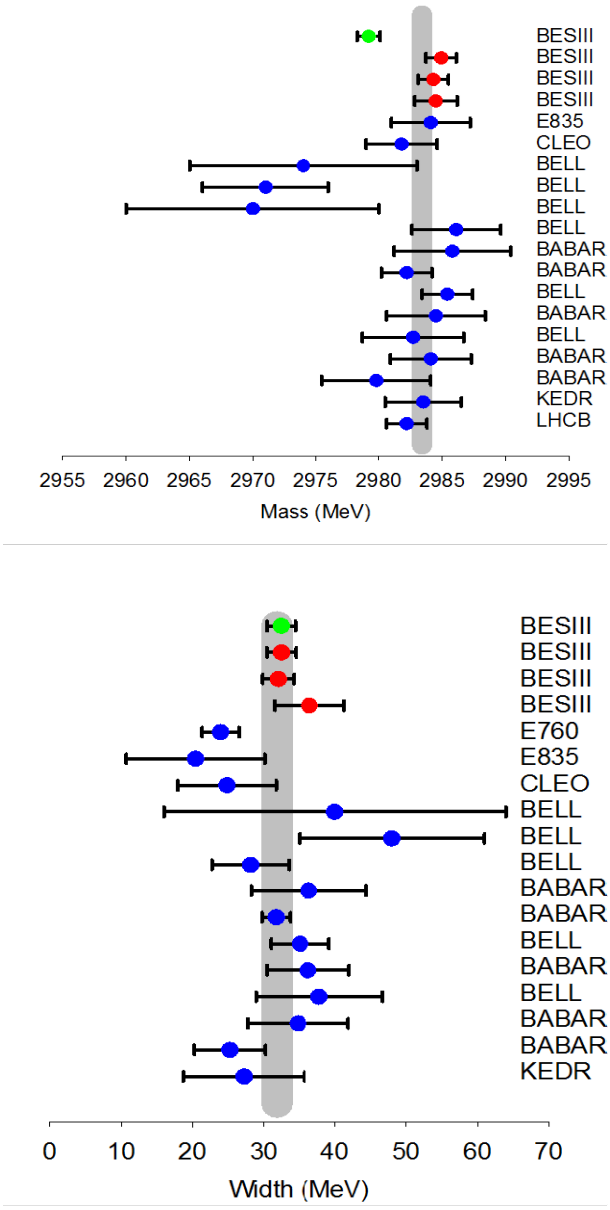

Figure 5.17: All the existing measurements for the mass (top) and width (bottom) of η_c. The green circle shows our result for the M and Γ without considering the interference. The first three red circles are attributed to the BESIII collaboration. The first measurement is the result of this analysis, the second measurement is the result of $\psi^{'} \to \gamma\eta_c$ and the third one is the result of $\psi^{'} \to \pi^{\circ}h_c$, $h_c \to \gamma\eta_c$. The error bars are the total error taken by summing in quadrature the statistical and systematic error and the grey band represents the world average.

Theoretical calculations of hyperfine splitting (MeV/c^2)	
Lattice QCD (2009) [55]	$116.0 \pm 7.4^{+2.6}_{-0.0}$
Lattice QCD (2012) [22]	$116.5 \pm 2.1 \pm 2.4$
Lattice QCD (2013) [15]	$116.2 \pm 1.4 \pm 2.8$
Lattice QCD (2015) [54]	113.8 ± 0.8
NR potential model [29]	108
GI [47]	113
Experimental measurements of hyperfine splitting (MeV/c^2)	
BELLE [25]	$111.5^{+2.5}_{-1.6}$
BESIII [26]	112.6 ± 0.9
PDG 2016 [48]	113.3 ± 0.7
Our measurement of hyperfine splitting (MeV/c^2)	
Constructive scenario	112.0 ± 0.4
Destructive scenario	112.3 ± 0.5

Table 5.5: Theoretical calculations and experimental measurements of the S-wave hyperfine splitting in charmonium. The details of the theoretical calculations and experimental measurements can be found in Table 2.7.1. All values are expressed in units of MeV/c^2. The presented error for the experimental measurements is the quadratic sum of statistical and systematic errors.

For the other calculations, it is difficult to compare the S-wave hyperfine splitting since they do not quote any uncertainty which makes it hard to judge. From this perspective, it is essential that theoretical predictions also estimate their errors to make their results useful to benchmark.

Chapter 6

Data Analysis of $\psi^{'} \to \gamma\eta_c$

In the previous chapter, the line shape of the η_c was studied through one of the exclusive decay modes of the M1 transition, $J/\psi \to \gamma\eta_c$ and the conclusion was that the interference with the non-resonant background plays an important role in measuring the properties of the η_c, such as its mass, width and its radiative transition rate. The question we address here is how to measure unambiguously the M1 radiative transition between a vector charmonium state and the ground state of the η_c without depending on the branching fractions of its decay. We try to evaluate the possibility to measure the M1 transition rate by performing an inclusive analysis of the process $\psi^{'} \to \gamma\eta_c$. An inclusive analysis refers to an analysis in which there is no bias placed on the specifics of the final-state of the η_c. In our inclusive study, we exploit the photon recoil mass spectrum RM_γ as defined in the previous chapter. We only focus on the transition of the excited vector state, $\psi^{'}$, since this involved a photon with sufficient energy that will be detectable with the calorimeter of BESIII. The $J/\psi \to \gamma\eta_c$ channel suffers from a very small photon energy which is hard to detect in an inclusive analysis.

To get the raw RM_γ, each photon candidate is considered as the radiative photon. The RM_γ spectrum is shown in Figure 6.1. Three peaks from the right of the spectrum are attributed to E1 transitions, $\psi^{'} \to \gamma\chi_{cJ=0,1,2}$. The two bumps in the range of 3.18 GeV/c^2 $< RM_\gamma <$ 3.36 GeV/c^2 are related to $\chi_{cJ=0,2} \to \gamma J/\psi$ transitions and a tiny bump around 2.98 GeV/c^2 is related to the M1 transition of interest, $\psi^{'} \to \gamma\eta_c$. A comparison of the sizes of the peaks related to E1 and M1 radiative transitions indicates that the M1 transition is strongly suppressed relative to E1 transitions. It is, therefore, not surprising that the M1 transition $\psi^{'} \to \gamma\eta_c$, is rather poorly understood below the open-charm threshold and its branching fraction is determined just based on two measurements from CLEO in 2004 and 2009 [48]. In addition, an improved precision on the branching fraction of the $\psi^{'} \to \gamma\eta_c$ is necessary because it is often used in the determination of the branching fractions of the η_c into various channels. It is to be noted that systematic errors dominate in the CLEO measurements which are the latest

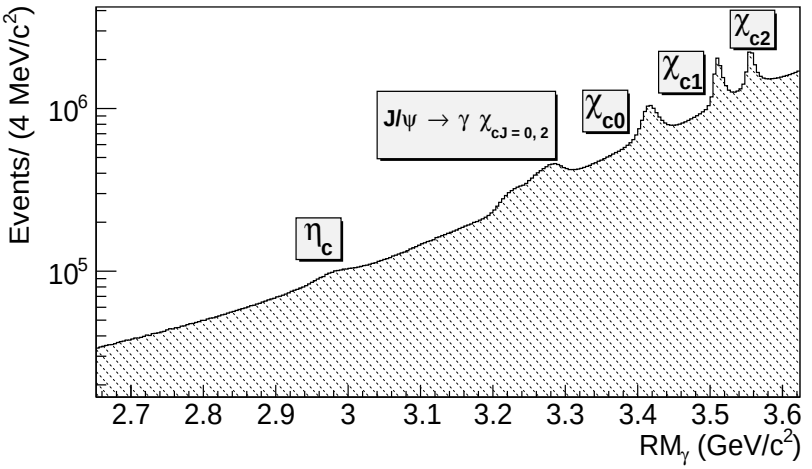

Figure 6.1: RM_γ spectrum for the transition $\psi' \to \gamma\eta_c$ obtained from data.

measurements of the branching fraction of $\psi' \to \gamma\eta_c$ transition. These results are shown in Table 6.1. To improve upon their results, it is necessary to reduce the systematic error. Since the statistical precision will not be the bottleneck, we decided to only use the 2009 ψ' dataset in this study.

The main aim of the analysis presented in this chapter is a branching fraction measurement. After optimizing the peak-to-background ratio, the number of signal events is obtained by fitting the RM_γ spectrum around the signal region. The fitting probability density function (PDF) includes the detector resolution, signal amplitude containing the mass and width of the η_c, a non-resonant background contribution, an interference phase accounting for the interference between signal and a non-resonant background and all the other sources of backgrounds, such as background related to ψ' decays, QED background and background attributed to the radiative decays of the η_c. In the fitting procedure, the mass and width of the η_c are fixed from the values obtained from the exclusive analysis result of $J/\psi \to \gamma\eta_c$. Then, using the number of signal events, the branching fraction is calculated. In this chapter the details of the analysis procedure that was used to get the branching fraction of the $\psi' \to \gamma\eta_c$ transition is presented.

Channel	Experiment	$\mathcal{B}(\psi^{'} \to \gamma\eta_c) \times 10^{-3}$
$\psi^{'} \to \gamma\eta_c$	CLEO04	$3.2 \pm 0.4 \pm 0.6$
$\psi^{'} \to \gamma\eta_c$	CLEO09	$4.32 \pm 0.16 \pm 0.6$
$\psi^{'} \to \gamma\eta_c$	PDG	3.4 ± 0.5

Table 6.1: $\psi^{'} \to \gamma\eta_c$ branching fraction from CLEO and average value from PDG 2016 [48]. The first error is statistical and the second error is systematical.

6.1 Branching fraction

The present analysis is aimed at measuring the branching fraction of $\psi^{'} \to \gamma\eta_c$. The branching fraction, $\mathcal{B}$, is calculated using the following equation:

$$\mathcal{B}_{(\psi' \to \gamma\eta_c)} = \frac{N_{\psi' \to \gamma\eta_c}}{\epsilon_{\psi' \to \gamma\eta_c} \times N_{\psi'}}, \tag{6.1}$$

where $\mathcal{B}_{(\psi' \to \gamma\eta_c)}$ is the branching fraction of $\psi^{'} \to \gamma\eta_c$, $N_{\psi' \to \gamma\eta_c}$ is the number of events in the signal region, 2.74 GeV/c^2 $< RM_\gamma <$ 3.16 GeV/c^2, which is obtained from the fit, $\epsilon_{\psi' \to \gamma\eta_c}$ is the efficiency which will be determined from Monte Carlo (MC) simulation and $N_{\psi'}$ is the total number of $\psi^{'}$ events. The fit strategy to extract the number of signal events and a description of the MC study that was performed to obtain the efficiency are discussed in Sections 6.2 and 6.5, respectively.

6.2 Overall strategy of fitting

By considering the non-resonant background and interference effect in the total fit, the fitting PDF as a function of mass (m) reads:

$$F(m) = \Big(E_\gamma^7 \times f_d(E_\gamma) \times \left|BW(m) \times e^{i\phi} + \alpha N(m)\right|^2 \otimes DR\Big) \otimes G + B(m), \tag{6.2}$$

where α is the strength of the non-resonant component, $N(m)$ is the non-resonant amplitude, $\otimes$ is the convolution symbol, G stands for gaussian and ϕ reflects the interference phase between signal and non-resonant background. $B(m)$ contains background from the $\psi^{'}$ decays, background from QED processes and background from η_c radiative decays. In the rest of the chapter, these three types of background are called $\psi^{'}$ background, continuum background and η_c background. The other components of the fit function are described below.

Signal:

The signal is described by a relativistic Breit-Wigner (BW) distribution modified by a factor E_γ^7. This factor is needed to get proper matrix elements but leads to a diverging tail at lower mass. To damp the E_γ^7 factor, an additional factor is added, which is called the damping factor. The damping factor, $f_d(E_\gamma)$, in our fit is taken from KEDR for a similar process [45]:

$$f_d(E_\gamma) = \frac{E_0^2}{E_\gamma E_0 + (E_\gamma - E_0)^2}, \tag{6.3}$$

where E_γ is the energy of the radiative photon and E_0 is the photon energy at the η_c nominal mass, m_{η_c}:

$$E_\gamma = \frac{m_{\psi'}^2 - m^2}{2m_{\psi'}}, \tag{6.4}$$

$$E_0 = \frac{m_{\psi'}^2 - m_{\eta_c}^2}{2m_{\psi'}}, \tag{6.5}$$

where $m_{\psi'}$ is the nominal ψ' mass, 3.686 GeV/c^2. The signal is convoluted with the Detector Response (DR) which is explained in more details in Section 6.5. The signal which is convoluted by DR is convoluted again by an additional Gaussian to take into account the difference in the DR between data and MC. The BW distribution as a function of mass is introduced as:

$$BW(m) = \frac{1}{(m^2 - m_{\eta_c}^2) + i m_{\eta_c}\Gamma}, \tag{6.6}$$

where m_{η_c} and Γ are the mass and width of η_c, respectively. The mass and width values are fixed from the results obtained from the exclusive decay mode of $J/\psi \to \gamma\eta_c$ which is reported in Chapter 5.

Background:

In the fitting procedure, we deal with four different sources of background: ψ' background, continuum background, η_c background and non-resonant background which are described below.

– $\psi^{'}$ background

This type of background is related to all the $\psi^{'}$ decays except $\psi^{'} \to \gamma\eta_c$. The line shape of this source of background is obtained from the inclusive MC sample which is explained in more detail in sub-section 6.5.3.

– Continuum background

This type of background is related to the $e^+e^- \to \gamma\gamma$ continuum process, which is a background contribution from QED. A 42 pb^{-1} continuum data sample, taken at a center-of-mass energy of $\sqrt{s} = 3.650$ GeV, is used to account for non-$\psi^{'}$ background. The integrated luminosity of the continuum data sample is about 25% of the integrated luminosity of the $\psi^{'}$ data sample. The continuum background is normalized by the luminosity.

– η_c background:

This type of background is related to the radiative transitions of η_c, $\eta_c \to \gamma X_i$, which would be part of the signal. Exclusive MC samples are used to obtain the contribution of this source of background which is explained in more detail in sub-section 6.5.3.

– Non-resonant background:

The signal can interfere with a non-resonant background. This type of background, $\psi^{'} \to \gamma X_i$ has the same final-state as signal events without η_c as an intermediate state. The interference of the signal with a non-resonant background is one of the elements to be checked in this analysis. For the first time, a non-resonant component was included in the fit of the η_c signal line shape for six exclusive decay modes of $\psi^{'} \to \gamma\eta_c$ in the BESIII analysis [26]. In all six exclusive modes, a flat distribution is considered for this type of non-resonant background and a reasonable fit is obtained. Furthermore, the interference phases appear to be all the same for various channels. Also in our analysis we considered an interference contribution. Similar to the exclusive analysis, we decided to take a flat distribution for the non-resonant background.

6.3 Data sample and MC simulation

To determine the η_c line shape in the $\psi' \to \gamma\eta_c$ transition for our data sample, exclusive and inclusive MC studies are required. In the following, we describe the data set and the MC samples that were used for this analysis.

6.3.1 Data set

The 2009 ψ' event sample was accumulated by BESIII from March 7 to April 4, 2009. The total number of ψ' events is $(106.41 \pm 0.86) \times 10^8$ and the integrated luminosity is 156.4 pb^{-1}. A 44 pb^{-1} data continuum sample, taken at a center-of-mass energy of 3.65 GeV is used to determine the non-ψ' background under the ψ' peak, i.e. from QED processes and cosmic rays. The BOSS version that was used to process and analyze the data is BOSS6.6.4.

6.3.2 MC samples

For the study of potential background sources and also to get the line shape of backgrounds in the final fit, 106×10^6 inclusive MC events are used. The events are generated with the generator EVTGEN [125], which simulates the decay of resonances with the known branching fractions from PDG. Decay channels with unknown branching fractions are simulated with the Lundcharm model [126]. The BOSS version that was used to generate and analyze the inclusive MC data is BOSS6.6.4 p01. Furthermore, the inclusive MC study is done to confirm that the fitting procedure is satisfactory and is reliable to extract the number of signal events for the data sample. In addition to the inclusive MC sample, exclusive MC samples are used to model the signal line shape and to determine the detection efficiency. The JPE decay model is used for the transition $\psi' \to \gamma\eta_c$ to generate the signal events. According to the PDF that is used to fit the observed line shape (see Section 6.2), to get the signal line shape, the BW distribution is convoluted with the DR. To obtain the DR, a clean data sample is generated by an exclusive MC simulation. To validate the simulated detector response, data originating from the radiative transition to the χ_{c1} state is used as a control sample and the χ_{c1} line shape is obtained from the exclusive MC sample for $\psi' \to \gamma\chi_{c1}$ which is generated with the P2GC1 model. For more details of decay models see section 4.2.1. Moreover, we carried out a consistency check of the analysis procedure by performing a so-called input-output check using MC generated data of the reactions $\psi' \to \gamma\chi_{c0}$ and $\psi' \to \gamma\eta_c$. This method is explained in more detail in sub-section 6.6.2.

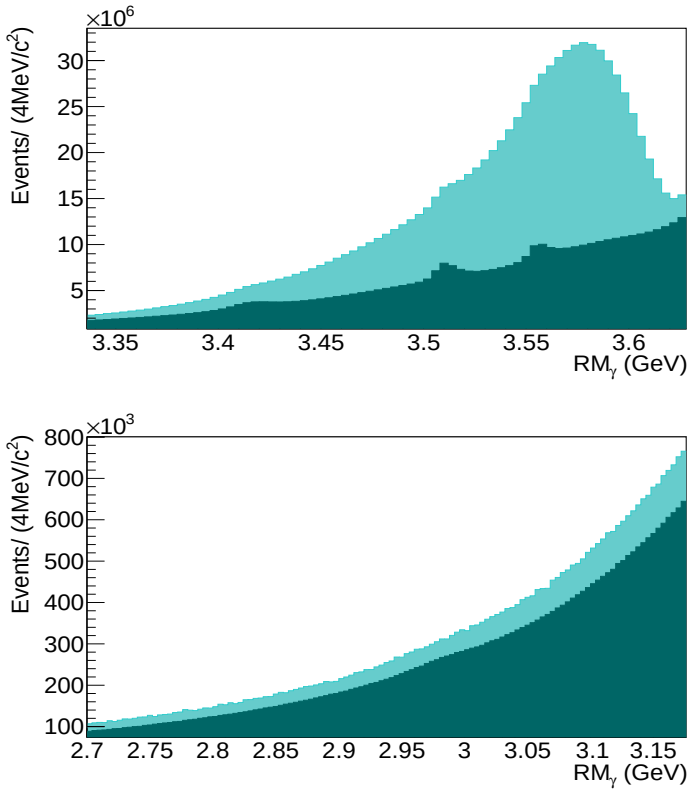

Figure 6.2: Comparison of $RM\gamma$ distributions before (light green distribution) and after (dark green distribution) applying the $N_{ch} > 0$ cut, Top: for the E1 radiative transitions, $\psi' \to \gamma\chi_{cJ=0,1,2}$, Bottom: for the M1 radiative transition $\psi' \to \gamma\eta_c$, obtained from data.

In the following, we describe the event selection that was used to optimize the signal-to-background ratio.

6.4 Event selection for $\psi' \to \gamma\eta_c$

Beyond the general selection criteria which are explained in Section 4.6, we applied additional constraints for the identification of the radiative photon candidates. In general we kept the event selection fairly loose in order to minimize the systematic error. In

the following, the data represent results for which the continuum background has been subtracted.

• Number of charged tracks (N_{ch})

The number of charged tracks, N_{ch}, is required to be at least one. Although this cut imposes a bias on the data, without this requirement there is simply too much background. The RM_γ spectrum is shown in the top panel of Figure 6.2 around the region corresponding to the E1 radiative transitions and in the bottom panel for the M1 radiative transition. In every plot, two distributions are compared, with and without requiring $N_{ch} > 0$. The light green spectrum represents the RM_γ distribution without requiring that $N_{ch} > 0$ and dark green with the requirement $N_{ch} > 0$. Figure 6.2 demonstrates that applying this cut helps to improve the signal-to-background ratio especially for the control samples, $\psi' \to \gamma\chi_{cj=0,1,2}$.

The distribution of charged track multiplicity per event is shown in the left panel of Figure 6.3 for the data and for the inclusive MC sample. Dots represent data and the filled histogram represents the result of the inclusive MC. The difference between data and inclusive MC results indicates that there is a remaining non-ψ' background which strongly contributes to the $N_{ch} = 1$ events. To remove the non-ψ' background related to $N_{ch} = 1$, the number of positive and negative charged tracks per event is checked and the result is shown in Figure 6.4. For the further analysis, the number of positive charged tracks per event, N_{Pch}, and the number of negative charged tracks per event, N_{Nch}, are required to be at least one. These cuts are used to get rid of low-energy positive and negative charged tracks which do not reach the EMC and to reduce the non-ψ' background.

• Number of photons (N_{ph})

The photon multiplicity distribution per event is shown in the right panel of Figure 6.3. Dots represent data and filled histogram represents the result of the inclusive MC. The number of photons, N_{ph}, is required to be at least one. There is mismatch between data and inclusive MC which can indicate that the inclusive MC model needs improvement or else it can be attributed to the existence of non-ψ' background. This point will be discussed in more detail in sub-section 6.6.1.

• Barrel photon requirement

For the further analysis, only photons that hit the barrel EMC are required. We

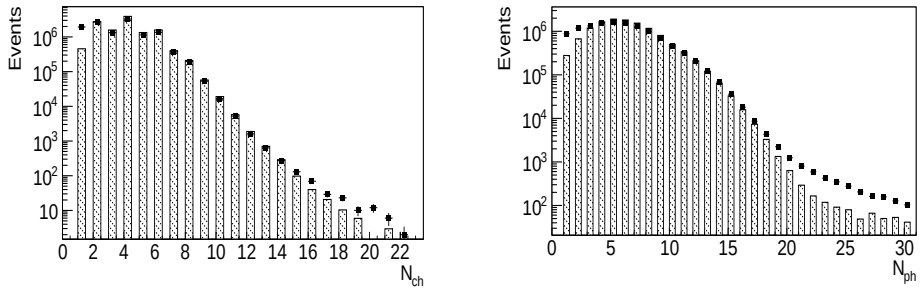

Figure 6.3: Left: The distribution of charged track multiplicity, N_{ch}, per event, Right: The distribution of photon multiplicity, N_{ph}, per event. Dots represent data and filled histogram represents the result of inclusive MC.

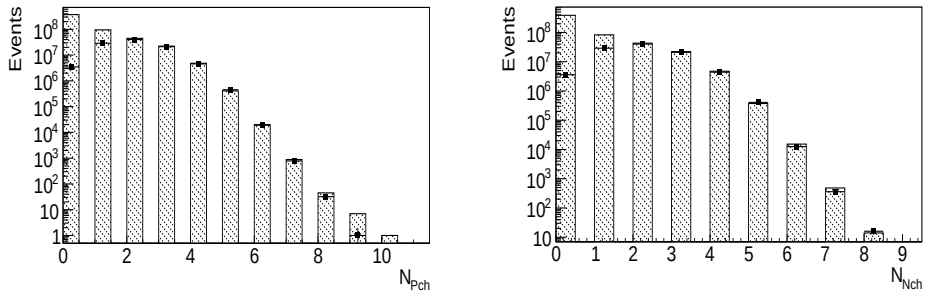

Figure 6.4: Left: The distribution of positive charged track multiplicity, N_{Pch}, per event, Right: The distribution of negative charged track multiplicity, N_{Nch}, per event. Dots represent data and the filled histogram represents the result of inclusive MC.

call these barrel photons and they are defined as photons that are detected within $40^\circ < \theta < 140^\circ$ and photons outside this region are defined as endcap photons. The requirement of barrel photons is used because endcap photons stem mostly from QED processes, moreover, the energy resolution for photons hitting the barrel is much better than that of photons hitting the endcaps.

• Reducing $\pi^+\pi^- J/\psi$ events

Since we require $N_{Pch} > 0$ and $N_{Nch} > 0$, we have the option to eliminate photons from J/ψ decays of the channel $\psi' \to \pi^+\pi^- J/\psi$. This reaction can be identified by studying the recoil mass distribution of the $\pi^+\pi^-$ system, $RM_{\pi^+\pi^-}$. The $RM_{\pi^+\pi^-}$

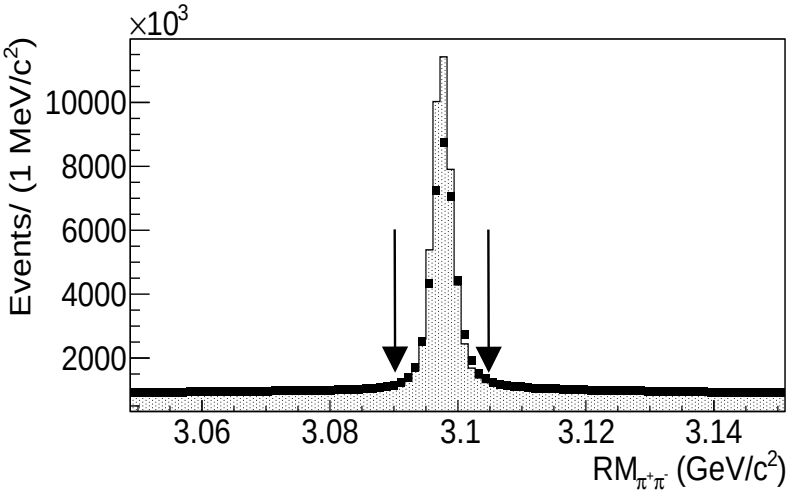

Figure 6.5: $RM_{\pi^+\pi^-}$ distribution obtained from data. The arrows in the plot represent the cut region to remove the J/ψ events as one of the sources of background in this analysis.

distribution is shown in Figure 6.5. The obtained result from data (dots) is compared with the result obtained from inclusive MC (filled histogram) and the results are in reasonable agreement. There is a clear peak around the J/ψ mass which is one of the sources of background for this analysis. J/ψ events are rejected by requiring 3.09 GeV/c^2 $< RM_{\pi^+\pi^-} <$ 3.11 GeV/c^2.

• Reducing non-ψ' events

Figure 6.6 shows the two-dimensional histogram of p (GeV/c) versus the E/p (c) in the signal region 2.74 GeV/c^2 $< RM_\gamma <$ 3.16 GeV/c^2 obtained from the data. p is the maximum momentum of all the charged tracks in an event, and E is the deposited energy in the EMC attributed to the charged tracks with the highest momentum. Since we deal with e^+e^- scattering, one expects to see the correlation at half of the beam energy (beam energy is 3.686 GeV/c^2) since we expect a contribution from Bhabha scattering. According to the E/p method, the E/p value for electrons (positrons) should be around one [1]. The blob in Figure 6.6 indicates the existence of Bhabha events which can be considered to be a source of background. To remove the Bhabha events, we applied the cuts $0.72c < E/p < 1.12c$ and 0.8 GeV/c $< p <$ 2.3 GeV/c.

[1] For more details of E/p method, see subsection 4.4.4.

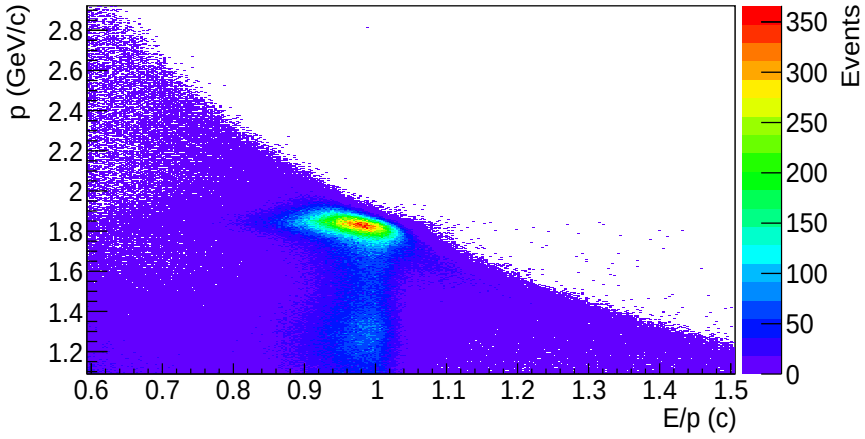

Figure 6.6: p (GeV/c) distribution versus the E/p (c) in the signal region, 2.74 GeV/c^2 < RM_γ < 3.16 GeV/c^2 for the channel of interest, $\psi' \to \gamma\eta_c$, obtained from data. The blob indicates the existence of Bhabha events which can be considered to be one of the sources of background.

• Reducing π° background

The invariant-mass of all possible combinations of two photons for each event is shown in Figure 6.7. Dots represent data and filled histograms represent inclusive MC results. There is a clear peak around the π° mass (0.139 GeV/c^2) and a peak around the η mass (0.547 GeV/c^2). We have studied the effect of applying a cut on photons originating from π° and η decays on the RM_γ spectrum in the signal region. For the further analysis, only the π° background cut is kept since the η background just reduces the efficiency without improving the signal-to-background ratio. Photons which are not in the mass window, 0.120 GeV/c^2 < $M_{\gamma\gamma}$ < 0.145 GeV/c^2, attributed to π° decays, are kept. To check the performance of each cut, the signal-to-background ratio, $\frac{S}{B}$, is calculated from data. S (B) denotes the number of events in the signal and background, respectively. To perform a fit and to count the signal and background events, the range 2.74 GeV/c^2 < RM_γ < 3.16 GeV/c^2 is selected. Our study shows that the $\frac{S}{B}$ ratio hardly improves when applying the various cuts, which implies that the cuts have hardly any noticeable effect on the statistical significance. However, we do find a clear improvement when considering the systematic uncertainty. Except for the $\pi^+\pi^- J/\psi$ exclusion window, all other cuts reduce the systematic error and are, therefore, kept as a condition for the further analysis. To give an impression about the role of the cuts in

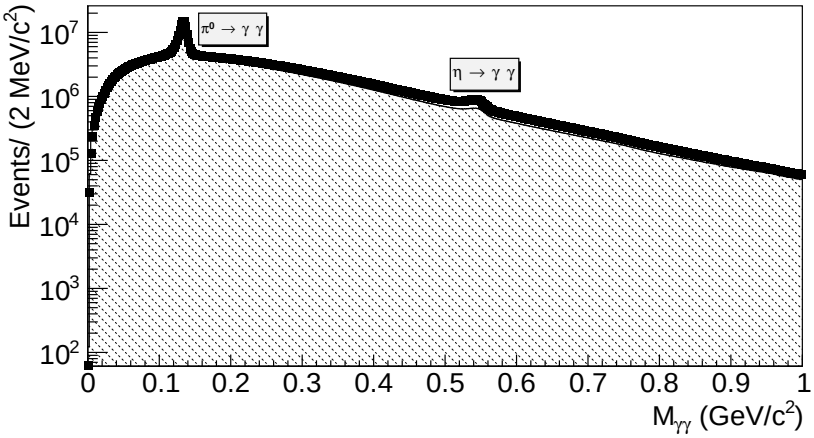

Figure 6.7: Invariant-mass distribution of two photons, $M_{\gamma\gamma}$ which represent a clear peak around the π^0 mass, 0.139 GeV/c^2, and a peak around the η mass, 0.547 GeV/c^2. Dots represent data and the filled histogram represents inclusive MC result.

reducing the systematic error, we studied the effect of the π°-veto cut. It turns out that the systematic error can be reduced by 5-8%, depending on the interference scenario, when applying the π°-veto condition.

The RM_γ distribution, with the cumulative selection requirements listed above, is shown in Figure 6.8 as obtained from the data. After reducing considerably the most probable backgrounds, the efficiency of various cuts, the DR and the background line shape are obtained by using MC studies.

6.5 MC studies

In this section, we explain the details of the simulation which was used to obtain the detection efficiencies, the detector response and background contributions.

6.5.1 Detection efficiency

The total detection efficiency, ϵ, is one of the parameters that is needed to calculate the branching fraction. The exclusive MC sample for the transition, $\psi' \to \gamma\eta_c$, $\eta_c \to$ anything, is used to calculate the detection efficiency for each cut. The efficiency

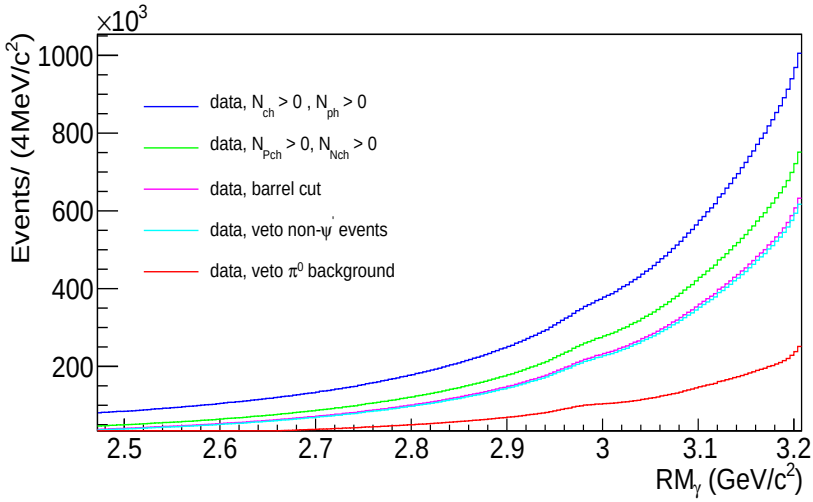

Figure 6.8: Comparison of RM_γ distribution for data after applying the cuts which are explained in section 6.4.

Selection criteria	Efficiency (ϵ)
$N_{ch} > 0$, $N_\gamma > 0$	0.98
$N_{Pch} > 0, N_{Nch} > 0$	0.86
Barrel cut	0.69
Reducing non-$\psi^{'}$ events	0.68
Reducing π° background	0.47

Table 6.2: Efficiency table for $\psi^{'} \rightarrow \gamma\eta_c$, $\eta_c \rightarrow$ anything obtained from an exclusive MC sample.

is defined as the ratio of detected and reconstructed events in the region of interest, (2.74 GeV$/c^2 < RM_\gamma < 3.16$ GeV$/c^2$), to the number of generated events in the exclusive MC sample. As an example, the result of RM_γ for $\psi^{'} \rightarrow \gamma\eta_c$, $\eta_c \rightarrow$ anything after applying all the criteria which are explained in Section 6.4, is shown in Figure 6.9. The signal line shape is modeled with a Crystal-ball function and the background is modeled with an exponential function. The input values for the mass and width of η_c are taken from obtained results of the exclusive analysis of $J/\psi \rightarrow \gamma\eta_c$. The selection requirements and the detection efficiency for each requirement are summarized in Table 6.2. The total detection efficiency for the further analysis is 46.6%.

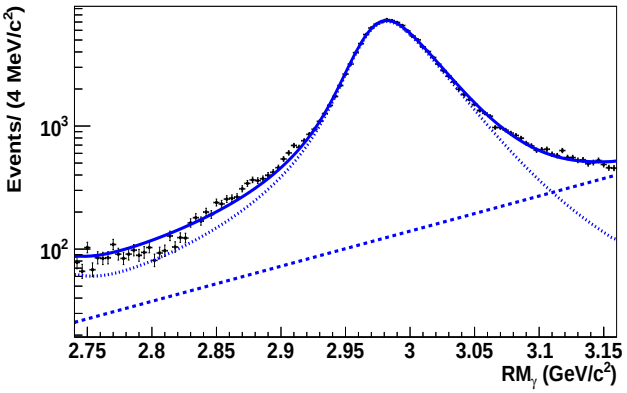

Figure 6.9: Exclusive MC result for $\psi' \to \gamma\eta_c$, $\eta_c \to$ anything. The signal is modeled with a Crystal-Ball function and the background is modeled with an exponential function.

6.5.2 Detector response

To get the right model for the detector response in this analysis, mono-energetic photons are generated and the result is represented in the top panel of Figure 6.10. To describe this spectrum, a fit is made using a Chebyshev function representing our model for the DR together with an exponential to model the background.

To validate our MC study, we look at the χ_{c1} state which has a small natural width of $\Gamma = 0.8$ MeV. The χ_{c1} state is used since it is one of the narrowest states in the RM_γ spectrum, as illustrated in Figure 6.1. In addition, the χ_{c1} state is populated via an E1 transition, $\psi' \to \gamma\chi_{c1}$, which is one of the very well understood transitions below the open-charm threshold. To describe the signal, the DR obtained from exclusive MC is fixed in the fit procedure and to describe the background two exponential functions are used. The fit result is shown in the bottom panel of Figure 6.10. The $\chi^2/n.d.f$ value for this fit is 2.75 which indicates that the fit result is reasonable. Therefore the MC study is a reliable method to obtain the DR.

6.5.3 Background line shapes

Various sources of background will be discussed in this sub-section. Exclusive and inclusive MC samples are used to get the background line shapes.

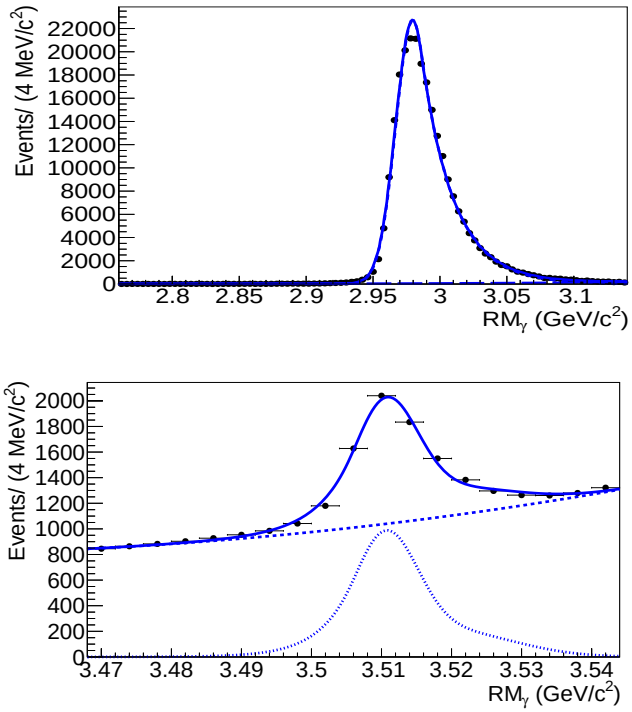

Figure 6.10: Top: The DR is obtained by performing the fit for exclusive MC of mono-energetic photons, Bottom: Validation of the DR by looking at the χ_{c1} state through the $\psi^{'} \to \gamma\chi_{c1}$ transition for the data. The data are described by a signal response function (dotted line) obtained from an exclusive MC simulation in which the DR response and the natural width of the χ_{c1} is accounted for, combined with a double exponential function describing the background (dashed line).

6.5.3.1 $\psi^{'}$ background

To model the line shape of background from $\psi^{'}$ decays other than the M1 transition, we exploited the inclusive MC data sample. For this, all the decay modes of $\psi^{'}$ which have at least one photon in the final-state, $\psi^{'} \to \gamma X_i$, are kept except those related to the $\psi^{'} \to \gamma\eta_c$ transition. The left panel of Figure 6.11 shows the line shape of the $\psi^{'}$ background. A second-order polynomial is used to describe the line shape. In the final fit, the $\psi^{'}$ background line shape is fixed and its magnitude is kept as a free parameter.

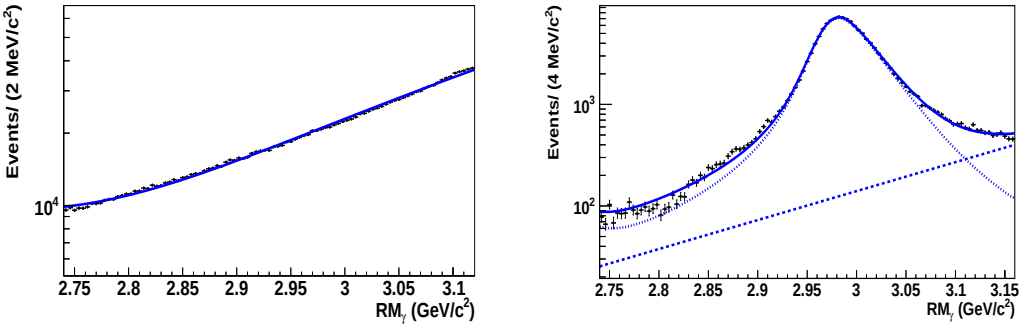

Figure 6.11: Left: ψ' background line shape which is obtained from inclusive MC sample. The second-order polynomial is used to describe the line shape. Right: Exclusive MC result of $\psi' \to \gamma\eta_c$, $\eta_c \to$ anything. The signal line shape is modeled with a Crystal-ball function and background is modeled with an exponential function.

6.5.3.2 η_c background

This type of background is related to the radiative transition of $\psi' \to \gamma\eta_c$, whereby the η_c eventually decays into photons that could end up in the signal region as part of the background. Exclusive MC decay of $\psi' \to \gamma\eta_c$, $\eta_c \to$ anything is used to obtain the contribution of this source of background. The right panel of Figure 6.11 shows this type of background. The signal line shape is modeled with a Crystal-Ball function and background is modeled with an exponential function. The line shape and the ratio between signal and background are fixed in the final fit but the magnitude is kept as a free parameter. For this type of background, we depend upon the modeling of the generator, but since the size of background is small, it will hardly introduce a significant systematic error on our analysis.

6.6 MC validation

Since the efficiency and background line shapes depend on the predictive power of the MC simulation, it is important to compare the inclusive MC and data. In the following, the continuum background has been subtracted from data. In sub-section 6.6.1, spectra of some key observables are compared with results of the inclusive MC data sample and in sub-section 6.6.2, the fit procedure is validated using MC studies and a control channel.

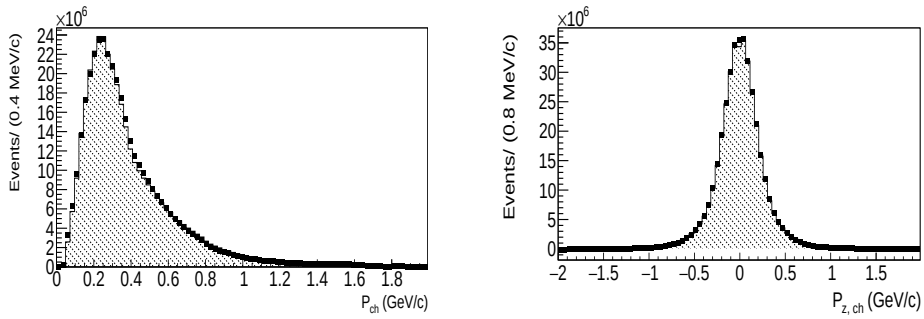

Figure 6.12: Left: p_{ch}(GeV/c) distribution and Right: $p_{z,\ ch}$(GeV/c) distribution. Dots represent data and filled histograms represent the result from inclusive MC.

6.6.1 Data versus MC

Figure 6.12 shows the reconstructed momentum distribution, p_{ch}, for charged tracks, and the distribution of the z component of its momentum, $p_{z,\ ch}$. The polar angle and azimuthal angle between the photon and beam direction, $\theta_{(\gamma,\mathrm{beam})}$ and $\phi_{(\gamma,\mathrm{beam})}$, respectively, are shown in the left and right panel of Figure 6.13. In all cases, there is a perfect agreement between data and MC. The agreement between data and inclusive MC for some of the photon distributions is less satisfactory, such as the photon multiplicity, N_{ph}, and two-photon invariant-mass, $M_{\gamma\gamma}$ as discussed in Section 6.4. In order to correct for the observed deficiencies, MC events will be corrected by a weight determined according to the measured N_{π^0} distribution. For events with N_{π^0} corresponding to bin i of the N_{π^0} distribution, the weight is obtained from $wt_{\pi^0} = \frac{N_{\pi^0}^{data}}{N_{\pi^0}^{MC}}$. Figure 6.14 shows the corrected distributions which can be compared to the uncorrected distributions given in Figure 6.3 and Figure 6.7. Note that the N_{ph} and $M_{\gamma\gamma}$ distributions agree well with data.

6.6.2 Input-output check

The so-called input-output check is a method to test the analysis technique using the inclusive MC sample. In the input-output check, all the selection criteria which are applied to the data are applied to the inclusive MC sample as well and the final results are compared to the input values. The aim of the input-output check for this analysis is to test the fitting procedure and extracting the number of events in the signal region. The branching fraction is calculated by using equation 6.1 and the obtained result is

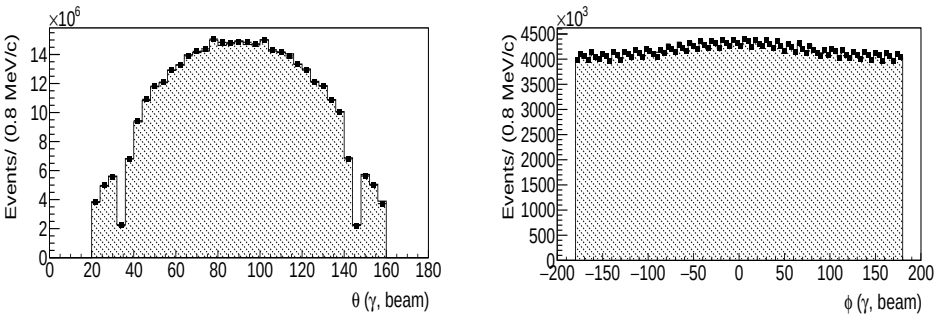

Figure 6.13: Left: Polar angle distribution. The polar angle coverage are $|\cos\theta| < 0.82$ for the barrel and $0.85 < |\cos\theta| < 0.95$ for the endcaps. Two holes are related to small dead gaps between the barrel and two endcaps. In our analysis only photons that hit the barrel EMC are required. Right: Azimuthal angle distribution between photon and the beam direction.

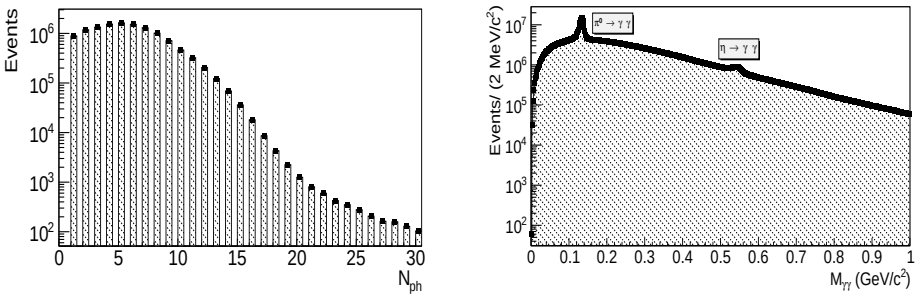

Figure 6.14: The corrected photon distributions with the weight, $wt_{\pi^0} = \frac{N^{data}_{\pi^0}}{N^{MC}_{\pi^0}}$, Left: For the photon multiplicity, Right: for the $M_{\gamma\gamma}$ distribution. For more details see subsection 6.6.1.

compared with the values for the branching fraction that were used as input to the inclusive MC study. For the inclusive MC, all the decays of the ψ' are generated according to the branching fractions published by the PDG [48].

First, the fitting method is tested on the E1 radiative transition, $\psi' \to \gamma\chi_{c0}$. The result of the fit is shown in the top panel of Figure 6.15. A BW distribution is used to model the signal since the other corrections, like the damping factor which is explained in Section 6.2, are part of the inclusive MC sample. The background is modeled by adding two different sources of backgrounds, the ψ' and η_c background. These types of backgrounds are explained in Section 6.2 in more detail. The other parameter to

Channel	Efficiency	Input value	Output value
$\psi^{'} \rightarrow \gamma\chi_{c0}$	35%	0.094	0.095 $\pm$ 0.001
$\psi^{'} \rightarrow \gamma\eta_c$	47%	0.003	0.00296 $\pm$ 0.00003

Table 6.3: The summary of the input-output check for the E1 transition, $\psi^{'} \rightarrow \gamma\chi_{c0}$, and the M1 transition, $\psi^{'} \rightarrow \gamma\eta_c$. The error in the output value is only statistical.

calculate the branching fraction is the efficiency which is obtained from an analysis of the exclusive MC sample, $\psi^{'} \rightarrow \gamma\chi_{c0}$. The fit result is shown in the bottom panel of Figure 6.15. A BW distribution is used to describe the signal and one exponential is used to describe the background line shape. The efficiency was found to be 35%. A branching fraction of 0.095 $\pm$ 0.001 was obtained from the fit, which can be compared to the input value of 0.094.

As a next step, our channel of interest, $\psi^{'} \rightarrow \gamma\eta_c$ is checked. The fit based on equation 6.2 is used to perform the fit and to extract the number of signal events. The fit result is presented in Figure 6.16. The efficiency for this channel was found to be 47% as explained in sub-section 6.5.1. A branching fraction of 0.00296 $\pm$ 0.00003 is obtained for an input value of 0.003. The summary of the results of the input-output check is given in Table 6.3. The output values are consistent with the input values within the statistical error. We are not sensitive to the systematic error since the background is taken from the inclusive MC itself.

After performing the input-output check, we try to do one more test on the E1 radiative transition, $\psi^{'} \rightarrow \gamma\chi_{c0}$, but this time with the data sample instead of the inclusive MC sample. The same fitting procedure as was used for the inclusive MC study has been applied for the data. To take into consideration a small deviation of the detector resolution between data and MC, our BW distribution has been convoluted with a gaussian function with a resolution of 1 MeV. The $\chi^2/n.d.f$ value of the fit is 5.2 and a branching fraction of $\psi^{'} \rightarrow \gamma\chi_{c0}$ was found to be 0.0991 $\pm$ 0.0001 $\pm$ 0.0031. The first error is statistical and the second one is systematic [2]. The PDG value for this transition is 0.0999 $\pm$ 0.0027 [48]. Our result is consistent with the PDG value within the error.

As a result, we can conclude that the fitting procedure is satisfactory and can be used for the extraction of the signal events for our channel of interest, $\psi^{'} \rightarrow \gamma\eta_c$.

[2]The systematic error is taken from the BESIII analysis related to E1 radiative transitions of $\psi^{'}$ which is reported in [49].

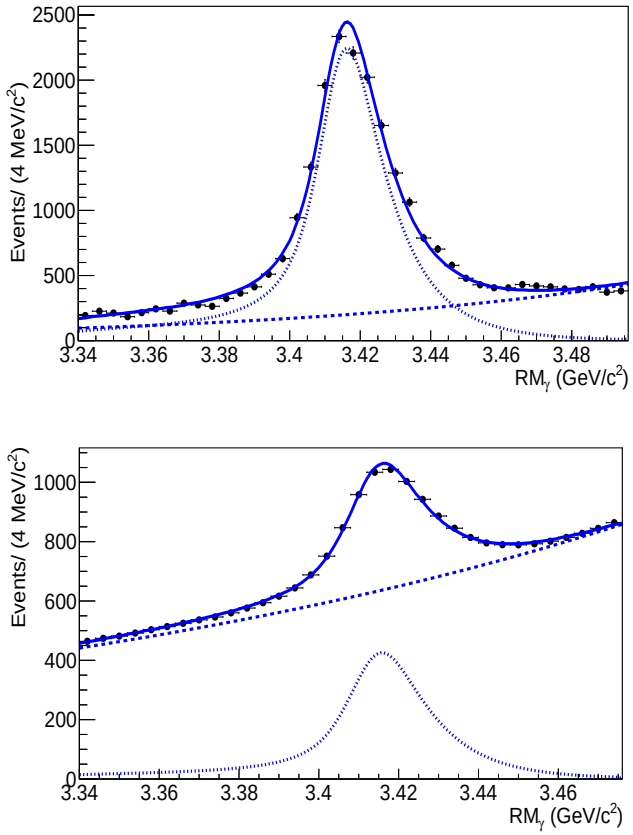

Figure 6.15: Fit result for the $\psi' \to \gamma\chi_{c0}$ transition, Top: For exclusive MC, Bottom: For inclusive MC. The signal (background) line shape is represented by the dotted (dashed) curve and the total line shape of signal plus background is represented by the solid curve. More details of the fitting procedure are given in sub-section 6.6.2.

6.7 Results

As was concluded in sub-section 6.6.2, the fit procedure described in Section 6.2 is a reliable way to extract the number of signal events. The total line shape including signal and background is represented by a PDF given by equation 6.2 and the results are shown in Figure 6.17. Two assumptions are considered in this fit. The first assumption is related to the line shape of the interfering non-resonant background which is assumed

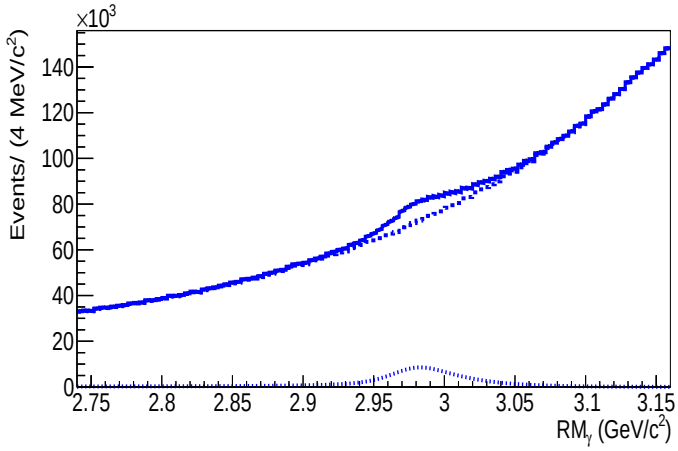

Figure 6.16: The fit result for the $\psi^{'} \rightarrow \gamma\eta_c$ transition for the inclusive MC data. More details of the fitting procedure are given in the text.

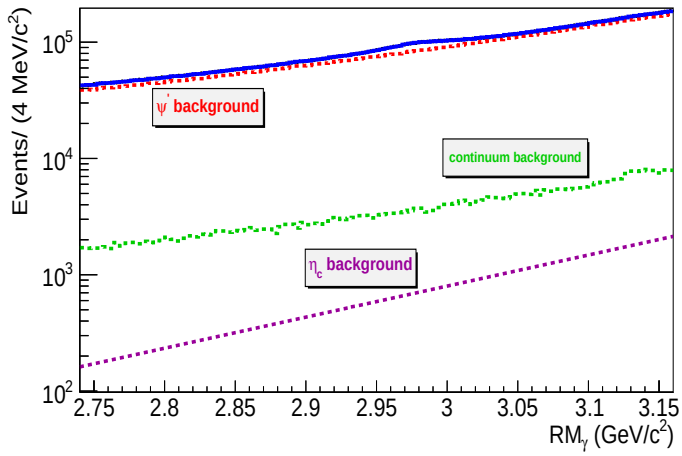

Figure 6.17: The fit result for the $\psi^{'} \rightarrow \gamma\eta_c$ transition obtained from data. The total line shape of signal plus background is represented by the blue curve. Each of the three different components of background are represented as well. The red curve shows the $\psi^{'}$ background, the green curve shows the continuum background and the purple curve shows the η_c background.

to be a flat distribution. This assumption works reasonably well for the analysis based on the six exclusive decay modes of the ψ' as explained in reference [26]. The second assumption is related to the interference phase between the signal and the non-resonant background. According to the conclusion obtained from analysis of six exclusive decay modes of the ψ' [26], the interference phase values are the same in all six exclusive decay modes of the ψ'. Based on this observation, we decided to use the same phase values in our case. A phase of $\phi = 2.40 \pm 0.07 \pm 0.47$ rad is taken for the constructive interference and $\phi = 4.19 \pm 0.03 \pm 0.47$ rad for the destructive interference. The mass and width of η_c are fixed from the obtained values of the exclusive analysis of $J/\psi \to \gamma\eta_c$ which is reported in Chapter 5. The total line shape of the signal plus background is represented by the blue curve in Figure 6.17. The three different components of the background are represented in Figure 6.17 as well. The red curve shows the ψ' background, the green curve shows the continuum background and the purple curve shows the η_c background.

The quality of the fit for the two different situations, constructive and destructive interference, are shown in Figure 6.18 by representing the pull distribution. The pull distribution is defined as a subtraction of every data point from the fitted PDF divided by the statistical error of every data point. The top panel of Figure 6.18 shows the pull distribution for the constructive interference procedure and bottom panel shows the pull distribution for the destructive interference procedure. The fit results have the same fit quality in both situations. It is, therefore, impossible to discriminate between both scenarios.

The different components of the signal and the interferences are presented in Figure 6.19. The top panel shows the constructive interference and bottom panel the destructive interference. The black curve shows the signal which is obtained from the fit result containing three different components, signal (red curve), non-resonant background (orange line) and the interference contribution between signal and non-resonant background (cyan curve). The fit yields 130741 ± 361 events for the signal contribution for the constructive case and 256354 ± 515 events for the destructive case.

6.8 Systematic error

The systematic errors are due to deficiencies in the MC simulation that influence the efficiencies of the selection requirements. In other words, the systematic errors arise from the selection requirements, the fitting procedure, considering the interference between signal and non-resonant background, the uncertainty related to the fixed parameters, the photon reconstruction and the uncertainty in the number of ψ' events which are

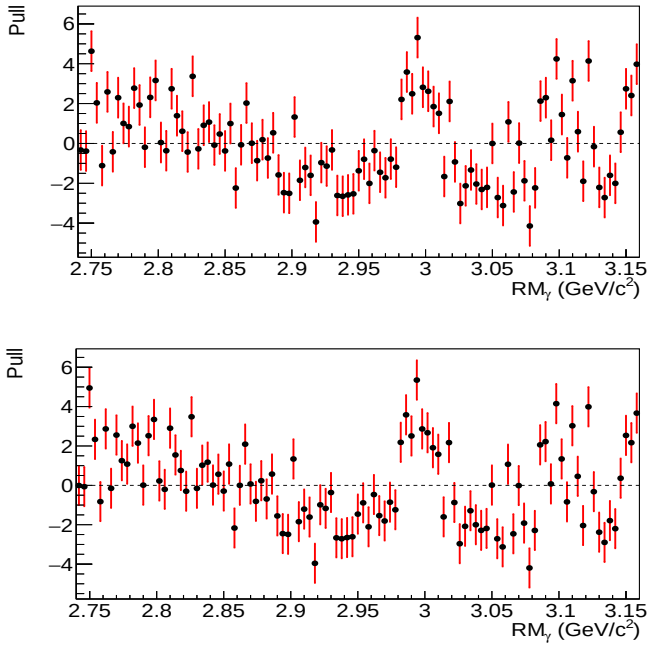

Figure 6.18: The pull distributions of the fit of the data for the $\psi^{'} \rightarrow \gamma\eta_c$ transition, Top: For fitting procedure considering constructive interference, Bottom: For fitting procedure considering the destructive interference.

explained in the following. Note that all the presented systematic errors are relative to the branching fraction.

• Fixed mass, width and interference phase values

The mass and width of the η_c are fixed from the results obtained from the exclusive decay mode of $J/\psi \rightarrow \gamma\eta_c$ which is reported in Chapter 5. The phase values are taken from reference [26] and are fixed in the final fit. Thus, errors of these parameters are part of the systematic errors of this analysis. The values of the mass, width and phase for constructive interference (destructive interference) are $M = 2.9849 \pm 0.0006 \pm 0.0006$ GeV/c^2 ($M = 2.9851 \pm 0.0001 \pm 0.0015$ GeV/c^2), $\Gamma = 0.032 \pm 0.002 \pm 0.001$ GeV ($\Gamma = 0.0310 \pm 0.0002 \pm 0.0022$ GeV), $\phi = 2.40 \pm 0.07 \pm 0.47$ rad ($\phi = 4.19 \pm 0.03 \pm 0.47$ rad), respectively. The first errors are statistical and the second ones are systematic. The total error is given by adding the individual errors in quadrature. First, the branch-

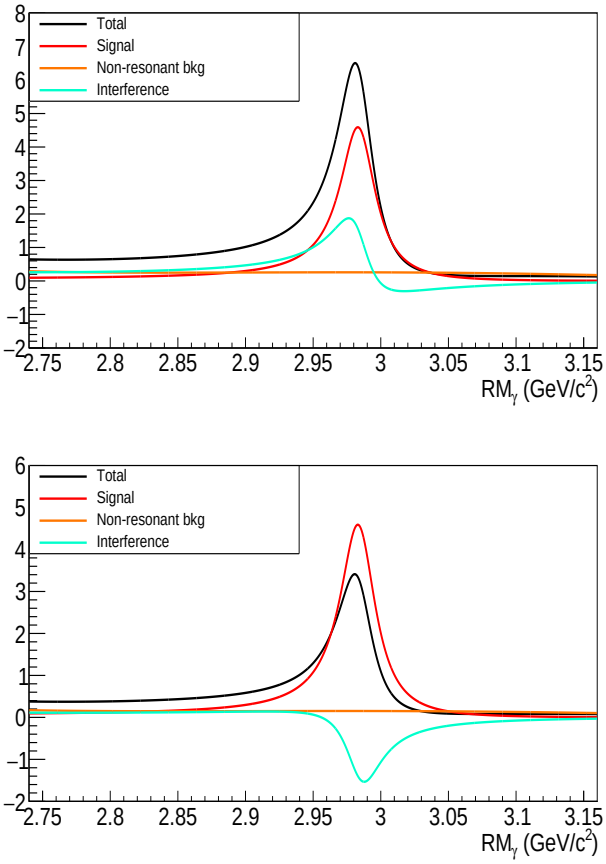

Figure 6.19: The black curve shows the signal which is obtained from the fit result containing three different components, signal (red curve), non-resonant background (orange line) and the interference contribution between signal and non-resonant background (cyan curve), Top: For fitting procedure considering constructive interference, Bottom: For fitting procedure considering destructive interference.

ing fraction is calculated based on nominal values and then it is calculated within the total error and the maximum difference between the results is taken as a systematic error. The estimated errors are represented in Table 6.4 for both constructive and destructive fitting procedures.

• $N_{Pch} > 0, N_{Nch} > 0$, **reducing Bhabha events, reducing** $\pi^+\pi^- J/\psi$ **and reducing non-**ψ' **background**

To determine the systematic error for these requirements, the requirements are removed in the selection process and the branching fraction results are compared to those with the requirement. The difference between the nominal branching fraction and the one without the requirement is taken as a systematic error. The systematic error estimates for all the mentioned requirements are summarized in Table 6.4.

• **Non-resonant line shape**

An alternative line shape for the non-resonant background is obtained from analyzing the inclusive MC sample. All the radiative transitions of $\psi^{'}$, $\psi^{'} \to \gamma X_i$ are chosen and X is always required to have the mother particle $\psi^{'}$ and it is allowed to be anything except the η_c. A second-order polynomial is used to describe this line shape. Then, the flat distribution assumption of the non-resonant background is replaced with the second-order polynomial with fixed parameters obtained from the inclusive MC. The difference between the obtained branching fraction based on a flat distribution assumption and the one based on the second-order polynomial assumption is taken as a systematic error and is estimated to be around 2.9% for the constructive fitting procedure and 0.7% for the destructive fitting procedure.

• **Interference between signal and non-resonant background**

As an alternative scenario, we consider a PDF excluding the interference between the signal and the non-resonant background. In practice, this implies that the α value is assigned to be zero in equation 6.2. Then, the newly-defined PDF is used to perform the fit and to obtain a branching fraction. The quality of the fit is represented in Figure 6.20. Since the fit quality is significantly worse than the scenario including interference effects, we ignore such a hypothesis. Thus, this source of systematic error is not considered.

• **Barrel cut**

The systematic error associated with the barrel cut ($40^\circ < \theta < 140^\circ$) is determined by using an alternative requirement ($30^\circ < \theta < 150^\circ$) and comparing the result with the standard requirement. This tests whether there are edge effects in the EMC that are not properly accounted for in the simulation. The systematic error for this requirement is estimated to be 2% for the constructive interference scenario and 4% for the destructive interference scenario.

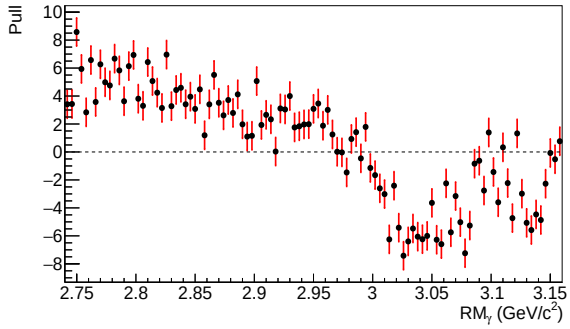

Figure 6.20: The pull distribution for the fit result of the $\psi' \to \gamma\eta_c$ transition obtained from data without considering the interference between signal and non-resonant background.

• Line shape

Since $\psi' \to \gamma\eta_c$ is an electromagnetic-hindered M1 transition and such a transition is proportional to E_γ^7, the events should be weighted with E_γ^7. The systematic error is determined by turning off the weight and taking the difference as a systematic error. The systematic error for both cases of fitting, constructive and destructive is negligible.

• Damping factor

Two different damping factors have been proposed by the KEDR [45] and CLEO [80] collaboration to describe the line shape properly. In our nominal fit, the damping factor is taken from the KEDR collaboration. To account for the systematic error related to the damping factor function, the damping factor in our nominal fit is replaced with the damping factor used by the CLEO-collaboration. The difference between the obtained branching fractions based on these two damping factor functions is taken as a systematic error which is estimated to be negligible.

• Fitting range

The invariant-mass distribution is fitted using different intervals within the range of [2.70, 3.20] GeV/c^2. The largest difference in the extracted branching fractions within the alternative fitting intervals is taken as a systematic error which is estimated to be 6% for the constructive interference scenario and 5% for the destructive interference scenario.

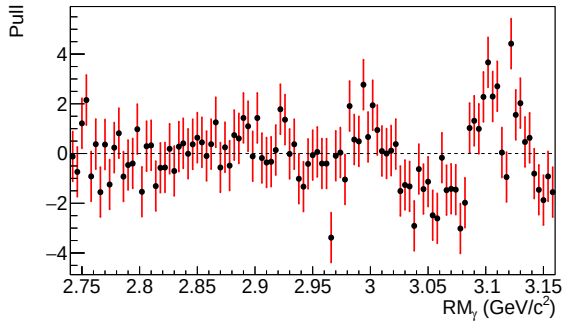

Figure 6.21: The pull distribution for the fit result of the $\psi^{'} \to \gamma\eta_c$ transition obtained from data for the alternative background line shape (two exponential functions) for the constructive fitting procedure. The destructive fitting procedure has the same quality as the constructive fitting procedure.

• Background line shape

In the nominal fit, the background line shape is modeled by using the combinations of three different sources of background which is explained in Section 6.2. Two exponential functions are used as an alternative way to estimate the uncertainty due to the background line shape. The pull distribution for the constructive fitting procedure is represented in Figure 6.21 which shows a reasonable fit quality for the alternative method of the background line shape. The pull distribution for the destructive fitting procedure has the same quality as the constructive fitting procedure. The difference between the results for the branching fraction attributed to two different kinds of the background line shapes is taken as a systematic error which is estimated to be 16% for the constructive interference scenario and 14% for the destructive interference scenario.

• Photon reconstruction

The photon detection efficiency is studied utilizing the control samples $\psi^{'} \to \pi^+\pi^- J/\psi$, $J/\psi \to \rho^\circ\pi^\circ$ and $\psi^{'} \to \pi^\circ\pi^\circ J/\psi$ with $J/\psi \to l^+l^-$ $(l = e, \mu)$ and $\rho^\circ\pi^\circ$. The corresponding systematic uncertainty is estimated by the difference in detection efficiency between data and MC samples, and 1% is assigned for each photon [85].

• Number of $\psi^{'}$ events

An uncertainty of 0.7% is estimated, related to the number of $\psi^{'}$ events as reported

Syst. error sources	constructive interference (%)	destructive interference (%)
Fixed M	0.4	0.5
Fixed Γ	3	3
Fixed ϕ	0.03	0.02
$N_{ch} > 0$	negligible	negligible
$N_{Pch} > 0, N_{Nch} > 0$	0.02	0.06
Reducing Bhabha events	2	2
Reducing non-ψ'	negligible	negligible
Reducing π° background	2	3
Non-resonant line shape	2	0.7
Barrel cut	2	4
Line shape	negligible	negligible
Damping factor	negligible	negligible
Fit range	6	5
Background line shape	16	14
Photon reconstruction	1	1
Number of ψ'	0.7	0.7
Total σ	17	16

Table 6.4: Summary of all the systematic errors. All the errors are relative to the branching fraction. We consider the error negligible if it is smaller than 0.001.

in [84].

6.8.1 Summary of all the systematic errors

All the sources of the systematic errors are summarized in Table 6.4. Assuming all the sources are independent, the total systematic error, σ, is calculated by adding the individual errors in quadrature.

6.9 Results and discussion

Measuring the branching fraction of $\psi' \to \gamma\eta_c$ and increasing the precision were two aims of the reported analysis in this chapter.

It is for the first time that the effect of interference between signal and a non-resonant

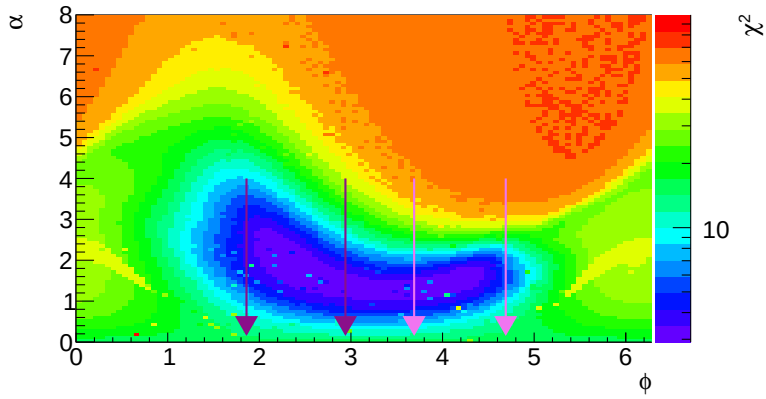

Figure 6.22: The reduced χ^2 values as a function of ϕ (in radian) and α. A goodness-of-fit study in which we systematically varied the fit parameters α and ϕ, representing the strength and phase between the η_c resonance and the non-resonant background, respectively, and we extracted its reduced chi-square for each (α,ϕ) combination. For this scan, all other parameters are fixed. The band between the two purple arrows shows the result of the constructive scenario, $\phi = 2.140 \pm 0.07 \pm 0.47$ and The band between the two pink arrows shows the result of the destructive scenario, $\phi = 4.19 \pm 0.03 \pm 0.47$.

Experimental groups	$\mathcal{B}(\psi' \to \gamma\eta_c) \times 10^{-3}$
This work, constructive	$2.7 \pm 0.07 \pm 0.46$
This work, destructive	$5.3 \pm 0.07 \pm 0.84$
CLEO-2004	$3.2 \pm 0.4 \pm 0.6$
CLEO-2009	$4.32 \pm 0.16 \pm 0.6$
CBALL	2.8 ± 0.6
PDG [48]	3.4 ± 0.5

Table 6.5: Table for the values of the branching fraction compared with other measurements.

background is considered in an inclusive analysis. The branching fraction measurements for two different fitting scenarios, namely assuming a constructive or destructive interference, are reported in Table 6.5. The first error is statistical and the second is systematic. The CLEO measurements are presented in Table 6.5 as well. In the CLEO analysis, the effect of interference is not considered and the PDG value corresponds to the average of measurements by CLEO. Our result for the constructive case has a better precision in comparison with the CLEO result but not for the destructive case.

From the results and analysis procedure discussed in this chapter, we conclude the

following two aspects.

First of all, when comparing the fit quality between a scenario which accounts for a possible interference between signal and a non-resonant background (see Figures 6.18 and 6.20), we show that the interference scenario is highly favoured. Our data, therefore, point to the existence of a modification of the η_c line shape which can be fairly well explained by considering the proposed interference. The data cannot be described by simply taking into account a Breit-Wigner line shape convoluted with the detector response of the calorimeter. This is consistent with the results obtained in a fully exclusive analysis of the same transition, as reported in reference [26]. In this context, it is worth mentioning that the interference phases we extracted from the exclusive study give a reasonably good fit in the inclusive study as well. To get a feeling of our sensitivity to the overall phase factor for this inclusive measurement, we show in Figure 6.22 a goodness-of-fit study in which we systematically varied the fit parameters α and ϕ, representing the strength and phase between the η_c resonance and the non-resonant background, respectively, and we extracted its reduced chi-square for each (α,ϕ) combination. For this scan, all other parameters are fixed. From this figure, it is evident that our inclusive measurement will not be able to precisely determine ϕ, but that our best fit is consistent with the ϕ found in the exclusive study as published by BESIII, which is $\phi = 2.40$ for the constructive scenario and $\phi = 4.19$ for the destructive scenario.

Secondly, in this inclusive analysis we were not able to discriminate between the two interference scenarios corresponding to a constructive and destructive situation. For the determination of the branching fraction it is of utmost importance to settle on this aspect, since the branching fraction is highly sensitive to this. Some ideas are proposed in chapter 7 on how to overcome this challenge.

Chapter 7

Summary and outlook

Quantum chromodynamics (QCD), the theory that describes the strong interactions among with colored quarks and gluons, is part of the Standard Model (SM) and it is based on $SU(3)$ gauge symmetry. Gluons are the force carriers of the theory, like photons for the electromagnetic force in quantum electrodynamics (QED). The strength of QCD is represented by the so-called running coupling constant. At the high-energy regime, also known as the perturbative QCD regime, the coupling constant becomes very small and in this regime, quarks are nearly free or non-interacting. This feature is called asymptotic freedom and QCD is well understood and tested in this regime. In the low-energy regime, referred to as non-perturbative QCD, the coupling constant becomes large and quarks bind together to form hadrons. There are a number of features within the regime of non-perturbative QCD that are presently not well understood. In particular, it remains a mystery what the dynamics are that give rise to the formation of massive hadrons made out of nearly massless constituents. A deeper insight in the degrees of freedom that lead to color confinement is, therefore, needed to make progress in this field.

Charmonium, bound states composed of a charm and anticharm quark pair, is considered as an ideal probe to study the dynamics of QCD. Its mass range covers the transition region between perturbative and non-perturbative QCD, which makes it a perfect probe to study systematically the dynamics of color confinement at various scales. For this, an experimental measurement of the masses and decay properties of various charmonium states is necessary. The first charmonium states, the J/ψ and $\psi^{'}$ vector mesons, were discovered in the seventies. These particles were populated directly in electron-positron annihilations, since they couple to a virtual photon carrying the same quantum numbers. Other charmonium states were discovered later, through indirect methods via radiative and hadronic decays of the $\psi^{'}$.

The ground state of charmonium is a pseudo-scalar particle and is referred to as the η_c. It was discovered in 1980 by the Crystal Ball collaboration via the process $\psi^{'} \rightarrow \gamma\eta_c$.

In the past 40 years, various other experiments using different probes have studied the properties of the η_c, such as its mass and natural width. Strikingly, the various experiments gave results that are not consistent among each other. More recently, a measurement by BESIII of the magnetic dipole (M1) radiative process, $\psi' \to \gamma\eta_c \to$ 6 final-states, demonstrated that these discrepancies might be caused by a line shape distortion due to an interference effect. Since earlier experiments did not account for such an effect, the extracted mass and width could be systematically off, depending on the probe that was used.

This thesis is devoted to a systematic analysis of the radiative M1 transitions of the two lowest lying vector-meson states, J/ψ and ψ', to the ground state, η_c. Data were taken with BESIII using the world's highest statistics in electron-positron annihilations. For both studies, we analysed data collected at a center-of-mass energy corresponding to the nominal mass of the ψ' resonance. An inclusive analysis was carried out with the aim to provide a measurement of the M1 transition rate of $\psi' \to \gamma\eta_c$. In addition, the M1 transition rate of $J/\psi \to \gamma\eta_c$ has been obtained via the exclusive process, $\psi' \to \pi\pi J/\psi,\ J/\psi \to \gamma\eta_c,\ \eta_c \to K^\circ_S K\pi$. The latter reaction gave access to a complementary measurement of the mass and the natural width of the η_c. In all cases, the distortion of the line shape of the η_c has been accounted for by considering an interference effect between the decay of the η_c resonance with other processes that have the same final-state.

To determine the M1 transition rate in $J/\psi \to \gamma\eta_c$, we first selected J/ψ decays by analysing the $\pi^+\pi^-$ recoil mass spectrum in $\psi' \to \pi\pi J/\psi,\ J/\psi \to \gamma\eta_c,\ \eta_c \to K^\circ_S K\pi$. Events with a mass in the vicinity of the nominal J/ψ mass were identified as J/ψ candidates. The photon-recoil mass spectrum in the J/ψ rest frame was obtained by reconstructing and considering all the photon candidates in each event. In this way, we identified a clear signal from the η_c resonance. Various fits including background components and interference scenarios were performed to extract the number of η_c decays to all possible final-states. From this, we were able to determine the branching fraction for the $J/\psi \to \gamma\eta_c$ process. The branching fraction for the constructive scenario was found to be $(1.54 \pm 0.01 \pm 0.21) \times 10^{-2}$ and for the destructive scenario was found to be $(2.11 \pm 0.02 \pm 0.31) \times 10^{-2}$. Besides extracting the branching fraction, $J/\psi \to \gamma\eta_c$, we also used our data to determine the mass and total width of the η_c. This was possible due to the excellent mass resolution we obtained in the exclusive analysis. The detector response was verified by studying the control channel $\psi' \to \gamma\chi_{cj=0,1,2} \to K^\circ_S K\pi\pi\pi$. The obtained values for the constructive interference scenario for the M and Γ are 2.9849 $\pm$ 0.0006 $\pm$ 0.0006 GeV/c^2 and 0.032 $\pm$ 0.002 $\pm$ 0.001 GeV and for the destructive interference scenario are 2.9851 $\pm$ 0.0001 $\pm$ 0.0015 GeV/c^2 and 0.031 $\pm$ 0.002 $\pm$ 0.002 GeV, respectively. In Sections 5.11, 7.1 and 7.2, we discuss these results by comparing

with other measurements and calculations.

Using an inclusive analysis of $\psi^{'} \to \gamma\eta_c$, $\eta_c \to$ anything, we observed a significant η_c signal with a large background in the photon-recoil mass spectrum. Similar to the $J/\psi \to \gamma\eta_c$ analysis, the recoil mass spectrum was fitted to extract the number of η_c signal events, thereby taking into account various sources of backgrounds, the η_c resonance, a model of the detector response, and various interference scenarios possibly affecting the line shape. The interference effect appeared to be important in the inclusive analysis as well. The phases were extracted from an earlier exclusive analysis of BESIII for the channel $\psi^{'} \to \gamma\eta_c$ with η_c decaying into 6 exclusive decay modes. Depending on the two solutions for the phase, we obtained a branching fraction of $\psi^{'} \to \gamma\eta_c$ for the constructive scenario of $(2.7 \pm 0.07 \pm 0.46) \times 10^{-3}$ and for the destructive scenario of $(5.3 \pm 0.07 \pm 0.84) \times 10^{-3}$. From these branching fraction measurements and from our measurement of the total width of the η_c resonance, we extracted the partial width of the M1 radiative transition and compared these results with calculations and other experiments. In Section 7.3, we summarize the outcome of this comparison.

For both the inclusive and exclusive analysis of the M1 transition of the two vector meson states to the ground state of charmonium, we find that the observed line shape can not be described by a Breit-Wigner shape convoluted with the detector response and accounting for various background contributions. This distortion can be resolved by considering an interference component with a non-resonant background. Unfortunately, our data are not sensitive enough to determine the nature of this interference effect. Moreover, we are not able to resolve whether the interference is constructive or destructive, which poses ambiguities in our results, in particular, in the determination of the branching fractions of the M1 transitions. In Section 7.4, we discuss possible future actions that might help to shed further light on these aspects.

7.1 Hyperfine splitting

From the exclusive analysis of the $\psi^{'} \to \pi\pi J/\psi,\ J/\psi \to \gamma\eta_c,\ \eta_c \to K^{\circ}_{S}K\pi$, we extract the mass of the η_c. Our mass measurement of the η_c allows us to determine the S-wave hyperfine splitting, thereby providing a test of the spin-dependent part of the confinement potential. For this, we take the difference of the mass of the J/ψ, obtained from the PDG [48], with our mass measurement of the η_c. S-wave hyperfine splittings of 111.9 ± 0.4 MeV/c^2 and 108.8 ± 0.5 MeV/c^2 are obtained corresponding to the cases in which we assume a constructive or destructive interference in our fit, respectively. Our results are compared in Table 5.5 with different theoretical predictions. Our obtained

result from the constructive (destructive) scenario is consistent within 2σ (5σ) with the latest lattice QCD result and consistent within 2σ (5σ) with the PDG value. Both experimental and theoretical errors have been reduced in the course of time and are now very competitive.

7.2 The partial width of the radiative transition $J/\psi \to \gamma\eta_c$

Chapter 5 of this thesis reported on our measurement of the branching fraction of the radiative decay, $\mathcal{B}(J/\psi \to \gamma\eta_c)$ and the corresponding partial decay width. The partial decay width has been obtained by multiplying our branching fraction with our measurement of the total width of the η_c. Our result for the branching fraction was found to be $(1.54 \pm 0.01 \pm 0.21) \times 10^{-2}$ and $(2.11 \pm 0.02 \pm 0.31) \times 10^{-2}$ by considering a constructive and destructive interference of the η_c signal with a non-resonant background, respectively. We obtained a partial width of $1.43 \pm 0.03 \pm 0.17$ keV for the constructive scenario and $1.94 \pm 0.04 \pm 0.18$ keV for the destructive scenario. Table 7.1 compares our results with predictions of theoretical work and with published results from other experiments.

The theoretical models and experimental probes for this measurement were reviewed in Chapter 2. Our constructive (destructive) result is consistent within 4σ (2σ) with the 2009 and 2012 lattice QCD calculations. In all cases, the result of the destructive scenario has better consistency with lattice QCD than the result of the constructive scenario. In comparison with pNREFT, our constructive (destructive) result is consistent within 2σ (1σ). For the EFT, in both situations, constructive and destructive scenarios, our results are consistent within 1σ. Inconsistency between different theoretical models indicates that the existing models need further improvement.

In comparison with the other experimental measurements, our obtained result based upon a constructive (destructive) scenario is consistent within 1σ (2σ) with the published result from CBALL, 2σ (1σ) with CLEOc and 6σ (4σ) with KEDR. The KEDR collaboration is the only experimental group which considered the effect of interference in their analysis. We note, however, that their experiment was statistically limited which made it impossible for them to have a good estimate on the interference contribution. Moreover, they did not consider both constructive and destructive scenarios in their fit.

Theoretical calculations for $\Gamma(J/\psi \to \gamma\eta_c)$ (keV)	
Lattice QCD (2013) [18]	$2.64 \pm 0.11 \pm 0.03$
Lattice QCD (2012) [22]	$2.49 \pm 0.18 \pm 0.07$
Lattice QCD (2009) [17]	2.51 ± 0.08
NR potential model [29]	1.5
MNR potential model [29]	2.2
pNREFT [41]	2.12 ± 0.40
Quark model [35]	1.25
EFT (average) [41], [42]	1.5 ± 1.0
GI [47]	2.4
Experimental measurements for $\Gamma(J/\psi \to \gamma\eta_c)$ (keV)	
CBALL [44]	1.17 ± 0.32
CLEOc [80]	$1.83 \pm 0.08 \pm 0.19$
KEDR [45]	$2.98 \pm 0.18^{+0.15}_{-0.33}$
PDG value [48]	1.28 ± 0.32
Our measurements for $\Gamma(J/\psi \to \gamma\eta_c)$ (keV)	
Constructive scenario	$1.43 \pm 0.03 \pm 0.17$
Destructive scenario	$1.94 \pm 0.04 \pm 0.18$

Table 7.1: Theoretical calculations and experimental measurements of partial widths (keV) of the M1 radiative transitions for $J/\psi \to \gamma\eta_c$. The presented error of our measurements corresponds to a quadratic sum of statistical and systematic error.

7.3 The partial width of the radiative transition $\psi' \to \gamma\eta_c$

Chapter 6 of this thesis reported on our measurement of the branching fraction of the radiative decay $\mathcal{B}(\psi' \to \gamma\eta_c)$ and the corresponding partial decay width. The original motivation of this analysis is its unique feature. We do not require knowledge on the branching fraction of a biased decay of the η_c into a specific final-state to extract the branching fraction of the radiative process.

Our result for the branching fraction was found to be $(2.7 \pm 0.07 \pm 0.46) \times 10^{-3}$ and $(5.3 \pm 0.07 \pm 0.84) \times 10^{-3}$ by considering a constructive and destructive interference of the η_c signal with a non-resonant background, respectively. We obtained a partial width of $0.79 \pm 0.05 \pm 0.19$ keV for the constructive scenario and $1.57 \pm 0.04 \pm 0.18$ keV for the destructive scenario.

Table 7.2 compares our results with predictions of theoretical work and with published results from other experiments. According to this comparison our results for constructive (destructive) scenario is consistent within $1\sigma(1\sigma)$ with lattice QCD results

Theoretical calculations for $\Gamma(\psi' \to \gamma\eta_c)$ (keV)	
Lattice QCD [22]	0.4 ± 0.8
NR potential model [29]	3.1
MNR potential model [29]	3.8
Quark model [35]	2.41
GI [47]	2.6
Experimental measurements for $\Gamma(\psi' \to \gamma\eta_c)$ (keV)	
CBALL [44]	0.83 ± 0.22
CLEOc-2004 [50]	$0.95 \pm 0.15 \pm 0.21$
CLEOc-2009 [80]	$1.28 \pm 0.06 \pm 0.17$
PDG value [48]	1.01 ± 0.17
Our measurements for $\Gamma(\psi' \to \gamma\eta_c)$ (keV)	
Constructive scenario	$0.79 \pm 0.05 \pm 0.19$
Destructive scenario	$1.57 \pm 0.04 \pm 0.18$

Table 7.2: Theoretical calculations and experimental measurements of partial widths (keV) of the M1 radiative transitions for $\psi' \to \gamma\eta_c$. The presented error of our measurements corresponds to a quadratic sum of the statistical and systematic error.

and is consistent within $1\sigma(2\sigma)$ with the PDG average value. Two different measurements were done with the CLEOc in 2004 and 2009. The first measurement was based on 1.6×10^6 ψ' decays and the second measurement was based on 24.5×10^6 ψ' decays. The 2009 measurement is, therefore, more precise than the 2004 measurement.

The CBALL and CLEOc experimental groups did not consider the effect of interference in their analysis. The advantage of our analysis is that we do consider an interference effect which turned out to be necessary even in the inclusive channel. Note that the accuracy of our result is very competitive with respect to the other measurements. In addition, we demonstrate that it is of utmost importance to have a proper understanding of the line shape in order to obtain an unambiguous determination of the partial width.

7.4 Outlook

Charmonium decays, in particular M1 radiative transitions below the open-charm threshold, have been studied extensively during the past decade. The main objectives of these studies have been to probe the basic properties of various charmonium states, in particular the mass and width of pseudo-scalar states, and to exploit the transition photon as

a probe to study the structure of charmonium states. Moreover, the M1 radiative transition can also be used to search for non-$q\bar{q}$ mesons such as glueballs or other exotics that are predicted by QCD. The vector-meson states of charmonium can, for instance, decay into a photon and two gluons, whereby the two gluons can form a pseudo-scalar glueball state. In this work, we have studied two M1 radiative transition processes, namely, $J/\psi \to \gamma\eta_c$ and $\psi^{'} \to \gamma\eta_c$, with the aim to shed some light on all these enigmas.

By considering the effect of an interference between the signal and a non-resonant background, the branching fractions, $\mathcal{B}(J/\psi \to \gamma\eta_c)$ and $\mathcal{B}(\psi^{'} \to \gamma\eta_c)$ were measured. Without considering the interference effect in both situations, we were not able to get a reasonable fit. In addition, the mass and width of the η_c were measured via the $J/\psi \to \gamma\eta_c$ channel. Our results show that the role of the interference contribution is important for the determination of the branching fraction of M1 transitions and the η_c mass. Although we considered an interference contribution in our fit, we were not able to determine whether it adds constructively or destructively to our signal. Moreover, it is not clear at this stage what is the nature of the non-resonant contribution that appears to interfere with the signal. The possibility that this might be a signature of an exotic hadronic state carrying the same quantum numbers as the η_c can not be excluded. This poses an uncertainty that should be addressed both experimentally and theoretically in future research. Once these aspects are clarified, a significant improvement of the mass and width measurement can follow. There are several alternative approaches that may be helpful in this direction, which will be outlined below.

The most reliable result can be obtained by carrying out a multi-dimensional fit exploiting other observables than the mass, such as the angular distribution. The PWA is one of the methods for implementing the multi-dimensional fit. In our case, a PWA turned out to be difficult to perform because of the complexity of dealing with a three-body final-state in $J/\psi \to \gamma\eta_c$, $\eta_c \to K^{\circ}_{S}K^{\pm}\pi^{\mp}$. Moreover, for the inclusive analysis, $\psi^{'} \to \gamma\eta_c$, we were very limited in the number of observables that were available. One of the proposals is to study one of the two-body decays of the η_c, such as the channel $\eta_c \to \gamma\gamma$. The decay mode of η_c is necessary to determine the momentum of the η_c. In this case, one would be able to do the multi-dimensional fit but the disadvantage of this method is its small branching fraction.

The other channel which would be complementary to study the basic properties of the η_c is the process $h_c \to \gamma\eta_c$. In this case, the electric-dipole (E1) transition is dominant which has a significantly higher branching fraction (about 50%). One expects that the interference effect would be significantly smaller in this case compared to the M1 transition. Promising results have been obtained recently by BESIII and more details can be found in [27]. Although the branching fraction of the E1 transition is

very large, it is difficult to populate the h_c resonance in electron-positron annihilation because of the isospin-suppressed hadronic decay of $\psi^{'} \to \pi^{\circ} h_c$. Here, an experiment like PANDA, using antiproton-proton annihilations, might be advantageous since it can populate directly the h_c resonance. The perspectives of the PANDA experiment will be discussed later in this section.

Besides providing a more accurate determination of the mass and width of the η_c, it would also be helpful to shed more light on the nature of the interference. The first excited state of the η_c, the $\eta_c^{\prime}$, can be an option to get the information related to the interference effect. $\eta_c^{\prime}$ has the same quantum number as the η_c, namely 0^{-+}. A similar interference as was observed in $\psi^{'} \to \gamma\eta_c$ and $J/\psi \to \gamma\eta_c$, might be expected in this transition as well. Combining these results could help to understand its underlying dynamics. The experimental challenge of the measurement of this decay channel is to detect the 48 MeV radiative photons with considerable background. Therefore, the success of this study depends on a careful and detailed analysis of all possible background sources. In 2013, the $\eta_c^{'}$ signal was observed by BESIII via hadronic decay modes of $\eta_c^{'}$, $\psi^{'} \to \gamma K_S^{\circ} K^{\pm}\pi^{\mp}\pi^{+}\pi^{-}$ [26]. The statistical significance of the observed signal was found to be 4σ.

Besides studying the η_c indirectly via e^+e^- annihilations, an alternative approach would be to populate this state directly in antiproton-proton collisions such as being planned for the PANDA experiment at the future facility FAIR [137]. Using a resonance scan by varying the antiproton-beam momentum in the vicinity of the η_c mass and using a complementary initial channel, one would be able to study its line shape in great detail. Since PANDA is a future experiment that will start taking data around 2025, we do not have lots of detailed information on the performance of antiproton-proton annihilations to extract the information of η_c. Some preliminary studies were carried out by E835 at Fermilab [136]. In their analysis, an interference with continuum $\gamma\gamma$ production was considered and the conclusion was that the interference affects the peak position of the η_c mass. We can estimate the production cross section $p\bar{p} \to \eta_c$ by making use of the detailed balance formula [137]:

$$\sigma(p\bar{p} \to \eta_c) = \frac{4(2J+1)\pi}{M_{\eta_c}^2 - 4m_p^2} \times \mathcal{B}(\eta_c \to p\bar{p}), \tag{7.1}$$

where J is the spin of η_c, m_p and m_{η_c} are the masses of proton and η_c respectively, and $\mathcal{B}(p\bar{p} \to \eta_c)$ is taken from the BESIII measurement [135]. With the most recent values, we estimate a cross section of $\sigma(p\bar{p} \to \eta_c) = 1.67$ μb. The expected number of events for the transition $\eta_c \to p\bar{p}$ can be obtained by:

$$N_{expected} = L \cdot t \cdot \sigma(p\bar{p} \to \eta_c) \cdot \epsilon, \tag{7.2}$$

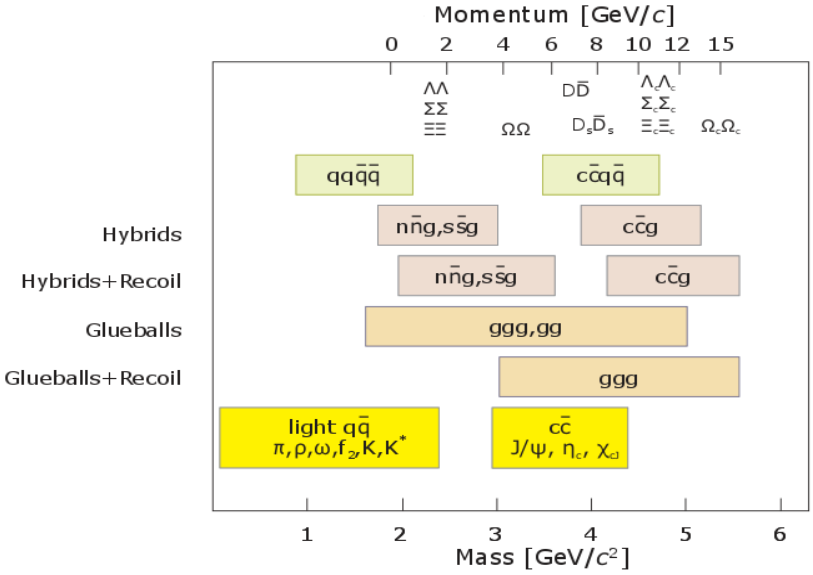

Figure 7.1: An overview of the hadronic states that will be addressed by the future experiment PANDA using a high-intensity momentum-cooled antiproton beam. The available antiproton-beam momenta are indicated in the figure together with the corresponding mass range [137].

where L is the luminosity, t is the accumulated beam time and ϵ is the detection efficiency. Assuming $L = 2 \cdot 10^{32}$ cm^{-2}s^{-1}, $t = 30$ days and a 10% detection efficiency, the expected number of events for the $p\bar{p} \to \eta_c$ transition is estimated to be 28×10^6 signal events which indicate that $p\bar{p} \to \eta_c$ is a good candidate to get access to the line shape of the η_c.

The analysis and results presented and discussed in this thesis show that it remains experimentally challenging to extract some of the basic parameters of one of the most important states in charmonium, namely its ground state. Although, there are numerous experiments and methods that have become available to study this state, the accuracy of extracting some of its basic parameters, such as the mass and width, remains limited due to systematic effects that are difficult to control. In order to reach a similar precision as obtained for the J/ψ, one needs to address the observed inconsistencies. To this end, it might be advantageous to consider an analysis framework in which one tries to analyse the various probes in a unique and consistent manner. One could think of an extended PWA in which all available data, based on a large spectrum of initial and final-states, are combined to unambiguously extract the basic parameters of the η_c. Such a framework does not exist at present, but it might be worthwhile to develop in the near future. This

would require a common effort between theory and experiment.

The nature of the observed interference remains a mystery. In order to provide insight, it is necessary to develop our theoretical basis further. One possible and intriguing explanation of the interference could be related to the existence of exotic states, such as glueballs. Figure 7.1 gives an overview of possible hadronic states in the vicinity of the charmonium spectrum. Note that it includes the possibilities of glueball bound states composed out of colorless combinations of two or three gluons. It is conceivable that the process $J/\psi(\psi') \to \gamma\eta_c \to \gamma X$ interferes with such an intermediate glueball state, such as $J/\psi(\psi') \to \gamma gg \to \gamma X$ decay. The η_c meson decays mainly into two gluons and the lower-order Feynman diagrams for these processes are very similar, which makes an interference with a two-gluon state very likely.

Chapter 8

Nederlandse Samenvatting

Quantum Chromodynamics (QCD), de theorie die de sterke interacties tussen gekleurde quarks en gluons omschrijft, maakt deel uit van het Standard Model (SM) en is gebaseerd op een abstracte rotatiesymmetrie, de zogenaamde $SU(3)$ gauge symmetrie. Gluonen zijn de krachtdragers van de sterke kracht, zoals fotonen voor de elektromagnetische kracht in kwantumelektrodynamica (QED). De sterkte van QCD wordt vertegenwoordigd door de zogenaamde loopkoppelingskonstante. In de hoge-energie bereik, ook wel bekend als perturbative QCD-regime, wordt de koppelingskonstante zeer klein en in dit regime bewegen quarks als nagenoeg vrije deeltjes. Deze eigenschap heet asymptotische vrijheid en QCD is goed begrepen en getest in dit bereik. Het lage-energie bereik, waarnaar wordt gerefereerd als niet-perturbative QCD, wordt de koppelingskonstante groot en quarks binden samen om hadronen te vormen. Er zijn een aantal eigenschappen binnen het energiebereik van de niet-perturbative QCD die momenteel niet goed begrepen worden. In het bijzonder blijft het een mysterie wat de dynamiek is die leidt tot de vorming van massieve hadronen gemaakt uit bijna massaloze componenten. Een dieper inzicht in de vrijheidsgraden die tot kleur leiden, is derhalve nodig om vooruitgang te boeken op dit gebied.

Charmonium, gebonden-toestanden samengesteld uit een charm en anticharm quark paar, wordt beschouwd als een ideale sonde om de dynamiek van QCD te bestuderen. De massa van charmonium ligt in het overgangsgebied tussen perturbatieve en niet-perturbatieve QCD, waardoor het een perfecte sonde is om systematisch de dynamiek van kleur op verschillende schalen te bestuderen. Hiervoor is een experimentele meting van de massa's en vervaleigenschappen van verschillende charmoniumstaten nodig. De eerste twee charmoniumtoestanden, de J/ψ en ψ' vector mesonen, werden ontdekt in de jaren zeventig. Deze deeltjes kunnen direct worden gevormd in elektron-positron botsingen, aangezien ze koppelen aan een virtueel foton met dezelfde spin en pariteit als de charmoniumtoestanden. Andere charmonium-toestanden werden later ontdekt via indirecte hadronische en electromagnetische vervallen van de ψ'.

De grondtoestand van charmonium is een pseudo-scalaire deeltje en wordt aangeduid als met η_c. Het werd in 1980 ontdekt door de Crystal Ball collaboratie via het proces $\psi' \to \gamma\eta_c$. In de afgelopen 40 jaar bestudeerden diverse andere experimenten met behulp van verschillende probes de eigenschappen van de η_c, zoals zijn massa en natuurlijke breedte. Opvallend was dat de resultaten van de verschillende experimenten niet goed met elkaar overeenkwamen. Recentelijk heeft een meting van de BESIII collaboratie via het electromagnetische dipool (M1) verval, $\psi' \to \gamma\eta_c \to 6$ eindtoestanden aangetoond dat betreffende discrepanties kunnen worden veroorzaakt door een interferentie effect waardoor de resonantie vervormd kan worden. Aangezien eerdere experimenten geen rekening hielden met een dergelijk effect, werden de massa en breedte systematisch foutief bepaald, afhankelijk van de gebruikte sonde.

Dit proefschrift is gewijd aan een systematische analyse van de electromagnetische M1-overgangen van de twee laagst liggende vector-meson toestanden, J/ψ en ψ', naar de grondtoestand, η_c. Gegevens werden bij BESIII genomen met de hoogste statistieken ter wereld in elektron-positron botsingen. Voor beide studies analyseerden we data verzameld op een massa-middelpunt-energie die overeenkomt met de nominale massa van de ψ' resonantie. Een inclusieve analyse wordt uitgevoerd met als doel een meting van de M1 overgangssnelheid van $\psi' \to \gamma\eta_c$ te geven. Daarnaast is de M1 overgangssnelheid van $\psi' \to \gamma\eta_c$ verkregen via het exclusieve proces, $\psi' \to \pi\pi J/\psi,\ J/\psi \to \gamma\eta_c,\ \eta_c \to K^\circ_S K\pi$. De laatste reactie gaf toegang tot een complementaire meting van de massa en de natuurlijke breedte van de η_c. In alle gevallen is de vervorming van de resonantievorm van de η_c meegenomen door een interferentie-effect te overwegen tussen het verval van de η_c resonantie en andere processen die dezelfde eindtoestand hebben.

Om de M1 overgangsgsnelheid te bepalen in $J/\psi \to \gamma\eta_c$, hebben we eerst J/ψ vervallen geselecteerd door het $\pi^+\pi^-$ terugslag-massa spectrum in $\psi' \to \pi\pi J/\psi,\ J/\psi \to \gamma\eta_c,\ \eta_c \to K^\circ_S K\pi$ te analyseren. Gebeurtenissen met een massa in de buurt van de nominale J/ψ massa werden geïdentificeerd als J/ψ kandidaten. Het foton-terugslag massa spectrum in het J/ψ ruststelsel werd verkregen door alle fotonkandidaten in elke interactie te reconstrueren en te overwegen. Op deze manier konden we een duidelijk signaal identificeren afkomstig van de η_c resonantie. Verschillende fits inclusief achtergrondcomponenten en interferentiescenario's werden uitgevoerd om het aantal η_c vervallen naar alle mogelijke eindtoestanden af te leiden. Hieruit kunnen we de vertakkingsfractie bepalen voor het $J/\psi \to \gamma\eta_c$ proces.

Hoofdstuk 5 van dit proefschrift beschrijft onze meting van de vertakkingsfractie van het stralingsverval, $\mathcal{B}(J/\psi \to \gamma\eta_c)$. Ons resultaat voor de vertakkingsfractie bleek $(1.54 \pm 0.01 \pm 0.21) \times 10^{-2}$ en $(2.11 \pm 0.02 \pm 0.31) \times 10^{-2}$ te zijn door het beschouwen van een respectievelijk constructieve en destructieve interferentie van het η_c signaal met

een niet-resonante achtergrond. De gemeten waarde van de vertakkingsfractie wordt weergegeven in tabel 5.4 en vergeleken met de resultaten van andere experimenten. Ons resultaat dat is gebaseerd op het constructieve interferentie scenario is consistent met de CLEO en CBALL resultaten binnen de foutenmarges, maar niet voor het destructieve interferentie scenario. In het geval van het constructieve interferentie scenario hebben we de fouten verbeterd ten opzichte van eerdere experimenten.

Naast de vertakkingsfractie, $J/\psi \to \gamma\eta_c$, hebben we ook onze gegevens gebruikt om de massa en totale breedte van de η_c te bepalen. Dit was mogelijk door de uitstekende massa resolutie die we in de exclusieve analyse hebben verkregen. De detector respons werd geverifieerd door het controlekanaal $\psi' \to \gamma\chi_{cj=0,1,2} \to K^{\circ}_{S}K\pi\pi\pi$ te bestuderen. De verkregen waarden voor het constructieve interferentiescenario voor de M en Γ zijn 2.9849 $\pm$ 0.0006 $\pm$ 0.0006 GeV/c^2 en 0.032 $\pm$ 0.002 $\pm$ 0.001 GeV, en voor het destructieve interferentiescenario 2.9851 $\pm$ 0.0001 $\pm$ 0.0015 GeV/c^2 en 0.031 $\pm$ 0.002 $\pm$ 0.002 GeV, respectievelijk.

Onze massameting van de η_c stelt ons in staat om de S-wave hyperfijnsplitsing te bepalen, waardoor een test van het spin-afhankelijke deel van de confinement-potentiaal wordt verkregen. Hiervoor nemen we het verschil van de massa van de J/ψ, uit het werk van de Particle Data Group, (PDG) [48], met onze massa-meting van de η_c. Een S-wave hyperfijnsplitsing van 111.9 $\pm$ 0.4 MeV/c^2 en 108.8 $\pm$ 0.5 MeV/c^2 werden verkregen overeenkomstig de gevallen waarin we een constructieve of destructieve interferentie aannemen in onze fit, respectievelijk. Onze resultaten worden vergeleken in tabel 5.5 met verschillende theoretische voorspellingen. Ons verkregen resultaat van constructief (destructief) scenario is consistent binnen 2σ (5σ) met het laatste resultaat van een Lattice-QCD berekening en consistent binnen 2σ (5σ) met de PDG waarde. Zowel experimentele als theoretische fouten zijn in de loop der tijd verminderd en zijn nu met deze resultaten zeer competitief.

Met behulp van een inclusieve analyse van $\psi' \to \gamma\eta_c$, $\eta_c \to$ alles, vonden we een significant η_c signaal met een grote achtergrond in het foton-recoil massaspectrum. Net als in de $J/\psi \to \gamma\eta_c$ analyse is het recoil-massaspectrum gefit om het aantal η_c signaal-gebeurtenissen te bepalen, waarbij rekening wordt gehouden met verschillende bronnen van achtergronden, de η_c resonantie, een model van de detector respons, en diverse interferentie scenario's die mogelijk de lijnvorm beïnvloeden. Het interferentie-effect bleek ook belangrijk te zijn in de inclusieve analyse. Afhankelijk van de twee oplossingen voor de interferentiefase kregen we een vertakkingsfractie van het inclusieve verval $\psi' \to \gamma\eta_c$ voor het constructieve scenario van (2.7 $\pm$ 0.07 $\pm$ 0.46) $\times 10^3$ en voor het destructieve scenario van (5.3 $\pm$ 0.07 $\pm$ 0.84) $\times 10^3$. Uit deze meting van de vertakkingsfractie en van onze meting van de totale breedte van de η_c resonantie, hebben we de gedeel-

telijke breedte van de M1-stralingsovergang bepaald en deze resultaten vergeleken met berekeningen en de resultaten van andere experimenten. In sectie 8.1 vatten we het resultaat van deze vergelijking samen. Het is voor het eerste keer dat het effect van interferentie tussen signaal en niet-resonante achtergrond in een inclusieve analyse wordt overwogen.

Voor zowel de inclusieve en exclusieve analyse van de M1-overgang van de twee vector-meson toestanden naar de grondtoestand van charmonium, vinden we dat de waargenomen lijnvorm niet kan worden beschreven door een Breit Wigner-vorm rekening houdend met de detectorrespons en met verschillende achtergrondbijdragen. De waargenomen resonantievorm kan worden beschreven door een interferentiecomponent met een niet-resonante achtergrond te beschouwen. Helaas zijn onze gegevens niet gevoelig genoeg om de aard van dit interferentie-effect te bepalen. Bovendien kunnen we niet bepalen of de interferentie constructief of destructief is, wat ambiguiteiten in onze resultaten inhoudt, met name bij de bepaling van de vertakkingsfracties van de M1-overgangen. In sectie 8.1 bespreken we mogelijke toekomstige acties die kunnen helpen om deze aspecten verder te verlichten.

8.1 Vooruitzicht

Naast een nauwkeuriger bepaling van de massa en breedte van de η_c, zou het ook nuttig zijn om meer licht op de aard van de interferentie te werpen. De eerste aangeslagen toestand van η_c, de η_c', kan een optie zijn om de informatie met betrekking tot het interferentie-effect te krijgen. η_c' heeft hetzelfde kwantumgetal als de η_c, namelijk 0^{-+}. Een soortgelijke interferentie als waargenomen in $\psi^{'} \to \gamma\eta_c$ en $J/\psi \to \gamma\eta_c$, kan ook in deze overgang worden verwacht. Het combineren van deze resultaten kan helpen om de onderliggende dynamiek te begrijpen. De experimentele uitdaging van de meting van dit vervalkanaal is het detecteren van de 48 MeV stralingsfotonen met een aanzienlijke achtergrond. Daarom is het succes van deze studie afhankelijk van een zorgvuldige en gedetailleerde analyse van alle mogelijke achtergrondbronnen. In 2013 werd het $\eta_c^{'}$-signaal waargenomen door BESIII via hadronische verval van $\eta_c^{'}$, $\psi^{'} \to \gamma K_S^{\circ} K^{\pm}\pi^{\mp}\pi^{+}\pi^{-}$. De statistische significantie van het waargenomen signaal bleek 4σ te zijn.

Naast de indirecte studie van η_c via e^+e^- annihilaties, zou een alternatieve aanpak zijn om deze toestand direct in antiproton-protonbotsingen te produceren, zoals wordt gepland voor het PANDA-experiment bij de toekomstige faciliteit FAIR [137]. Met behulp van een resonantie-scan, door de impuls van de antiprotonenbundel in de buurt van de η_c massa te varieren en een complementair initieel kanaal te gebruiken, zou men

de η_c lijnvorm in detail kunnen bestuderen.

De analyse en resultaten die in dit proefschrift worden voorgesteld en besproken, tonen aan dat het experimenteel uitdagend blijft om enkele basisparameters van een van de belangrijkste toestanden in charmonium te bepalen, namelijk de grondtoestand ervan. Hoewel er tal van experimenten en methoden beschikbaar zijn om de charmonium grondtoestand te bestuderen, blijft de nauwkeurigheid van het extraheren van enkele basiswaarden, zoals massa en breedte, beperkt door systematische effecten die moeilijk te beheersen zijn. Om een nauwkeurigheid te bereiken op een niveau dat gelijk is aan dat verkregen voor bijvoorbeeld J/ψ, moet men de waargenomen inconsistenties aanpakken. Daartoe kan het voordelig zijn om een analyse kader te overwegen waarin men de verschillende sonden probeert te analyseren op een unieke en consistente wijze. Men zou kunnen denken aan een uitgebreid Partial-Wave Analysis (PWA) waarin alle beschikbare gegevens, gebaseerd op een groot spectrum van initiale en eindtoestanden, gecombineerd worden om de basisparameters van de η_c ondubbelzinnig te bepalen. Zo'n kader bestaat momenteel niet, maar het kan wellicht de moeite waard zijn om dit in de nabije toekomst te ontwikkelen. Dit vereist een gemeenschappelijke inspanning tussen theorie en experiment.

De aard van de waargenomen interferentie blijft een mysterie. Om inzicht te geven, is het noodzakelijk onze theoretische basis verder te ontwikkelen. Een mogelijke en intrigerende verklaring van de interferentie kan verband houden met het bestaan van exotische toestanden. Figure 7.1 geeft een overzicht van mogelijke hadronische toestanden in de buurt van het charmonium spectrum. We houden rekening met mogelijke lijmbal-toestanden, bijzondere deeltjes die bestaan uit kleurloze twee-of-drie gluonen. Het is denkbaar dat het proces $J/\psi(\psi^{'}) \rightarrow \gamma\eta_c \rightarrow \gamma X$ interfereert met een dergelijke intermediaire glueball-toestand, zoals het $J/\psi(\psi^{'}) \rightarrow \gamma gg \rightarrow \gamma X$ verval. De η_c meson vervalt hoofdzakelijk in twee gluonen en de lagere-orde Feynman-diagrammen voor deze processen zijn zeer vergelijkbaar, waardoor een interferentie met een twee-gluon-toestand zeer waarschijnlijk is.

Acknowledgement

It is time to thank all the people that contributed to this work by their persistent encouragement and unscrupulous support for me during this challenging 4-year period.

First of all, I would like to express my very great appreciation to my supervisor, Johan Messchendorp. My words are not able to appreciate you for your patient guidance and support throughout my PhD studies. Definitely, without your creative scientific insights and ongoing discussions, I would not have been able to complete this project.

I would very much like to thank Prof. Nasser Kalantar, who not only provided scientific inspirations for many new ideas in the advancement of this study and for the analysis of the data, but also taught me a lot of life lessons.

I would also like to thank Prof. Gerald Feldman, Prof. Olaf Scholten, and Prof. Raimond Snellings, the reading committee, for their valuable comments and constructive suggestions.

I wish to thank the BESIII collaboration, and especially the M1 transition group. Scientific discussions in this group helped me resolve the challenges I faced in this research. In particular, I appreciate Ke Li, who was a valuable source of technical information for BESIII analysis. I warmly thank you for your answering all my questions with great responsibility.

Dear Alex and Ali, thank you for being my paranymphs. Alex, I cannot imagine a better officemate than you. You are a very valuable friend to me. The 3 p.m. breaks will remain one of my best memories of KVI. I appreciate Mohammad Babai for the valuable comments provided. Your presence at KVI was very valuable to me. I also express my gratitude to Ali Najafi for great companionship and encouragements like a caring brother from my first day at KVI. I thank Olga very much. Your scientific support in the early PhD program paved the way for my further advancements. I would like to appreciate Auke for all his support. I wish to thank Solmaz. I will never forget the good times we had with each other in our trips around Europe.

I give my appreciation and gratitude to all my very good friends at KVI, who made my years of PhD full of sweet and unforgettable memories.

I want to extend my most heartfelt appreciation to my kind and loving parents, Majid and Afsaneh; my compassionate brothers Amir and Ali; and my matchless sister, Sara. My statements cannot thank you for your unreserved support during these years and no words can express my love and affection for you. Thank you for your presence. I dedicate this dissertation to you, my most loved ones in the world.

Appendix A

Kinematic fitting

A.0.1 General algorithm

This section is adopted from BESIII book [58].
The fitting technique is straightforward and is based on the well-known Lagrange multiplier method [115]. It is assumed that the constraint equations can be linearized and summarized in two matrices, $\mathbf{D}$ and $\mathbf{d}$. Let α represent the parameters for a set of n tracks. It has the form of a column vector

$$\alpha = \begin{pmatrix} \alpha_1 \\ \alpha_2 \\ \vdots \\ \alpha_n \end{pmatrix}. \tag{A.1}$$

Initially, the track parameters have the unconstrained values α_0, obtained from the reconstruction. The r constraint functions can be written generally as

$$\mathbf{H}(\alpha) \equiv 0, \quad \text{where } \mathbf{H} = \begin{pmatrix} H_1 & H_2 & \cdots & H_r \end{pmatrix}. \tag{A.2}$$

Expanding (A.2) around a convenient point α_A yields the linearized equations

$$0 = \frac{\partial H(\alpha_A)}{\partial \alpha}(\alpha - \alpha_A) + H(\alpha_A) = \mathbf{D}\delta\alpha + \mathbf{d}, \tag{A.3}$$

where $\delta\alpha = \alpha - \alpha_A$. Thus we have

$$\mathbf{D} = \begin{pmatrix} \frac{\partial H_1}{\partial \alpha_1} & \frac{\partial H_1}{\partial \alpha_2} & \cdots & \frac{\partial H_1}{\partial \alpha_n} \\ \frac{\partial H_2}{\partial \alpha_1} & \frac{\partial H_2}{\partial \alpha_2} & \cdots & \frac{\partial H_2}{\partial \alpha_n} \\ \vdots & \vdots & \ddots & \vdots \\ \frac{\partial H_r}{\partial \alpha_1} & \frac{\partial H_r}{\partial \alpha_2} & \cdots & \frac{\partial H_r}{\partial \alpha_n} \end{pmatrix}, \quad \mathbf{d} = \begin{pmatrix} H_1(\alpha_A) \\ H_2(\alpha_A) \\ \vdots \\ H_r(\alpha_A) \end{pmatrix}, \tag{A.4}$$

or $D_{ij} = \dfrac{\partial H_i}{\partial \alpha_j}$ and $d_i = H_i(\alpha_A)$. The constraints are incorporated using the method of Lagrange multipliers in which the χ^2 is written as a sum of two terms

$$\chi^2 = (\alpha - \alpha_0)^T V_{\alpha_0}^{-1} (\alpha - \alpha_0) + 2\lambda^T (\mathbf{D}\delta\alpha + \mathbf{d}), \tag{A.5}$$

where λ is a vector of r unknown Lagrange multipliers. Minimizing the χ^2 with respect to α and λ yields two vector equations that can be solved for parameters α and their covariance matrix:

$$\begin{array}{c} V_{\alpha_0}^{-1}(\alpha - \alpha_0) + \mathbf{D}^T\lambda = 0, \\ \mathbf{D}\delta\alpha + \mathbf{d} = 0. \end{array} \tag{A.6}$$

The solution can be written as:

$$\begin{array}{c} \alpha = \alpha_0 - V_{\alpha_0}\mathbf{D}^T\lambda, \\ \lambda = V_D(\mathbf{D}\delta\alpha_0 + \mathbf{d}), \\ V_\alpha = V_{\alpha_0} - V_{\alpha_0}\mathbf{D}^T V_D \mathbf{D} V_{\alpha_0}, \end{array} \tag{A.7}$$

where $V_D = \left(\mathbf{D}V_{\alpha_0}\mathbf{D}^T\right)^{-1}$ is the $r \times r$ constraint covariance matrix and

$$\chi^2 = \lambda^T V_D^{-1} \lambda = \lambda^T (\mathbf{D}\delta\alpha_0 + \mathbf{d}). \tag{A.8}$$

Note that the χ^2 can be written as a sum of r distinct terms, one for each constraint. It can be shown that the new covariance matrix V_α has diagonal elements that are smaller than the initial covariance matrix V_{α_0}. In general, the non-linearities of the constraint equations requires that the kinematic fitting procedure be applied iteratively until satisfactory convergence is achieved. Track parameters and their errors, covariance matrices, fit information and other quantities can be obtained after fitting.

The constraints "pull" the tracks away from their unconstrained values. The "pull" of the $i^{\text{th}}-$track parameter is defined as:

$$(\text{pull})_i = \frac{\alpha_i - \alpha_{0i}}{\sqrt{(V_{\alpha_0})_{ii} - (V_\alpha)_{ii}}}. \tag{A.9}$$

This is an important variable to test the track parameter and its error. The resulting χ^2 that is obtained with r constraints is distributed like a standard χ^2 with r degrees of freedom, if Gaussian errors apply. Of course, since track errors are only approximately Gaussian, the actual distribution will have more events in the tail than predicted by theory. Still, knowledge of the distribution allows one to define reasonable χ^2 cuts.

It is useful to compute how far the parameters have to move to satisfy a particular constraint j. The initial "distance from satisfaction" can be characterized by the quantity $(\mathbf{D}\delta\alpha_0 + \mathbf{d})_j$ and the number of standard deviations away from satisfying the constraint is easily calculated to be

$$\sigma_j = \frac{D_{ji}\delta\alpha_{0i} + d_j}{\sqrt{(V_D^{-1})_{jj}}}. \tag{A.10}$$

This information can be used to provide criteria for rejecting background in addition to the overall χ^2.

A.0.2 Kinematic constraints

In this section, we will compute the explicit form of the **D** and **d** matrices for constraints commonly encountered in high energy physics. If multiple constraints are desired then one just extends the matrices by adding rows to them, one row per constraint. E_c, p_c and m_c indicate the energy, momentum and mass related the applied constraint. This allows many constraints to be used simultaneously in the fit.

1. Invariant-mass constraint

$$H = E^2 - p_x^2 - p_y^2 - p_z^2 - m_c^2 = 0; \tag{A.11}$$

$$\mathbf{D} = \begin{pmatrix} -2p_x & -2p_y & -2p_z & 2E & 0 & 0 & 0 \end{pmatrix}; \tag{A.12}$$

$$d = E^2 - p_x^2 - p_y^2 - p_z^2 - m_c^2 = 0. \tag{A.13}$$

2. Total energy constraint

$$H = E - E_c = 0; \tag{A.14}$$

$$\mathbf{D} = \begin{pmatrix} 0 & 0 & 0 & 1 & 0 & 0 & 0 \end{pmatrix}; \tag{A.15}$$

$$\mathbf{d} = E - E_c. \tag{A.16}$$

3. Total momentum constraint

$$H = \sqrt{p_x^2 + p_y^2 + p_z^2} - p_c = 0; \tag{A.17}$$

$$\mathbf{D} = \begin{pmatrix} p_x/p & p_y/p & p_z/p & 0 & 0 & 0 & 0 \end{pmatrix}; \tag{A.18}$$

$$d = \sqrt{p_x^2 + p_y^2 + p_z^2} - p_c. \tag{A.19}$$

4. Total 3-vector constraint

$$H = \begin{pmatrix} p_x - p_{cx} \\ p_y - p_{cy} \\ p_z - p_{cz} \\ E - E_c \end{pmatrix} = 0; \tag{A.20}$$

$$\mathbf{D} = \begin{pmatrix} 1 & 0 & 0 & 0 & 0 & 0 & 0 \\ 0 & 0 & 1 & 0 & 0 & 0 & 0 \\ 0 & 0 & 0 & 1 & 0 & 0 & 0 \end{pmatrix}; \tag{A.21}$$

$$\mathbf{d} = \begin{pmatrix} p_x - p_{cx} \\ p_y - p_{cy} \\ p_z - p_{cz} \\ E - E_c \end{pmatrix}. \tag{A.22}$$

5. Total 4-vector constraint

$$H = \begin{pmatrix} p_x - p_{cx} \\ p_y - p_{cy} \\ p_z - p_{cz} \\ E - E_c \end{pmatrix} = 0; \tag{A.23}$$

$$\mathbf{D} = \begin{pmatrix} 1 & 0 & 0 & 0 & 0 & 0 & 0 \\ 0 & 0 & 1 & 0 & 0 & 0 & 0 \\ 0 & 0 & 0 & 1 & 0 & 0 & 0 \\ 0 & 0 & 0 & 0 & 1 & 0 & 0 \end{pmatrix}; \tag{A.24}$$

$$\mathbf{d} = \begin{pmatrix} p_x - p_{cx} \\ p_y - p_{cy} \\ p_z - p_{cz} \\ E - E_c \end{pmatrix}. \tag{A.25}$$

6. Equal mass constraint

$$H = (E_1^2 - p_{1x}^2 - p_{1y}^2 + p_{1z}^2) - (E_2^2 - p_{2x}^2 - p_{2y}^2 + p_{2z}^2) = 0; \tag{A.26}$$

$$\mathbf{D_1} = \begin{pmatrix} -2p_{1x} - 2p_{1y} - 2p_{1z} - 2p_{1z} - 2E_1 & 0 & 0 & 0 \end{pmatrix}; \tag{A.27}$$

$$\mathbf{D_2} = \begin{pmatrix} -2p_{2x} - 2p_{2y} - 2p_{2z} - 2p_{2z} - 2E_2 & 0 & 0 & 0 \end{pmatrix}; \tag{A.28}$$

$$\mathbf{d} = \left(E_1^2 - p_{1x}^2 - p_{1y}^2 + p_{1z}^2\right) - \left(E_2^2 - p_{2x}^2 - p_{2y}^2 + p_{2z}^2\right). \tag{A.29}$$

Once these matrices are known, the tracks can be kinematically fitted using the procedure described in the previous section.

Bibliography

[1] S. Bethk, *Eur. Phys. J. C* **64** (2009) 689, [arXiv:0908.1135 [hep-ph]].

[2] G. M. Prosperi, M. Raciti and C. Simolo, *Nucl. Phys.* **58** (2006) 387, [arXiv:0607209v2 [hep-ph]].

[3] P. Fritzsch *et al.*, *Nucl. Phys. B* **865** (2012) 397, [arXiv:1205.5380 [hep-ph]].

[4] S. L. Olsen, *Hyperfine Interact.* **229** (2014) 7, [arXiv:1403.1254 [hep-ex]].

[5] M. Voloshin, *Prog. Part. Nucl. Phys* **61** (2008) 455, [arXiv:0711.4566 [hep-ph]].

[6] D. M. Asner *et al.*, *Progress in Particle and Nuclear Physics.* **54** (2005) 615.

[7] Website *https://home.cern/about/experiments.*

[8] A. Buijs, *Nucl. Phys. B (Proc. Suppl.)* **82** (2000) 300.

[9] C. Michael, *Nucl. Phys. B* **259** (1985) 58.

[10] B. Blossier, M. DellaMorte, G. von Hippel, T. Mendes, and R. Sommer, *JHEP 0904:094* (2009), [arXiv:0902.1265[hep-lat].

[11] K. G. Wilson, *Phys. Rev. D* **10** (1974) 2445.

[12] G. Bali, S. Collins, P. Pérez-Rubio, *Phys. Rev. D* **92** (2015) 034504.

[13] Sasa Prelovsek, *in 7th International Workshop on Charm Physics (Charm 2015) Detroit, MI, USA, May 18-22* (2015), [arXiv:1508.07322 [hep-lat]].

[14] K. A. Olive *et al.*, *(Particle Data Group), Chinese. Phys. C* **38** (2014) 090001.

[15] B. A. Galloway, P. Knecht, J. Koponen, C. T. H. Davies, and G. P. Lepage, *PoS LATTICE2014* **092** (2014), [arXiv:1411.1318 [hep-lat]].

[16] J. J. Dudek, R. G. Edwards, and D. G. Richards, *Phys. Rev. D* **73** (2006) 074507, [arXiv:0601137 [hep-ph]].

[17] J. J. Dudek, R. G. Edwards, *Phys. Rev. D* **79** (2009) 094504, [arXiv:0902.2241 [hep-ph]].

[18] D. Becirevic, F. Sanfilippo, *JHEP 01:028* (2013), [arXiv:1206.1445 [hep-ph]].

[19] E. Follana *et al.*, *Phys. Rev. D* **75** (2007) 054502, [arXiv:0610092 [hep-lat]].

[20] R. Gupta, (1997), [arXiv:9807028 [hep-lat]].

[21] D. Ebert, R. N. Faustov, V. O. Galkin, *Phys. Rev. D* **67** (2003) 014027.

[22] G. Donald *et al.*, *Phys. Rev. D* **86** (2012) 094501, [arXiv:1208.2855 [hep-lat]].

[23] J. J. Dudek, R. G. Edwards, and D. G. Richards, *Phys. Rev. D* **73** (2006) 074507, [arXiv:0601137 [hep-ph]].

[24] C. Davies, C. McNeile, E. Follana, G. Lepage *et al. (HPQCD Collaboration)*, *Phys. Rev. D* **82** (114504 (2010)), [arXiv:1008.4018 [hep-ph]].

[25] A. Vinokurova *et al.*, *Phys. Lett. B* **706** (2011) 139, [arXiv:1105.0978 [hep-ph]].

[26] M. Ablikim *et al.*, *Phys. Lett. B* **108** (2012) 222002, [arXiv:1111.0398 [hep-ph]].

[27] M. Ablikim *et al.*, *Phys. Rev. D* **86** (2012) 092009, [arXiv:1209.4963 [hep-ph]].

[28] C. Semay, B. Silvestre-Brac *et al.*, *Nuclear Physics A* **618** (1997) 455.

[29] L. Cao, Y. C. Yang and H. Chen, *Few Body Syst.* **53** (2012) 327, [arXiv:1206.3008 [hep-ph]].

[30] R. Aaij *et al.,* [LHCb Collaboration], *Eur. Phys. J.* **C75** (2015) 7, [arXiv:1409.3612 [hep-ex]].

[31] T. Barnes, S. Godfrey, *Phys. Rev. D* **69** (2004) 054008.

[32] D. Mohler, S. Prelovsek, R. M. Woloshyn, *Phys. Rev. D* **87** (2013) 034501.

[33] E. J. Eichten, K. Lane, and C. Quigg, *Phys. Rev. D* **73** (2006) 014014.

[34] J. Segovia, D. R. Entem, F. Fernandez, E. Hernandez, *Int. J. Mod. Phys. E* **22** (2013) 1330026, [arXiv:1309.6926 [hep-ph]].

[35] W. J. Deng, L. Y. Xiao, L. C. Gui and X. H. Zhong, *Phys. Rev. D* **95** (2017) 034026, [arXiv:1510.08269 [hep-ph]].

[36] J. Soto, *Eur. Phys. J. A* **31** (2007) 705-710, [arXiv:nucl-th/0611055].

[37] M. Neubert, (2005) 149, [arXiv:0512222 [hep-ph]].

[38] J. Segovia, (2016), [arXiv:1603.08527 [hep-ph]].

[39] W. Caswell and G. Lepage, *Phys. Lett. B* **167** (1986) 437.

[40] N. Brambilla, J. Soto and A. Vairo, *Nucl. Phys. B* **566** (2000) 275.

[41] A. Pineda and J. Segovia, *Phys. Rev. D* **87** (2013) 074024, [arXiv:1302.3528 [hep-ph]].

[42] N. Brambilla, P. Pietrulewicz, A. Vairo, *Phys. Rev. D* **85** (2012) 094005, [arXiv:1203.3020 [hep-ph]].

[43] N. Brambilla, Y. Jia and A. Vairo, *Phys. Rev. D* **73** (2006) 054005, [arXiv:0512369 [hep-ph]].

[44] J. Gaiser *et al.*, *Phys. Rev. D* **34** (1986) 34.

[45] V. V. Anashin *et al.*, *Phys. Lett. B* **738** (2014) 391, [arXiv:1406.7644 [hep-ex]].

[46] V. V. Anashin *et al.*, [arXiv:1012.1694 [hep-ex]].

[47] T. Barnes, S. Godfrey and E. S. Swanson, *Phys. Rev. D* **72** (2005) 054026.

[48] C. Patrignani *et al.*, (Particle Data Group) *Chinese. Phys. C* **40** (2016) 100001.

[49] F. Harris *et al.*, [BESIII Collaboration], (2017), [arXiv:1703.00077 [hep-ex]].

[50] S. B. Ethe *et al.*, *Phys. Rev. D* **70** (2004) 112002.

[51] D. M. Asner *et al.*, *Rev. Lett.* **92** (2004) 142001.

[52] J. Giser (SLAC) *et al.*, *Phys. Rev. D* **34** (1986) 711.

[53] G. Li and Q. Zhao, *Phys. Rev. D* **84** (2011) 074005, [arXiv:1107.2037[hep-ph]].

[54] T. Kawanai and S. Sasaki, *Phys. Rev. D* **92** (2015) 094503, [arXiv:1508.02178 [hep-lat]].

[55] T. Burch, C. DeTar, M. Di Pierro, A. X. El-Khadra, E. D. Freeland, S. Gottlieb, A. S. Kronfeld, L. Levkova, P. B. Mackenzie, and J. N. Simon, *Phys. Rev. D* **81** (2010) 034508, [arXiv:0912.2701 [hep-lat]].

[56] Website: http://www.ihep.ac.cn/english/ihep.htmhttp://www.ihep.ac.cn/english/ihep.htm.

[57] M. Ablikim *et al.*, *Nucl. Instrum. Meth. A* **614** (2010) 310.

[58] D. M. Asner *et al.*, *Int. J. Mod. Phys. A* **24**, S1 (2009), [arXiv:0809.1869 [hep-ex]].

[59] T. Appelquist and H. D. Politzer, *Phys. Rev. Lett.* **34** (1975) 43.

[60] A. De Rujula and S. L. Glashow, *Phys. Rev. Lett.* **34** (1975) 46.

[61] M. E. Franklin *et al.,* [Mark-II Collaboration], *Phys. Rev. Lett.* **51** (1983) 963.

[62] X. H. Mo, C. Z. Yuan and P. Wang, *High Energy Phys. Nucl. Phys.* **31** (2007) 2676.

[63] E. Eichten *et al.*, *Phys. Rev. Lett.* **34** (1975) 369.

[64] E. Eichten *et al.*, *Phys. Rev. D* **21** (1980) 203.

[65] C. Amsler *et al.*, (Particle Data Group), *Jour. Phys. G* **37** (2008) 075021.

[66] M. Ablikim *et al.*, [BES Collaboration], *Phys. Rev. D* **76** (2007) 74.

[67] M. Ablikim *et al.*, [BES Collaboration], *Phys. Lett. B* **659** (2008) 74.

[68] D. Besson *et al.*, [CLEO Collaboration], *Phys. Rev. Lett.* **96** (2006) 092002.

[69] M. Ablikim *et al.*, [BES Collaboration], *Phys. Rev. Lett.* **101** (2008) 102004.

[70] M. Ablikim *et al.*, [BES Collaboration], *Phys. Lett.* **688** (2008) 253.

[71] J. Z. Bai *et al.*, [BES Collaboration], *Hep & Np.* **28(4)** (2004) 325.

[72] M. Ablikim *et al.*, [BES Collaboration], *Phys. Lett. B* **605** (2005) 63.

[73] K. Nakamura *et al.*, (Particle Data Group), *Phys. Lett. B* **667** (2010) 1.

[74] R. M. Baltrusaitis *et al.*, [Mark-III Collaboration], *J. Phys. G* **37** (2010) 075021.

[75] K. Nakamura *et al.*, (Particle Data Group), *Rev. D* **33** (1986) 629.

[76] J. Z. Bai *et al.*, [BES Collaboration], *Phys. Lett. B* **555** (2003) 174.

[77] D. M. Asner *et al.*, [CLEO Collaboration], *Phys. Rev. Lett.* **555** (2003) 174.

[78] J. Z. Bai *et al.*, [BES Collaboration], *Phys. Lett. B* **92** (2004) 142001.

[79] A. Vinokurova *et al.*, [Belle Collaboration], *Phys. Lett. B* **8706** (2011) 139.

[80] R. E. Mitchell *et al.*, [CLEO Collaboration], *Phys. Rev. Lett.* **102** (2009) 011801.

[81] D. Bernstein *et al.*, *Nucl. Instr. and Meth in Phys. Research A* **226** (1984) 301.

[82] M. Ablikim *et al.*, [BESIII Collaboration], *Phys.Rev. D* **92** (2015) 071101.

[83] M. Ablikim *et al.*, [BESIII Collaboration], *Nucl. Instrum. Methods Phys. Res., Sec. A.* **614** (2010) 345.

[84] M. Ablikim *et al.*, [BESIII Collaboration], *Chinese. Phys. C* **37** (2013) 123001.

[85] M. Ablikim *et al.*, [BESIII Collaboration], *Phys. Rev. D* **83** (2011) 112005.

[86] M. Ablikim *et al.*, [BESIII Collaboration], *Chinese. Phys. C* **39** (2015) 093001.

[87] J. Z. Bai *et al.*, *Phys. Rev. D* **53** (1996) 20.

[88] Y. Tsai *et al.*, *Phys. Rev. D* **4** (1971) 2821.

[89] W. J. Marciano and A.Sirlin, *Phys. Rev. Lett.* **61** (1988) 1815.

[90] M. N. Achasov *et al.*, [BESIII Collaboration], *Phys. Rev. D* **90** (2014) 012001.

[91] Atsushi Hosako, Takayuki Myo, Kanabu Nawa *et al.*, *Osaka university* (2009).

[92] J. Z. Bai *et al.*, [BESIII Collaboration], *Phys. Rev. Lett.* **84** (2000) 594.

[93] M. A. *et al.*, *Chinese Phys. C* **34** (2010) 421.

[94] J. Z. Bai, Y. Ban, J. G. Bian, X. Cai, J. F. Chang, H. F. Chen, H. S. Chen, J. Chen, J. Chen, J. C. Chen, *et al.*, [BESIII Collaboration], *Phys. Rev. Lett.* **91** (2003) 022001.

[95] B. Aubert, R. Barate, M. Bona, D. Boutigny, F. Couderc, Y. Karyotakis, J. P. Lees, V. Poireau, V. Tisserand, A. Zghiche *et al.*, *Phys. Rev. D* **74** (2006) 051101.

[96] M. Ablikim *et al.*, [BESIII Collaboration], *Nucl. Instrum. Meth. A* **614** (2010) 345, [arXiv:0911.4960 [physics.ins-det]].

[97] M. Ablikim *et al.*, [BESIII Collaboration], *Nucl. Instrum. Meth. A* **614** (2010) 345.

[98] H. Bethe and J. Ashkin *et al.*, [BESIII Collaboration], *Exp. Nucl. Phys. E. Segre, J. Wiley.* (eds) 253 (1953).

[99] N. Berger *et al.*, [BESIII Collaboration], *Chinese. Phys. C* **34** (2010) 1779.

[100] O. Bondarenko, Ph.D. thesis, Rijksuniversiteit Groningen; *Isospin-Suppressed Charmonium Transitions below the Open-Charm Threshold.* (2014).

[101] W. Li *et al.*, *Proc. Int. Conf. Comput. High Energy and Nucl. Phys* (eds) 225 (2006).

[102] C. Arnault, *Comput. Phys. Commun.* **140** (2001) 1.

[103] G. Cowan, *Statistical data analysis, Oxford Univ. Press Inc., New York,* (1998).

[104] R. Ping, *Chinese. Phys. C.* **32** (2008) 599.

[105] A. Ryd *et al.*, http://robbep.home.cern.ch/robbep/EvtGen/GuideEvtGen.pdf.

[106] R. Barlow, (2009), [arXiv:0406120 [hep-ex]].

[107] http://www.cern.ch/gdml.

[108] W. Li *et al.*, *The offline software for the BESIII experiment, Proceedings of CHEP,* (http://indico.cern.ch/event/048/session/3/20060214, 2006).

Phys. Rev. Lett. **34** (1975) 43-45.

[109] E. Richter-Was, *Phys. Lett. B* **303** (1993) 163.

[110] T. Bayes, Phil. Trans., *Roy. Soc.* **53** (1763) 370 .

[111] H. Jeffreys, *Theory of probability, 3rd edition, Clarendon, Oxford* (1961).

[112] H. Jaynes, *IEEE Trans. on System Sci. and Cyber. SSC.* **4** (1968) 227.

[113] R.-G. Ping *et al.*, [BESIII Collaboration], *Chinese. Phys. C* **32** (2008) 599.

[114] S. Chakravarty, S. M. Kim and P. Ko, *Phys. Rev. D* **50** (1994) 389.

[115] P. Avery, *Applied Fitting Theory I: General Least Squares Theory* **CBX** 91.

[116] M. Ablikim *et al.*, [BESIII Collaboration], *Chinese. Phys. C* **37** (2013).

[117] http://home.web.cern.ch.

[118] S. Jadach, B. F. L. Ward and Z. Was, *Comp. Phys. Commun.* **130** (2000) 260.

[119] T. Sjöstrand, S. Mrenna, and P. Skands, *Comp. Phys. Commun.* **178** (2008) 852.

[120] N. Berger, *et al.*, [BESIII Collaboration], *Chinese Physics C* **34** (2010) 1779, [arXiv:1011.2825].

[121] M. Ablikim, *et al.*, [BESIII Collaboration], *Phys. Rev. D* **87** (2013), [arXiv:1208.4805].

[122] M. Xu *et al.*, *Chinese Physics C* **33** (2009) 428.

[123] F. Liu, K. Zhu, Y. Chen, J. X. Zuo,, *talk at DQ/Validation Meeting* (2010).

[124] M. Ablikim, *et al.*, [BESIII Collaboration], *Phys. Rev. D* **81** (2010) 052005.

[125] D. J. Lange, *Nucl. Instrum. Meth. A* **462** (2001) 152.

[126] R. G. Ping *et al.*, *HEPNP* **32** (2008) 599.

[127] H. Miao, *Journal of physics: Conference Series* **293** (2011) 012025.

[128] M. He *et al.*, *Chinese Physics C (HEP and NP)* **32(04)** (2008) 269.

[129] J. M. Bian *et al.*, *Chinese Physics C (HEP and NP)* **34(01)** (2010) 7277.

[130] B. B. Brabson *et al.*, *Nucl. Instr. Meth A* **332** (1993) 419.

[131] M. He (BESIII Collaboration), *Journ. of Phys: Conference Series* **293** (2011) 012025.

[132] D. Wang *et al.*, *Nuclear Electronics and Detection Technology* **27** (2007) 658.

[133] M. E. Rose, *Elementary Theory of Angular Momentum* (1957).

[134] M. Ablikim *et al.*, *Nucl. Instr. Meth A* **614** (2010) 345.

[135] M. Ablikim *et al.*, *Phys. Rev. D* **88** (2013) 112001.

[136] M. Ambrogiani *et al.*, *Phys. Lett. B* **566** (2003) 45.

[137] W. Erni *et al.*, *Physics Performance Report for PANDA*, [arXiv:0903.3905].